Application of Deep Learning for High-Resolution Flood Mapping in Urban Watersheds

Cesar Ambrogi Ferreira do Lago
Prof. Dr. Eduardo Mario Mendiondo

EESC · USP

UNIVERSIDADE DE SÃO PAULO

ESCOLA DE ENGENHARIA DE SÃO CARLOS

Cesar Ambrogi Ferreira do Lago

Application of Deep Learning for High-Resolution Flood Mapping in Urban Watersheds

São Carlos

2023

Cesar Ambrogi Ferreira do Lago

Application of Deep Learning for High-Resolution Flood Mapping in Urban Watersheds

Tese apresentada à Escola de Engenharia de São Carlos da Universidade de São Paulo, para obtenção do título de Mestre/Doutor em Ciências - Programa de Pós-Graduação em Engenharia Hidráulica e Saneamento.

Advisor: Prof. Dr Eduardo Mario Mendiondo

CORRECTED VERSION

São Carlos

2023

AUTORIZO A REPRODUÇÃO TOTAL OU PARCIAL DESTE TRABALHO, POR QUALQUER MEIO CONVENCIONAL OU ELETRÔNICO, PARA FINS DE ESTUDO E PESQUISA, DESDE QUE CITADA A FONTE.

Ficha catalográfica elaborada pela Biblioteca Prof. Dr. Sérgio Rodrigues Fontes da EESC/USP com os dados inseridos pelo(a) autor(a).

Eduardo Graziosi Silva - CRB - 8/8907

FOLHA DE JULGAMENTO

Candidato: Bacharel **CESAR AMBROGI FERREIRA DO LAGO**.

Título da tese: "Aplicação de Aprendizado Profundo para Mapeamento de Inundações em Alta Resolução em Bacias Urbanas".

Data da defesa: 13/09/2023.

Comissão Julgadora	Resultado
Prof. Dr. Eduardo Mario Mendiondo (Orientador) (Escola de Engenharia de São Carlos/EESC-USP)	**Aprovado**
Prof. Dr. Daniel Gustavo Allasia Piccilli (Universidade Federal de Santa Maria/UFSM)	**Aprovado**
Prof. Dr. Eduardo Sávio Passos Rodrigues Martins (Universidade Federal do Ceará/UFC)	**Aprovado**
Prof. Dr. José Goes Vasconcelos Neto (Auburn University)	**Aprovado**
Prof. Dr. Celso Augusto Guimarães Santos (Universidade Federal da Paraíba/UFPB)	**Aprovado**

Coordenador do Programa de Pós-Graduação em Engenharia Hidráulica e Saneamento:
Prof. Assoc. **Juliano Jose Corbi**

Presidente da Comissão de Pós-Graduação:
Prof. Titular **Carlos De Marqui Junior**

Este trabalho é dedicado aos meus avós

ACKNOWLEDGEMENTS

Meus agradecimentos se estendem a Adenauer e Neuza, meus pais, Conrado e Sheila, meus irmãos, e Mariana, minha namorada, que me apoiaram durante esta caminhada. Finalmente, minha gratidão aos meus amigos da USP e UTSA.

"Water is the Driving Force of All Nature."
Leonardo da Vinci

ABSTRACT

do Lago, C., A., F., **Application of Deep Learning for High-Resolution Flood Mapping in Urban Watersheds**. 2023. 118p. Thesis (Doctor) - Escola de Engenharia de São Carlos, Universidade de São Paulo, São Carlos, 2023.

Flood events significantly threaten urban environments, causing substantial economic damage and loss of life. Accurate prediction and mapping of these events are crucial for effective mitigation strategies. However, current hydrodynamic models used for flood prediction are expensive to build and often impractical for real-time applications or simulations on large domains due to long computational times. This dissertation explores the utility of Deep Learning (DL) models as a viable alternative for flood prediction and floodplain mapping, addressing the evident gap in current flood modeling practices. The research implements a three-fold methodology across three chapters, focusing on developing and applying ANNs for flood prediction. Chapters 1 and 2 use a conditional generative adversarial network developed for rapid pluvial flood predictions (cGAN-Flood). Chapter 1 demonstrates a novel DL application – improving flood mapping resolution from existing coarse hydrodynamic models using cGAN-Flood. Chapter 2 assesses the performance of cGAN-Flood, in distinct topological settings, specifically catchments in Sao Paulo, compared to its original training in San Antonio, Texas. Lastly, Chapter 3 outlines the creation of a novel model that predicts pluvial flood maps using ANN, requiring only Digital Elevation Models (DEM) and inflow inputs. General results across the chapters show the promising efficacy of ANNs and DL models in flood prediction and floodplain mapping. ANNs demonstrated the ability to emulate hydrodynamic models with high precision, while cGAN-Flood's application showed satisfactory predictive capabilities even in geographically distinct and topologically different regions. The newly proposed model in Chapter 3 compared favorably against FEMA floodplain maps, despite the simplicity of its training data. In conclusion, the research demonstrates that DL models, with further enhancements and training, can transform floodplain mapping and prediction, supporting faster simulations and extending applicability to different locations without retraining. This research underscores the potential of these models in bridging the gaps in current flood modeling practices, which is particularly significant for real-time flood prediction and the development of mitigation strategies, especially in developing regions where resources may be scarce or in larger domains.

Keywords: Deep learning, rapid flood models, artificial neural networks, rain-on-grid, high-resolution flood mapping.

RESUMO

do Lago, C., A., F., **Aplicação de Aprendizado Profundo para Mapeamento de Inundações em Alta Resolução em Bacias Urbanas**. 2023. 118p. Tese (Doutorado) - Escola de Engenharia de São Carlos, Universidade de São Paulo, São Carlos, 2023.

Eventos de inundação ameaçam ambientes urbanos, causando danos econômicos e perda de vidas. A previsão e o mapeamento desses eventos são cruciais para uma mitigação eficaz. No entanto, os atuais modelos hidrodinâmicos usados para a previsão de inundações são caros e muitas vezes impraticáveis para previsão em tempo real ou simulações em grande áreas pelos longos tempos de simulação. Esta tese explora modelos de Deep Learning (DL) como uma alternativa viável para a previsão de inundações e o mapeamento de planícies de inundação, abordando a lacuna nas práticas atuais de modelagem de inundações. A pesquisa foi dividida em três capítulos, focando no desenvolvimento e aplicação de Redes Neurais Artificiais (ANNs) para a previsão de inundações. Os capítulos 1 e 2 usam uma rede adversarial generativa condicional desenvolvida para previsões rápidas de inundações pluviais (cGAN-Flood). O Capítulo 1 demonstra uma nova aplicação de DL - aprimorar a resolução do mapeamento de inundações a partir de modelos hidrodinâmicos existentes usando cGAN-Flood. O Capítulo 2 avalia o desempenho do cGAN-Flood em ambientes topológicos distintos, especificamente bacias hidrográficas em São Paulo, comparado ao seu treinamento original em San Antonio, Texas. Por fim, o Capítulo 3 descreve a criação de um novo modelo que prevê mapas de inundações fluviais usando ANN, requerendo apenas Modelos Digitais de Elevação (DEM) e hidrogramas. Os resultados mostrados nos capítulos mostram uma eficácia promissora das ANNs na previsão de inundações e no mapeamento de de inundação. As ANNs demonstraram a capacidade de emular modelos hidrodinâmicos com alta precisão. Enquanto a aplicação do cGAN-Flood mostrou uma performance satisfatórias, mesmo em regiões geograficamente distintas e topologicamente diferentes, o novo modelo proposto no Capítulo 3 se comparou favoravelmente aos mapas de planícies de inundação da FEMA, apesar da simplicidade de seus dados de treinamento. Em conclusão, a pesquisa demonstra que os modelos DL, com mais desenvolvimento e treinamento, têm o potencial para aprimorar previsão de planícies de inundação, devido a simulações mais rápidas e estendendo a aplicabilidade a diferentes localizações sem re-treinamento. Esta pesquisa destaca o potencial desses modelos em preencher as lacunas nas práticas atuais de modelagem de inundações, o que é particularmente significativo para a previsão de inundações em tempo real e o desenvolvimento de estratégias de mitigação, especialmente em regiões em desenvolvimento, onde os recursos podem ser escassos, ou em maior escala.

Palavras-chave: Aprendizado profundo, modelos de inundações rápidos, chuva no grid, redes neurais artificiais, Mapeamento de inundações de alta resolução.

LIST OF FIGURES

LIST OF TABLES

LIST OF ABBREVIATIONS AND ACRONYMS

1D	One Dimensional
2D	Two Dimensional
ANN	Artificial Neural Networks
CA	Cellular Automata
CA2D	Cellular Automata 2D
CA-ffé	Cellular Automata Fast Flood Evaluation
CMIP	Coupled Model Intercomparison Project
cGAN	Conditional Generative Adversarial Network
CN	Curve Number
CNN	Convolutional Neural Networks
CSI	Critical Success Index
DEM	Digital Elevation Model
DL	Deep Learning
FAR	False Alarm Rate
FEMA	Federal Emergency Management Agency
GAN	Generative Adversarial Network
GCM	General Climate Model
HAND	Height Above Nearest Drainage
HEC	Hydrologic Engineering Center
HR	Hit Rate
HMS	Hydrologic Modeling System
IDF	Intensity-Duration-Frequency
MAE	Mean Absolute Error
MLP	Multi-Layer Perceptrons

Nadam	Nesterov Accelerated Adaptive Moment Estimation
NSE	Nash-Sutcliff Efficiency
RAS	River Analysis System
ReLU	Rectified Linear Unit
RCM	Regional Climate Model
RCP	Representative Concentration Pathways
RFM	Rapid Flood Modeling
RFSM	Rapid Flood Spreading Models
RMSE	Root-Mean-Square Error
RNN	Recurrent Neural Networks
SCS	Soil Conservation Service
SARA	San Antonio River Authority
tanh	Hyperbolic Tangent
UPSA	Upper San Antonio Watershed
WCA2D	Weighted Cellular Automata 2D
WSE	Water Surface Elevation

CONTENTS

1 INTRODUCTION

Frequency flood maps with depths based on the recurrence interval for design of a particular storm are used for flood assessment. Depending on its depth and extent, the floodplain produces different levels of damage magnitudes. The two categories of damages—tangible and non-tangible—can be used to quantify them. According to (VELDHUIS, 2011), a tangible accounts for losses to infrastructure, goods, and buildings that may be valued financially based on the depth, length, and area impacted by a flood (THIEKEN *et al.*, 2005). Calculating the risk of flooding in a specific area may then be done using the quantifiable damage and the likelihood of occurrence (VELDHUIS, 2011). This practice is frequently employed since it is analogous to safeguarding management and infrastructure plan investments. Intangible losses, however, are indirect and more difficult to quantify. These harms include economic and supply disruption, mass evacuation, and psychological stress among the local people (VELDHUIS, 2011). Furthermore, floods can also harm public health by dispersing disease (LIU *et al.*, 2018; WIJERATHNE; SENEVIRATHNA, 2018).

Different studies in many countries (AICH *et al.*, 2016; CLAVET-GAUMONT *et al.*, 2017; GAO *et al.*, 2020; SHRESTHA; LOHPAISANKRIT, 2017; YIN *et al.*, 2016; LAGO *et al.*, 2021a) provide additional evidence that climate change can increase rainfall frequency and severity, which would subsequently increase the frequency of flood events. The premise of climatic stationarity is, therefore, invalid as climate projections suggest, and flood control practices should be planned and constructed to create robust flood control systems that can function as intended under various scenarios. However, forecasting future flood conditions is difficult given the wide range of potential greenhouse gas emission scenarios and potential climate trajectories. Therefore, the uncertainties of the projections make the development of mitigating strategies more difficult due to the numerous potential outcomes (WANG *et al.*, 2018).

Flood control management is planned and designed with the use of computational models. Flood models are utilized to test how particular flood management practices or modified system elements would perform in order to reduce the effects of flooding. Today, two-dimensional (2D) hydrodynamic models have become popular due to the advance in computational efficiency, such as HEC-RAS 2D (BRUNNER, 2016) and Tuflow (WBM, 2008). However, these models require detailed data inputs and are computationally expensive (AFSHARI *et al.*, 2018). This disadvantage hampers its application in high-resolution large-scale watersheds (hundreds of square kilometers) modeling, where detailed hydrodynamic models would required long simulation times.

The low-complexity flood inundation models or rapid flood models are an alternative

to costly hydrodynamic simulation models (RFM). To shorten simulation times, these models, use simplified hydraulic ideas rather than solving difficult physical equations (JAMALI *et al.*, 2018). However, RFM's simplifications of use can limit the accuracy of how they anticipate floods. Using artificial neural network models (ANN) allows for the computationally efficient learning of complex rules. Compared to hydrodynamic models, recent research has effectively used ANN to predict flood maps, damages, and susceptibility with satisfactory performance and faster simulations. Consequently, this data-driven technique can be used to support rapid flood predictions. In 2021, NEARING *et al.* suggests that the artificial intelligence combined with physically-based models will likely be the future of hydrological predictions. Likewise, the future of flood modeling can also greatly benefit from using data-driven methodologies.

1.1   Climate change

Scientists utilize climate models to comprehend historical and present climate change and trends. The statistics of atmospheric conditions are predicted by general climate models (GCMs) using the gas law (ARNBJERG-NIELSEN *et al.*, 2013). Future climate scenarios are predicted using Representative Concentration Pathways (RCP) to reflect greenhouse gas emission scenarios, with incoming radiation being utilized as a boundary condition (MOSS *et al.*, 2010). GCMs typically have a coarse resolution and mimic the entire planet's climate, which prohibits accurately portraying regional climate characteristics (DIBABA; MIEGEL; DEMISSIE, 2019). Dynamic or statistical downscaling techniques are used to improve spatial resolution and capture regional climate subtleties. The dynamic downscalling approach uses Regional Climate Models (RCM) powered by the GCM or reanalysis data. In contrast, the second uses statistical analysis of local region to make climate predictions based on results at a larger scale (TANG *et al.*, 2016). Biases introduced by dynamic downscaling may need to be fixed (CHEN *et al.*, 2013). GCM and RCM rainfall extremes can be accessed and biased corrected using statistical techniques (ARNBJERG-NIELSEN *et al.*, 2013). Predictions of precipitation made using GCM and downscaled models frequently have considerable uncertainty, particularly for the high rainfall events employed in floodplain research. Furthermore, precipitation outputs from climate models usually have a coarse time resolution, larger than 3 hours (SIM *et al.*, 2018), which may be not suitable for micro-drainage studies (BERNE *et al.*, 2004; LAGO *et al.*, 2023). Therefore, improving temporal resolution often make use of synthetic hyetographs (LAGO, 2022), which adds extra uncertainties to projections.

The numerous uncertainties in future climate predictions significantly increase the complexity of water management plans to reduce the effects of climate change (LAWRENCE *et al.*, 2013; SHEN *et al.*, 2018).In 2013, SILLMANN *et al.* compared Phase 5's Coupled Model Intercomparison Project's GCMs' performance (CMIP5). The study used 27 indices

for temperature, precipitation, droughts, and other factors to assess the models. Fig 1 outlines their findings for six indices that have the potential to significantly affect how accurately future flood occurrences can be predicted: (1) The highest amount of precipitation in a single day, (2) the highest amount of precipitation in five consecutive days, (3) the 95th and 99th percentiles of the heaviest rainfall events, (4) the number of days with rainfall above 10mm, and (5) the maximum amount of precipitation in 20mm.
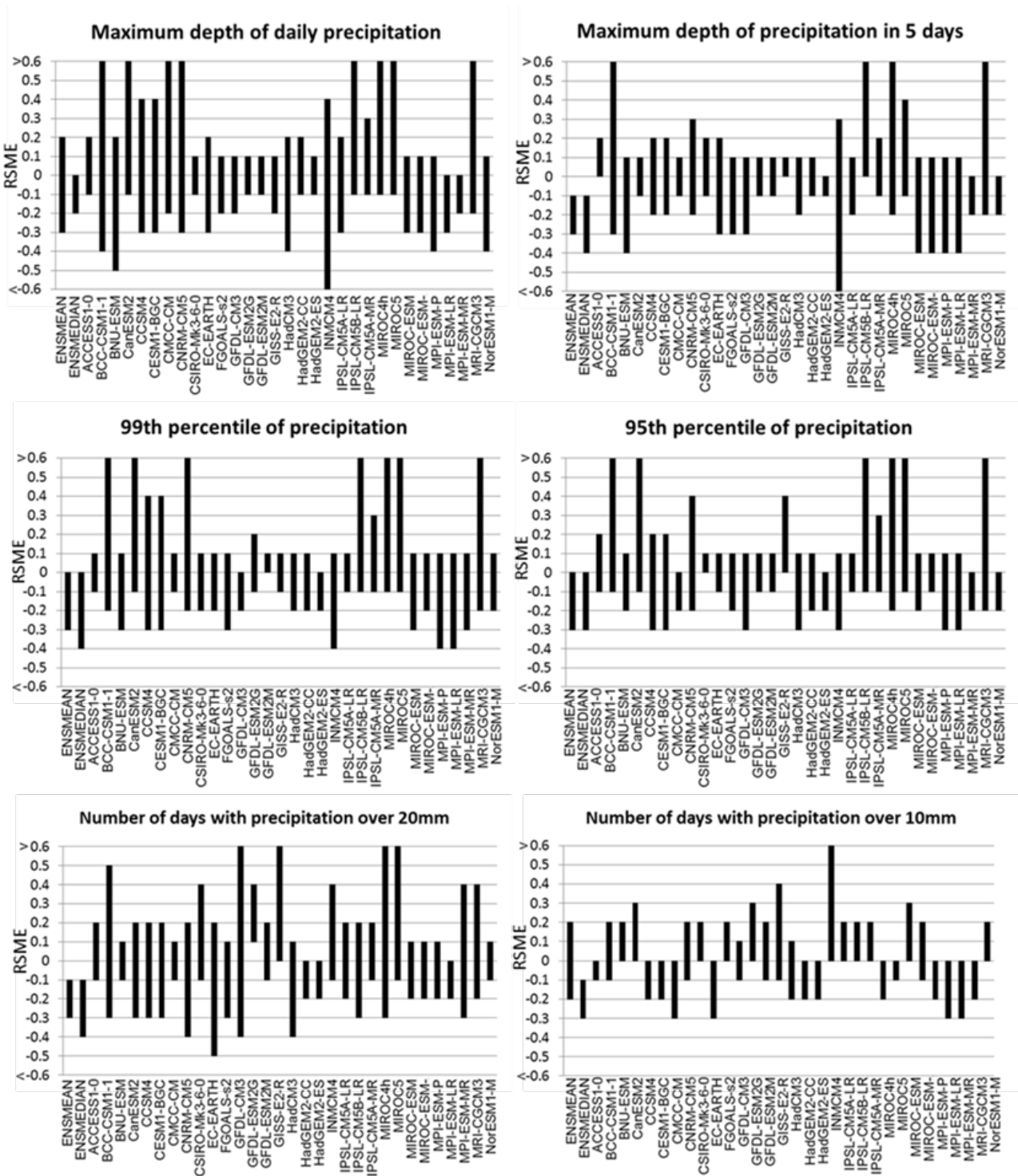
Figure 1 – Review uncertainties of climate change projections. Adapted from (SILLMANN *et al.*, 2013)

As can be observed, there are significant differences in uncertainties between the climate models (Fig 1), which directly impact the identification of design events estimated from intensity-duration frequency IDF. In 2015, CHANDRA; SAHA; MUJUMDAR employed a Bayesian technique with 26 General Climate Models (GCM) in CMPI5 and

discovered that IDF parameter uncertainties are more significant than GCM parameter uncertainties. In 2018, KUNDZEWICZ *et al.* highlighted many sorts of climate change and water resource uncertainties as well as potential solutions. Two strategies can be used to deal with uncertainties that cannot be reduced. Precaution is the first approach, considering the worst-case scenario for the mitigation preparations. The second method uses a multi-model probabilistic approach, which could result in different results. In a further study, (DEGAETANO; CASTELLANO, 2017) generated projected IDF for New York State using a mix of 50 GCM and RCM. They discovered that the median increase in rainfall intensity for the RCP 8.5 scenario is to increase by 20 to 30%. In southern Ontario, under RCP 8.5, there is likely to be a significant increase in the 10-year storm (GANGULI; COULIBALY, 2017). In 2016, AGILAN; UMAMAHESH used 24 GCM and discovered that the frequency of intense rainfalls is declining in India's central-south region. According to (KUNDZEWICZ *et al.*, 2018), handling climate change uncertainties should be done with precaution or by employing a probabilistic multi-model approach. The precaution strategy evaluates the worst-case outcome and is often used for critical infrastructures, such as dams, which in case of failure, can cause unprecedented damages. The second includes numerous solutions based on multiple global models' output, so decision-makers understand all possible climate outcomes to elaborate mitigation strategies.

Multi-probabilistic analysis has been used to understand potential climate change impacts on precipitation volumes, flood events, and runoff quality. For example, (WASKO; SHARMA, 2017) suggested a new methodology with variables to link the sensitivity of rainfall to temperatures of historical series to mimic continuous rainfall. In Australia, this method was used to simulate rainfall volumes changes in predicted by different warmer scenarios. Their investigation showed a correlation between increased temperature and increased rainfall extremes. JATO-ESPINO *et al.* (2019) used an optimization tool to modify the model parameters to predict future runoff flows brought on by extreme rainfall accurately. This method was deployed in Finland to provide more reliable analysis of the effects of climate change on flooding,. According to their findings, the risk of flooding might increase by up to five times due to climate change. WANG *et al.*, in 2020, selected 18 future climate projections to examine the effects of land use and climate change on severe occurrences in China. The authors employed three GCMs and three RCMs to scale them down for two future periods. According to their findings, climate change will result in a rise in the extreme precipitation indices, such as the maximum daily and five consecutive days of precipitation. More than 50% of the overall increase in floods may be attributable to climate change alone.

The most significant disadvantage of the multi-probabilistic evaluation of climate change is the requirement for several simulation runs of different possible scenarios. In the case of flood studies, in particular, the hydrodynamic models can often be complex and expensive to build. In addition, the generation of detailed flood maps may require long

simulation runs due to complex physical equations used in hydrodynamic models. These disadvantages can make multi-probabilistic analysis harder and hamper the evaluation of large-scale domains.

1.2 Flood Modeling Methods

This section review two types of flood modeling approaches. The first are the hydrodynamic models, which uses the laws of physics for simulating floods. RFM uses simplified rules, instead of complex hydrodynamic equations, to reduce simulation time and generate faster results. This approach can be an alternative to the complex traditional hydrodynamic models.

1.2.1 Hydrodynamic Models

Hydrodynamic models are the most popular tools used for flood predictions. These models apply on the laws of physics to simulate mainly flood depths and water velocities. The most widely used hydrodynamic models today are the one and two dimensional models (1D and 2D).

Models based on one dimension (1D) portray fluid movement within river channels by using conservation of mass and momentum principles (1D Saint-Venant equations) between various cross-sections. These models enable the estimation of water flow and level at each individual cross-section for every time increment (BRUNNER, 2016). Despite their computational efficiency, 1D models have limitations in simulating floods laterally (TENG *et al.*, 2017). Furthermore, their inability to provide topographical information between cross-sections may result in less accurate predictions for floodplain extents. For instance, blocked obstacles between cross-sections that prevent flows cannot be captured. Therefore, portions of cross-sections that do not effectively contribute to the flow, known as ineffective flow areas, must be manually inserted in the models, increasing the labor efforts. In addition, ineffective flow areas can be a significant source of instability issues when misplaced. 1D flood modeling can be recommended for (USACE, 2023):

- Rivers and floodplains where the dominant flow direction aligns with the river flow.

- River systems with numerous hydraulic structures, such as bridges, culverts, weirs, dams, and pump stations, as 1D models currently have a more comprehensive set of hydraulic structure modules.

- Large river systems requiring long time period forecasts.

- Areas where the available data does not support the use of a 2D model due to poor terrain accuracy.

Two-dimensional (2D) hydrological models, essentially a reduced form of the three-dimensional (3D) Navier-Stokes equations for fluid dynamics, conduct flood computations within a 2D space. These models work under the presumption that the water depth is significantly shallow when compared to the 2D domain (DHI, 2011; BRUNNER, 2016). Horizontal velocities and water levels over time are often determined using shallow water equations of mass and momentum conservation (BRUNNER, 2016; TENG *et al.*, 2017). Due to developments in computation, 2D modeling is becoming more effective and is advised for studies of floodplains (COUNCIL, 2009). When compared to 1D flood modeling, 2D models can predict velocity in better resolution, are more reliable in low-relief areas (MORSY *et al.*, 2018). These advantages are relevant to replicating flooded roadways, whose characteristics are captured due to interpolation between cross-sections in a 1D model. However, 2D models require high-resolution elevation data to make reliable predictions. For example, (FEMA, 2018) suggests a 3m resolution of the 2D domains for studies of floodplains. But such models' high computational costs limit their capacity to be used in large-scale areas (TENG *et al.*, 2017), which is often performed with larger cell size, which requires extra effort in building the model (e.g. a careful placement of breaklines to better represent the terrain and important features with the mesh). The following scenarios can be better modeled with 2D models (USACE, 2023):

- Leveed systems prone to overtopping or breaching, causing water to flow in various directions.

- Bays and estuaries with fluctuating tidal currents and river flows.

- Locations where the water flow path isn't entirely clear.

- Highly braided streams and alluvial fans.

- Regions with abrupt bends that might experience significant super-elevation during an event.

- Wide, flat floodplains with multiple flow paths.

- Applications requiring detailed velocity calculations, such as around bridge piers or abutments.

The coupling of 1D and 2D domains is also an effective method, particularly in situations where the water system's complexity necessitates a comprehensive representation of flow. This could include regions with intricate hydraulic structures, rivers with extensive floodplains, urban settings, and watersheds where river and surface flows coexist. The primary benefits of both approaches can be merged to provide a more trustworthy depiction of the area under study. For instance, a 1D model could be designed for the main river,

incorporating all hydraulic structures, and connected to a 2D domain through overbanks. In this scenario, the river overflow is transferred to the 2D domain to provide a more accurate portrayal of flow dynamics in detailed terrain. However, it's important to note that the interaction between 1D and 2D domains can lead to instability if not appropriately modeled (BETSHOLTZ; NORDLÖF, 2017).

1.2.2 Rapid Flood Models

In order to shorten simulation time, RFM use simplified hydraulic rules rather than solving complex physical equations (TENG *et al.*, 2017). The HAND (Height Above Nearest Drainage) (NOBRE *et al.*, 2011a), for instance, is an example of a rapid flood modeling approach for 1D modeling. The HAND metric provides a measure of elevation above the nearest drainage (typically a river, stream, or other watercourse) for any given location in a landscape. For each cell in the DEM, the vertical difference between its elevation and the elevation of the nearest cell in the stream network is calculated. This results in a HAND raster, where each cell's value indicates its height above the nearest drainage. It offers insights into various landscape characteristics, such as potential wetness, flood susceptibility, and even habitats for different species.

Cellular automata (WOLFRAM, 1984), is another common approach for RFM (JAMALI *et al.*, 2019; GUIDOLIN *et al.*, 2016; GHIMIRE *et al.*, 2013; JR *et al.*, 2023). Flooding from one grid spreads according to a set of principles that depend on the neighboring cells' properties and the grid's prior state. Examples of the application of cellular automata used for flood simulations include the Cellular Automata for 2D Modeling (CA2D) (GHIMIRE *et al.*, 2013) and Weighted Cellular Automata 2D (GUIDOLIN *et al.*, 2016). These investigations make use of Manning's equation to perform the overflow distribution. The first sort the neighboring cells based on the elevation of the water's surface, while the second inserts weights into neighboring cells following their inflow potential. The Cellular Automata Fast Flood Evaluation (CA-ffé), a less complex cellular automata model that does not provide a temporal evolution of flooding, was created by (JAMALI *et al.*, 2018) (2018). Criteria for the distribution of flood volume include rules such as flow when central cells have an elevation height and lower than at least one neighboring cell; spreading when the main cells and neighboring cells have the same elevations and; ponding when the elevation of the central cells is lower than all neighbors. A power-type equation inspired by hydrological rating curves is used to distribute flood volume to cells downstream. Rapid Flood Spreading Models (RFSM) (GOULDBY *et al.*, 2008) were evaluated and adjusted by (BERNINI; FRANCHINI, 2013). This model is based on accumulation zones with simplified exchange qualities between them, where excess flood volume accumulates instantly. The authors also suggested changes, such as gradually applying the weir equation between accumulation zones and filling the areas.

A review of the literature on five RFM models shows that the gains of computational time are several orders of magnitude while losing relatively small performance. Fig 2 shows an analysis performed comparing flood maps of five RFMs and corresponding 2D hydrodynamic models in different catchments worldwide. The CA2D was compared with Urban Inundation Model (CHEN *et al.*, 2013), WCA2D with InfoWorks (INNOVYZE, 2012), the performance of CA-ffé was tested with HEC-RAS (BRUNNER, 2016), and TUFLOW, RUFIDAM, on the other hand, was evaluated against MIKE FLOOD (DHI, 2011), and RFSM with FLO-2D. Fig 2a shows the Root Mean Square Error (RMSE) for all the domain cells versus how many times faster RFMs are compared to 2D hydrodynamic models. The results indicate that most model simulations are 100 times faster while maintaining an RMSE lower than 0.15 meters. In addition, the chart shows that RFSM and CA-feé outperform other models in speed. The computational time in Fig 2b was computed by dividing the total run time by the number of cells and the duration of the simulation to eliminate the effect of the size of the spatial domain and the cell size. It can be observed that the computational effort is greatly reduced by some orders of magnitude when compared to hydrodynamic models. The results indicate that some models present a clear linear relationship between the cell size and the computational time (e.g. WCA2D), while other models are less sensitive to the resolution of the spatial domain (e.g. RUFIDAN). RSME also seems independent of the watershed size (Fig 2c) and cell resolution (Fig 2d). These analyses show that RFM can significantly reduce computational time and produce reliable results.
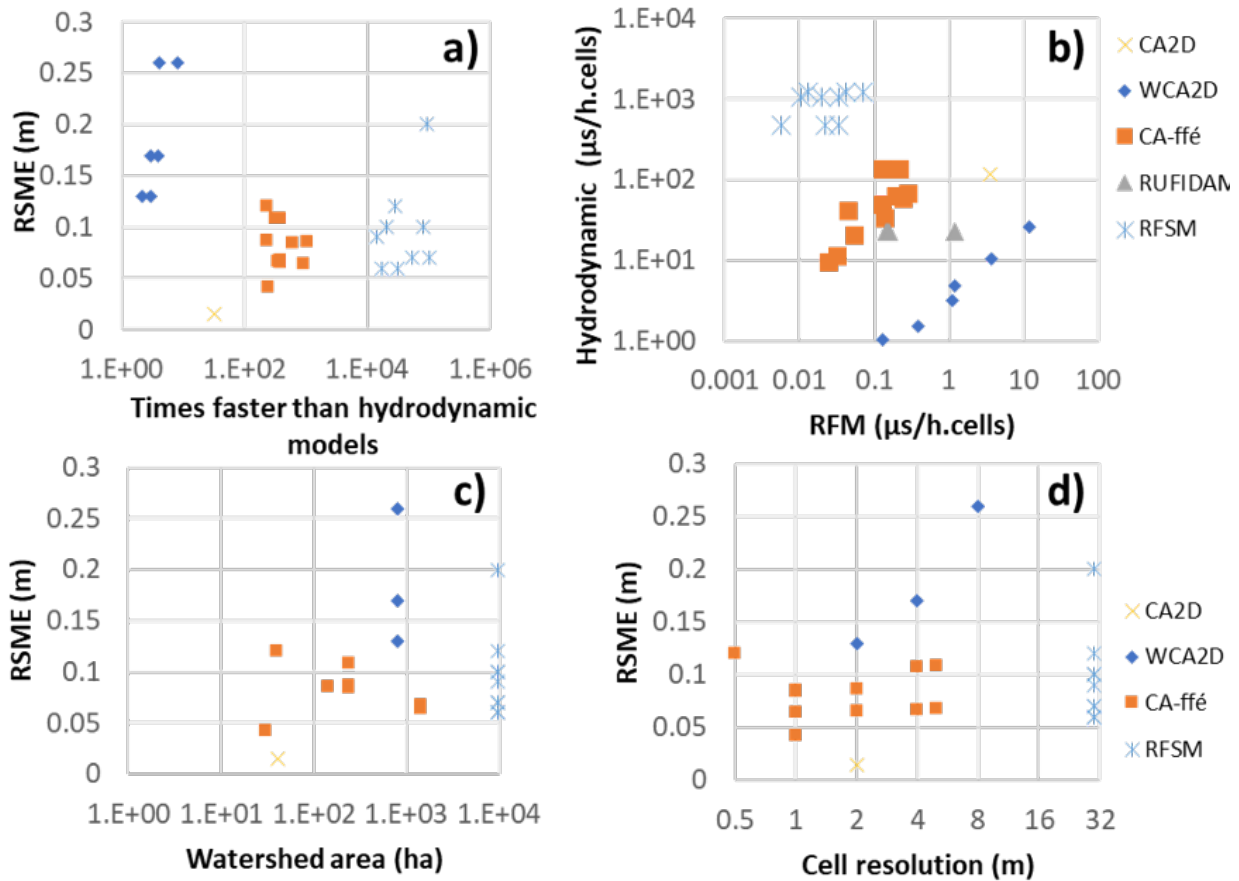
Figure 2 – Review of RFM performances

Despite the significant computational gains, the simplifications assumed by RFM reduce the accuracy of flood predictions. For instance, Jamali *et al.* (2018) observed that areas with high momentum and velocities showed more significant errors than hydrodynamic outputs. Moreover, low time-steps may be required in locations with high velocities and DEM and fine resolution to meet Courant number requirements, leading to longer simulation times Guidolin *et al.* (2016). Improving the accuracy of such models would require additional and more complex rules, which inherently increase the computational time.

1.3 Artificial Neural Networks Applied for Flood Predictions

The use of Artificial Neural Networks (ANNs) has gained prominence in flood estimation studies due to their computational efficiency and ability to learn complex patterns (PETERS; SCHMITZ; CULLMANN, 2006; PANAHI *et al.*, 2021; BOMERS *et al.*, 2019). ANNs are models inspired by the neural structure of the human brain. They are comprised of interconnected nodes, known as neurons, that process and transmit information. Each set of neuron forms a layer. A Multi-Layer Perceptron (MLP) structure

is one of the most basic ANN types, exemplified in Fig. 3a. A MLP is a feedforward ANN with various layers connected by weighted pathways. It encompasses an input layer that receives the input data, with each neuron representing an individual feature. Following this, there are hidden layers that transform this data using activation functions, such as *sigmoid*, Rectified Linear Unit (ReLU), Leaky Rectified Linear Unit (Leaky ReLU) and hyperbolic tangent (tanh). Each of the neurons in a MLP receives a correspondent bias (b), adn all connections between neurons receives a weight (w). The information flow though a neuron is exemplified in Fig. 3b. The values of b and w are fund during the ANN training process. Finally, the output layer delivers the network's predictions, adjusting its neuron count based on the task, from single neurons in the case of regression to multiple when the task is classification.
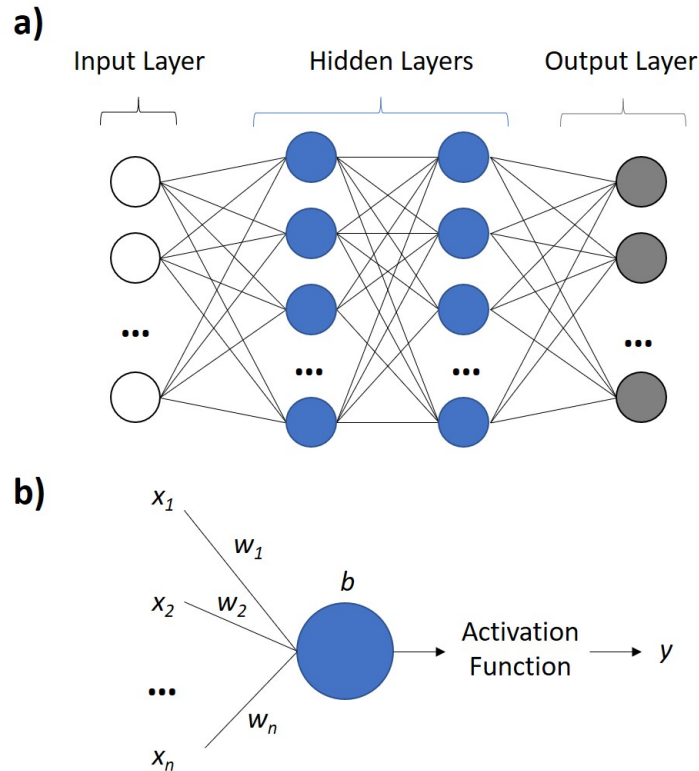
Figure 3 – Illustration of a MLP

Various researchers have successfully applied different forms of ANNs, such as MLPs, Convolutional Neural Networks (CNNs), and Recurrent Neural Networks (RNNs) to simulate flood dynamics, produce flood probability maps, and reconstruct historical flood events. These models have demonstrated high accuracy and have greatly reduced the computational time compared to traditional hydrodynamic models (PETERS; SCHMITZ; CULLMANN, 2006; KABIR *et al.*, 2020; BERKHAHN; FUCHS; NEUWEILER, 2019).

However, a common limitation observed across these studies is the lack transferability (of generalization) of ANN models in regions beyond their training datasets

or under different rainfall (KABIR *et al.*, 2020; BERKHAHN; FUCHS; NEUWEILER, 2019), which often necessitates separate models for different conditions and significantly hampers their versatility. In addition, the effectiveness of the model's architecture and hyperparameters may vary when applied to different regions (KABIR *et al.*, 2020). Further, any modification in the study domain requires updates to the physical flood model and new simulations for training new ANNs, which is a significant drawback (BERKHAHN; FUCHS; NEUWEILER, 2019). The incapacity of generalizing to different areas puts a significant barrier to applying ANN to large domains, which would required the development of extensive and detailed flood models to train the ANN. Furthermore, different DL models might be needed according the the modling purposes (e.g. fluvial and pluvial mapping). Therefore, ANN covering a large area, with a fine resolution, may result in a vast number of parameters which makes the training process slower and more complex.

Deep learning (DL) that is capable of generalizing flood predictions can facilitate DL application in large areas. In this sense, ANN can be trained with multiple smaller domains to be applied to across different locations to cover a wider studied area. Recent developments in ANN demonstrate that this data-driven strategy has the ability to generalize in several domains. For instance, LOWE *et al.* (2021) trained a U-net based ANN to forecast the maximum flood depths (U-Flood). U-Flood was trained with outputs from a hydrodynamic model created for a single watershed. In their study, 20% of the domain was divided up for testing in the U-Flood model. As a result, they could predict flooding outside training regions for various rainfall amounts, although U-Flood tended to underestimate inundated areas drastically. In addition, U-Flood wasn't evaluated for completely untested catchments. Their approach used specific watershed characteristics, such as aspect, so their model was not created with a focus on generalization. On the other hand, GUO; MOOSAVI; LEITÃO (2022), used WCA2D to simulate a 100-year flood in many catchments. The authors trained a CNN-based model to forecast maximum depths and velocities. Their findings demonstrated CNN's ability to generalize for various catchments. However, their strategy can only predict 100-year storms and doesn't make any generalizations regarding different boundary conditions (e.g., different inflows and rainfall magnitudes). Lago *et al.* (2023) developed a conditional generative adversarial for rapid flood predictions (cGAN-Flood), capable of generalizing to different catchments and rainfall magnitudes. Given cGAN-Flood's generalization capabilities, it is a promising method for large-scale predictions.

1.3.1 cGAN-Flood

GANs include a generator ($\mathcal{G}$) and a discriminator ($\mathcal{D}$), that competes during training. $\mathcal{D}$ is trained to differentiate the $\mathcal{G}$'s prediction from the ground-truth, $\mathcal{G}$ is trained to "fool" $\mathcal{D}$ by passing its output as the ground-truth (GONOG; ZHOU, 2019; WANG *et al.*, 2017). This compatition between generator and discriminator enhances the generators'

capacity to create more realistic predictions (WANG *et al.*, 2017). Traditional GANs use random noises as inputs for generating the final images. conditional GANs (cGANs) use labels that guide the generators in creating the final outputs.

According to Lago *et al.* (2023), cGAN-Flood uses two cGANs to distribute a target runoff volume (vt) over a given are to create maximum depth pluvial flooding maps. The summary of the whole method is shown in Fig. 4. A first generator (Generator 1), which uses elevation, flow accumulation, slope, and imperiousness maps, is trained to rank what cells in the domain are likely to be flooded first. A threshold τ is applied to this map to identify whether a cell is flooded or not. In this case, a cell will be considered wet if it is ranked above the threshold. Finally, a second generator (Generator 2) is trained to calculate the depths of the wet cells to create the depth map. The Pix2Pix (ISOLA *et al.*, 2017) was the approach used to develop the cGAN-Flood. The generators are a U-Net-based ANN that uses convolution and deconvolution layers. Details on the generator architectures and both discriminators used during training can be seen in (LAGO *et al.*, 2023).

The map constructions with the generators are done by assembling results from individual patches covering a portion of the domain. The reason is that convolutional neural networks (the base of the generators in this study) require fixed input size issues. The fixed input size is a major issue for scale-dependent problems (MARTINS *et al.*, 2020). Previous research used boundary conditions (such as hydrograph or precipitation) for specific convolutional neural networks (CNN) patches to predict floods (GUO; MOOSAVI; LEITÃO, 2022; LOWE *et al.*, 2021). Consequently, the interaction between patches is lost, making a comprehensive analysis of the entire domain—such as upholding the conservation of mass difficult. As a result, the method of using patches to anticipate floods hinders the creation of physics-driven ANN models.

The dual generator approach of cGAN-Flood overcomes these issues by creating the full domain map before applying the boundary conditions. The flood magnitude of a given rainfall event can be estimated by adjusting τ, and consequentially the number of wet cells. In other words, the cGAN-Flood method must automatically identify the value of τ representing the event magnitude.

The total volume to be distributed is v_t is used as input to cGAN-Flood. This volume is calculated with the sum of runoff volume flowing inside the catchment which can be estimated via water balance with hydrological simulations. cGAN-Flood then interactively modifies τ so that the total volume of Generator's 2 output (v) matches v_t. The Golden Search was the algorithm used to optimize the τ to minimize the difference between v) and v_t. The simulation ends when the error between v and v_t is below a pre-defined tolerance.

cGAN-Flood demonstrated an average speed increase of 250 times compared
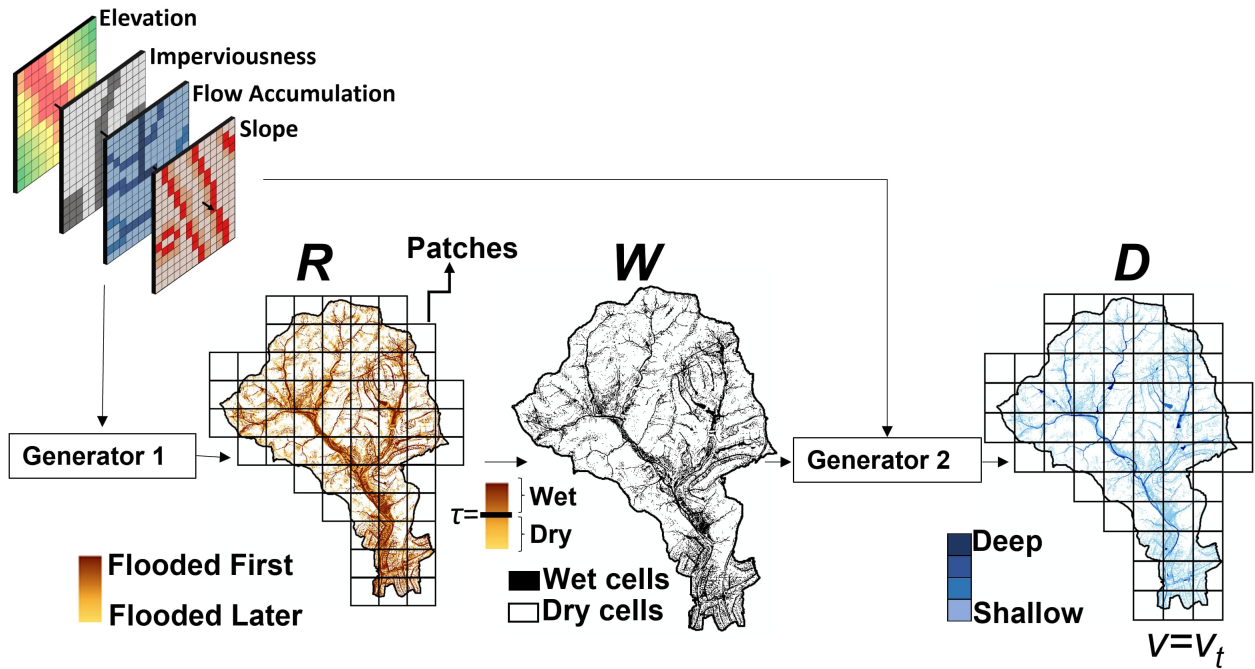
Figure 4 – cGAN-Flood Method Applies Two Generators. Source: adapted from Lago *et al.* (2023)

to the Hydrologic Engineering Center's River Analysis System (HEC-RAS) 2D models (BRUNNER, 2016) for the studied area where cGAN-Flood was developed and tested. The cGAN-Flood was designed to distribute a pre-defined flood volume to generate flood maps and was found to generalize well for various rainfalls and catchments. Nevertheless, the model's testing was limited to catchments smaller than 500ha, leaving its performance unverified for large-scale modeling. Furthermore, the training and testing catchments are located in San Antonio (Texas), and the cGAN-Flood capability of generalizing to other regions with distinct spatial characteristics has yet to be verified. Finally, cGAN-Flood has not been trained to predict fluvial flooding with draining areas larger than 500ha.

1.4 Objectives

Literature shows that there is still a need for improved methodologies to enhance rapid flood predictions, especially regarding high-resolution flood plains in large-scale watersheds (over hundreds of square kilometers). The advancement in DL predictions for such purposes can contribute to real-time predictions, climate change, and optimization studies. Therefore, the main objective of this thesis is to **advance DL modeling applicability in large-scale domains**. The following research objectives were accomplished to achieve the main goal:

1. Adapt cGAN-Flood to predict large-scale pluvial flooding.

2. Test cGAN-Flood prediction performance in areas with spatial characteristics that differs from its training locations.

3. Develop a 1D ANN flood model for fluvial flood estimation, focusing on flood mapping generalization.

In Chapter 2, cGAN-Flood was applied to enhance a coarse HEC-RAS model, a grid-based model, of the Upper San Antonio Watershed (UPSA) and generate high-resolution flood maps for watershed scale. Chapter 3 evaluated cGAN-Flood's capacity to reproduce high-resolution flood maps in Sao Paulo catchments. Furthermore, cGAN-Flood was used to increase the flood mapping resolution of Hydropol2D, a raster-based model, at Aricanduva Watershed. Chapter 4 introduced an innovative flood map prediction model using ANNs, with DEMs and inflows as its sole inputs. This model solves was trained with 1D hydrodynamic simulations for predicting fluvial flooding. Chapter 5 finally summarizes the main findings of the thesis, with the main advantages and disadvantages of the DL models with suggestions for future improvements.

2 COUPLING CGAN-FLOOD WITH A MESH-BASED FLOOD MODEL FOR EVALUATING ITS SCALABILITY FOR RAPID FLOOD PREDICTIONS

ABSTRACT

Deep learning (DL) models has shown to be an efficient alternative to hydrodynamic models for faster flood predictions. However, the application of DL for detailed flood predictions in large areas is hampered due to the low generalization capacity of existing DL models. This chapter aim to narrow address this gap by improving flood mapping resolution derived from coarse mesh-based flood models at a watershed scale. We have used cGAN-Flood, a conditional generative adversarial-based model (cGAN), that showed good performance in distributing a given flood volume (v_t) in unseen catchments. A coarse 2D HEC-RAS model was created for the Upper San Antonio Watershed (about 350 km² located in San Antonio, USA), with an average cell size of 32m. The presented methods were evaluated against a 3m resolution HEC-RAS model. Results indicate that the DL model considerably improved flood map accuracy. The generalization capacity of cGAN-Flood allowed large-scale prediction without needing to train the DL model for the entire area, illustrating how DL can enhance the resolution of existing coarse models.

2.1 Introduction

Floods are the most expensive natural disasters in terms of human and economic losses (BULTI; ABEBE, 2020; NATARAJAN; RADHAKRISHNAN, 2019). Furthermore, climate change may intensify these effects by increasing the frequency and severity of extreme storm events (AICH *et al.*, 2016; CLAVET-GAUMONT *et al.*, 2017; YIN *et al.*, 2018; LAGO *et al.*, 2021b). Flood modeling is vital for urban flood mitigation planning and design. In particular, concerns regarding pluvial flooding in urban areas have increased in the past two decades (RANGARI *et al.*, 2018). Although coastal and river are generally larger and most durable types of flooding, pluvial flooding may cause more damage to properties due to its higher occurrence frequency (SZEWRAŃSKI *et al.*, 2018). Two-dimensional 2D models are the most effective type of hydrodynamic model applied to urban flood predictions (CEA; COSTABILE, 2022), and are traditionally used for predicting pluvial flooding (BULTI; ABEBE, 2020). However, these models are computationally costly, limiting their use in large watersheds, optimization problems requiring numerous runs, and real-time predictions. Traditionally, large watershed modeling with 2D hydrodynamic models leverages coarse cell resolution. This approach curtails the number of computational nodes, enabling simulations to conclude within a manageable time frame. However, coarser cell resolution reduces the accuracy of flood mapping (CHEN *et al.*, 2012), especially in urban areas where the local topology is misrepresented (FEWTRELL *et al.*, 2008).

Rapid Flood Models (RFMs) are an alternative to hydrodynamic models for faster predictions. RFMs reduce simulation time by employing simplified hydraulic concepts, such as cellular automata (JAMALI *et al.*, 2019), instead of complex physical equations (TENG *et al.*, 2017). Although they offer computational speedups, their accuracy is diminished due to simplifications assumed for the simulations.

Deep learning (DL) can be used to model complex hydrodynamic iterations while maintaining computational efficiency. These DL models employ multi-layered structures called Artificial Neural Networks (ANN) to handle complex representations and learn from high-dimensional data (SIT *et al.*, 2020). While DL-based models have demonstrated promising results in flood prediction (BERKHAHN; FUCHS; NEUWEILER, 2019; DTIS-SIBE *et al.*, 2020; LOWE *et al.*, 2021; HOFMANN; SCHÜTTRUMPF, 2021), they are usually domain-specific and their capacity to reproduce flood predictions outside the training dataset is restricted. The lack of generalization is still a major challenge for the use of DL models in practical applications (KARIM *et al.*, 2023). Particularly in large area modeling, the inability to generalize the flood predictions requires training a DL model for the entire domain, which can be challenging as the training process is time-consuming and requires a significant amount of data (BENTIVOGLIO *et al.*, 2022).

Literature shows improvements in DL models' ability to generalize outside the training areas. Lowe *et al.* (2021) applied a U-Net-based DL approach to predict maximum water depths with local topological features and inputs and rainfall as inputs. They trained their model on portions of the study area and were able to predict maximum water depths in unobserved parts of the same domain. However, the capacity to generalize to other catchments still needs to be evaluated. Guo, Moosavi e Leitão (2022) developed a similar DL model, trained with a cellular automata model (GUIDOLIN *et al.*, 2016) for water depths and flow velocities predictions in different catchments. Despite the model's ability to generalize to unseen catchments, their method does not generalize for different rainfall events. (LAGO *et al.*, 2023) used a conditional generative adversarial network (cGAN) for pluvial flood modeling (cGAN-Flood), which was, on average, 250 times faster than Hydrologic Engineering Center's River Analysis System (HEC-RAS) (BRUNNER, 2016). cGAN-Flood distributes a pre-defined flood volume to generate the flood map and could generalize to different rainfalls and catchments. However, this model was tested for catchments smaller than 500ha. Therefore, its performance on large modeling still needs to be evaluated.

Despite the advances in the generalization capacity of DL flood models, the applicability of DL models for large predictions has yet to be shown in the literature. To tackle this gap, our study introduces a pioneering application of DL models to enhance the resolution of flood mapping derived from coarse hydrodynamic models. We exemplify our methods with a coarse HEC-RAS model, a grid-based model, which provides cGAN-Flood

with the total volume to be distributed. This approach unveils the potential to enhance the resolution of flood mapping in pre-existing large 2D hydrodynamic models.

The chapter is organized into Methodology, Results and Discussions, and Summary main sections. The methodology introduces the cGAN-Flood model, by describing how this DL model works, describing the HEC-RAS model of the watershed, and the metrics used to evaluate cGAN-Flood's performance. In the results section, we compare coarse and fine flood maps are and demonstrate how the DL model can improve flood mapping predictions. In the conclusions, we summarize the main findings of this chapter, with advantages, disadvantages, and opportunities for future research.

2.2 Methodology

2.2.1 cGAN-Flood

In this chapter, we used the cGAN-Flood (LAGO *et al.*, 2023) DL model to increase the resolutions of flood maps generated from a grid-based model. This DL model works by distributing a given flood volume over a given area, which can be calculated using low-resolution flood models. The overall methodology is presented in Fig. 5.

For generating high-resolution flood maps in a large domain, cGAN-Flood was coupled with coarse flood models. This model calculates and routes excess precipitation, providing cGAN-Flood with v_t. In this case, the primary concern is not the hydraulic behavior of the runoff within these coarser cells but rather their maximum stormwater volume in each cell. Although hydrodynamic models may produce unrealistic flood maps at low resolutions, they still maintain a proper water balance and flow between cells as a physically-based model, provided that stability issues are addressed.

2.2.2 Upper San Antonio Watershed

First, we applied cGAN-Flood to improve flood mapping resolution from a coarse 2D HEC-RAS model, version 6.2 Brunner, created for the Upper San Antonio (UPSA) Watershed. This coarse HEC-RAS model provides cGAN-Flood with the flood volume to be redistributed (v_t) for a high-resolution flood map output. This watershed contains 1 training, two validation, and two testing of the catchments used for cGAN-Flood development and evaluation (Fig. 29a). (LAGO *et al.*, 2023) showed that, although most of the training areas are located inside the Leon Creek watershed, cGAN-Flood performed satisfactorily on catchments inside UPSA.

The HEC-RAS domain has an area of approximately 350 km^2 with a base cell size of 100m. The terrain used for the simulations has a 3m resolution, downsampled from a 1m resolution DEM acquired with the San Antonio River Authority (SARA,2017). Breaklines were added for the reaches with a flow accumulation area larger than 100ha. Breaklines
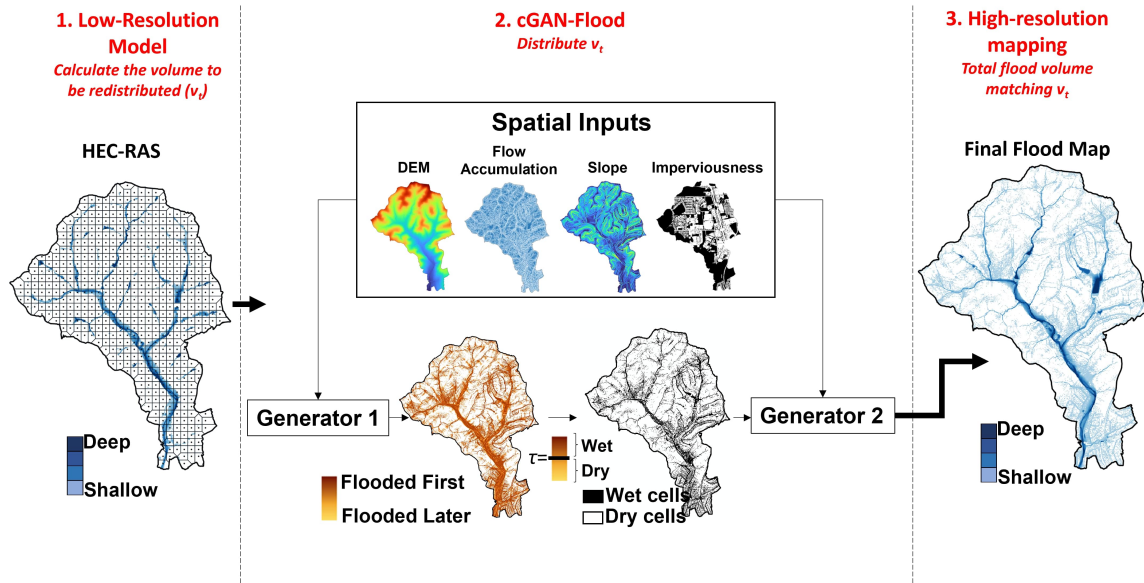
Figure 5 – The overall methodology includes the calculation of flood volumes with low-resolution models (1), which are distributed with cGAN-Flood (2) to generate high-resolution flood maps (3).

are modeling elements used to align the faces the the cells in a mesh with key features in the terrain (e.g. high grounds and river centerlines). Adding breaklines improves the model representation of the terrain and the water movement between cells. We selected a cell size of 15m for these breaklines to improve the discretization in areas with high flows to predict more accurately the flood dynamics. We added near repeats so that the 15m cells cover the entire reach width where necessary. Additional breaklines were added for the transportation infrastructure in UPSA watershed. A polyline file with the transportation infrastructure of San Antonio was acquired from the City of San Antonio (2023). Due to the coarser cell sizes, leakages between cells may occur if their faces need to be correctly placed in high-ground elevations. By adding and enforcing breaklines correspondent to streets and roads, the water flow is better represented with a more accurate v_t used with cGAN-Flood. After adding the breaklines, the average cell size of the HEC-RAS models is 32m. Furthermore, underground drainage infrastructure, such as culverts and pipes, was burned into the terrain with their corresponding width to allow hydraulic connectivity across the domain. A polyline with the underground drainage system and its characteristics was also downloaded from City of San Antonio (2023).

A Manning's n of 0.035 $m^{1/3}s^{-1}$ was used for impervious areas and channels and 0.1 $m^{1/3}s^{-1}$ for pervious areas, which is the standard Manning's n used for training cGAN-Flood (LAGO *et al.*, 2023). A 1m resolution map with imperviousness areas, acquired with the San Antonio River Authority (SARA,2017), was also downsampled to 3m. The curve number was the infiltration method used in this model. The CN values from 155 sub-catchments were acquired from a UPSA HEC-HMS, available at D2MR website, which
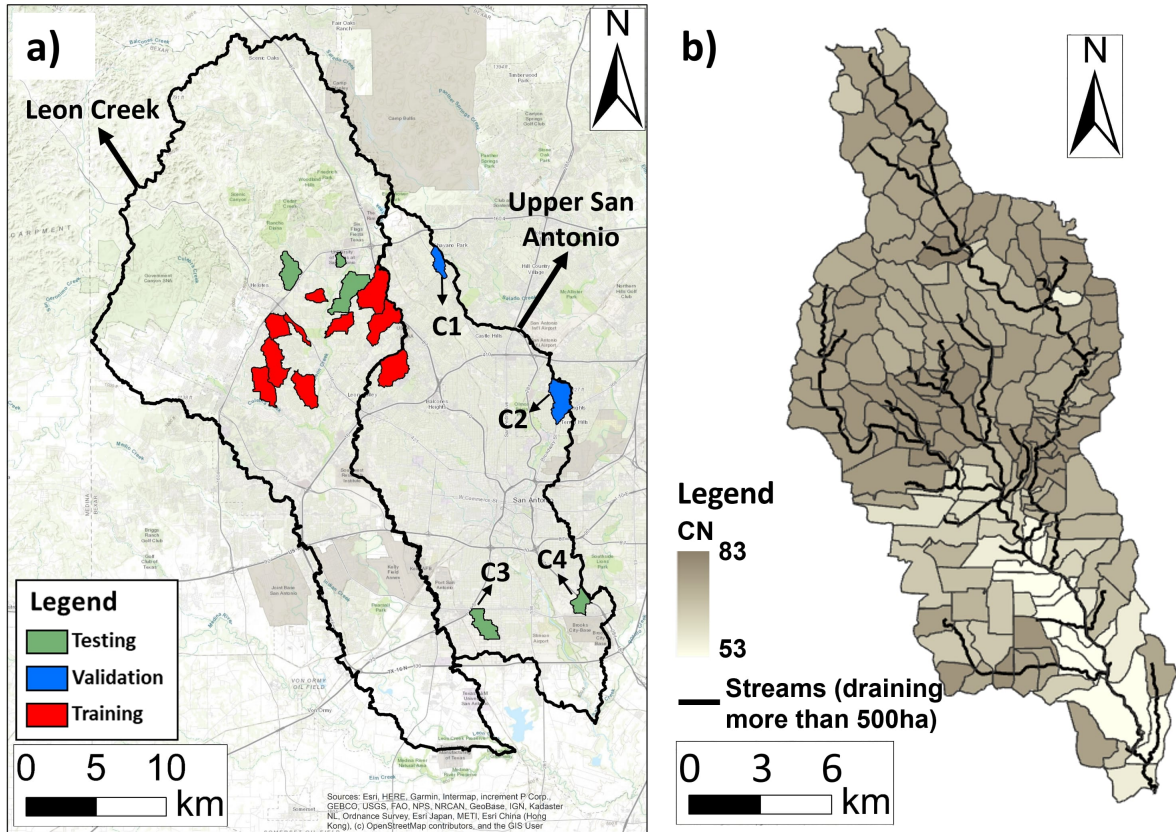
Figure 6 – UPSA watershed with cGAN-Flood training, validation and testing areas (a); and streams, sub-catchments and CN values (b). Source: (LAGO *et al.*, 2023)

focus on the dissemination of hydraulic and hydrological, shown in Fig. 29b. In this study, no calibration attempts were performed, as the focus of the paper is demonstrating how DL models can be used to improve flood mapping resolution. Different model parametrization could affect the v_t values and the final flood maps. However, the methods applied in this paper can be reproduced with any other mesh-based model configuration and parameters.

When applying cGAN-Flood for flood volume redistribution in the UPSA, the process is conducted independently across the 155 HEC-HMS sub-catchments. The total flood volume (v_t) for each sub-catchment is calculated by summing the volumes of all cells within it. Since mesh cell delineation does not always coincide with sub-catchment borders, cells on the boundaries of two sub-catchments may extend into both areas. To address this, we redraw the sub-catchments to align with cell faces, ensuring each cell lies entirely within a single sub-catchment for the purpose of v_t redistribution. v_t is calculated via elevation-volume tables after acquiring the maximum WSE of each cell. This process is done automatically by reading the hfd plan file of HEC-RAS (see SM.1 for further details).

Notably, cGAN-Flood was neither trained nor tested for areas larger than 500ha. As such, we did not redistribute fluvial flooding from segments receiving stormwater from larger areas, as previous analysis showed that cGAN-Flood was unable to predict floods

accuratly in such conditions. To do so, we exclude fully flooded cells adjacent to a flow line with a flow accumulation exceeding 500ha (Fig. 6b) from the redistribution process. The flood depths for these cells, as determined by the low-resolution HEC-RAS, are maintained in the final maps. Considering that fluvial flooding can be accurately and rapidly simulated with 1D models in most situations, our primary objective is to enhance the resolution of pluvial flood maps, which necessitates 2D modeling.

2.2.2.1 Performance Analysis in San Antonio Catchments

High-resolution HEC-RAS mapping of the whole UPSA was unfeasible due to computational resources and simulation time. Simulating the UPSA with a 3m cell size would result in approximately 39 million cells, which would not be supported due to a lack of computational memory. In addition, the simulation time would be unpredictable. Therefore, we have tested the performance of cGAN-Flood to improve the flood mapping resolution of HEC-RAS model in catchments C1, C2, C3, and C4 (Fig. 29a). HEC-RAS models with a 3m resolution were created for each catchment to be used as ground truth. Then, coarse HEC-RAS models were created for calculating v_t. The same methodology used for selecting cell sizes, applying breaklines, and adding terrain modifications in UPSA, was used in these catchments. The 25 and 100-year storms, with a 3-hour duration (LAGO *et al.*, 2023), were used to evaluate the performances.

We have simulated the 100-year storm in the whole UPSA to estimate the simulation time of cGAN-Flood and perform a visual comparison between low-resolution HEC-RAS and cGAN-Flood maps. Although we could not compare the whole UPSA with the high-resolution HEC-RAS, simulation time is still a relevant performance metric when simulating large domains.

2.2.3 Performance Metrics

We used a combination of the mean absolute error (MAE), root mean square error (RMSE), and the Nash-Sutcliff efficiency (NSE) to assess the spatial accuracy of low-resolution flood maps with and without applying cGAN-Flood, for all cells with depths equal or larger than 0.01m. We also utilized the hit rate (HR), false alarm rate (FAR), and the critical success index (CSI) to evaluate the accuracy of the predicted flooded areas. The metrics HR, FAR, and CSI are expressed as percentages, ranging from 0% to 100%. The optimal value for HR and CSI is 100%, while for FAR, it is 0%. The formulas for these metrics are as follows:

$$\text{HR} = \frac{\text{Hits}}{\text{Misses}} \tag{2.1}$$

$$\text{FAR} = \frac{\text{Hits}}{\text{Hits} + \text{False Alarms}} \tag{2.2}$$

$$\text{CSI} = \frac{\text{Hits}}{\text{Hits } + \text{ False Alarms} + \text{Misses}} \qquad (2.3)$$

In this context, 'hits' represent cells identified as flooded by both models, 'false alarms' denote cells flagged as flooded solely by cGAN-Flood, and 'misses' are cells recognized as flooded exclusively by the high-resolution HEC-RAS. We adopted thresholds of 0.01m, 0.05m, and 0.3m for distinguishing between dry and wet cells, in line with previous flood studies (BROWN; SPENCER; MOELLER, 2007; SHI *et al.*, 2021; JAMALI *et al.*, 2018; GUIDOLIN *et al.*, 2016; LOWE *et al.*, 2021), to better evaluate the performances under different depth magnitudes. HR and FAR were calculated only for a threshold of 0.05m (HR05 and FAR05), which is the mid-magnitude of the selected ones. The CSI metric was calculated with depth thresholds (CSI01, CSI05, and CSI3), as this measurement accounts for both false alarms and misses.

2.2.4 Hardware Specifications

All cGAN-Flood simluations NVIDIA GeForce RTX 2060 SUPER GPU (1650 MHz and 8GB of memory). Given that the HEC-RAS model lacks GPU support, its hydrodynamic computations were carried out using an i7 10700 CPU operating at 2.9GHz.

2.3 Results and Discussion

2.3.1 Model performances at San Antonio

First, we evaluated the capability of the low-resolution HEC-RAS model to predict maximum flood volumes. Table 1 shows that the volume calculated with the low-resolution HEC-RAS model, which was used as input to cGAN-Flood, matches the volume predicted with high-resolution HEC-RAS relatively well. The largest error in volume was an underestimation of approximately 10% for catchment C1 (25-year storm). The average error of all simulations is -6.7%. This table also demonstrates that low-resolution HEC-RAS tends to underestimate flood volume, meaning that the stormwater flows out of the catchment faster than simulated with a high-resolution model. One possible explanation is leakages from the coarse cells, which cause water to skip high-ground terrains and reach the outlet faster.

Flood maps were created for the four sub-catchments in the UPSA watershed with low and high-resolution HEC-RAS models and with cGAN-Flood. Table 2 shows the metrics for the low-resolution and cGAN-Flood outputs for the 25 and 100-year storms.

When comparing the two models, based on the metrics of False Alarm Rate (FAR), Hit Rate (HR), and the Critical Success Index (CSI), we observe that cGAN-Flood generally outperforms low-resolution HEC-RAS, except for FAR. Fig. 7 illustrates flood

Table 1 – Comparison of total flood volume calculated from low and high-resolution HEC-RAS models

Storm	Catchment	Volume high-resolution HEC-RAS (1000m3)	Volume low-resolution HEC-RAS (1000m3)	Error
25-year	C1	116.5	104.3	-10.4%
	C2	289.8	273.5	-5.6%
	C3	118.9	113.7	-4.4%
	C4	223.9	211.9	-5.3%
100-year	C1	139.4	125.6	-9.9%
	C2	348.8	330.3	-5.3%
	C3	142.7	132.8	-6.9%
	C4	270.6	255.3	-5.6%

Table 2 – Performance metrics of low-resolution HEC-RAS and cGAN-Flood

	Storm	Catchment	FAR05	HR05	CSI05	CSI	CSI3	RSME (m)	MAE (m)	NSE
Low Resolution HEC-RAS and cGAN-Flood	25-year	C1	23%	90%	71%	83%	74%	0.07	0.013	0.75
		C2	23%	91%	72%	80%	61%	0.07	0.019	0.70
		C3	19%	90%	74%	84%	66%	0.06	0.014	0.76
		C4	19%	87%	72%	80%	63%	0.09	0.013	0.73
	100-year	C1	20%	90%	73%	84%	76%	0.07	0.014	0.78
		C2	22%	92%	73%	81%	62%	0.08	0.022	0.72
		C3	17%	91%	76%	86%	65%	0.07	0.016	0.77
		C4	17%	88%	75%	82%	66%	0.08	0.014	0.75
Low Resolution HEC-RAS	25-year	C1	27%	40%	35%	30%	67%	0.05	0.018	0.67
		C2	17%	47%	43%	35%	62%	0.07	0.023	0.64
		C3	15%	46%	42%	36%	57%	0.06	0.022	0.63
		C4	23%	49%	42%	35%	51%	0.07	0.019	0.59
	100-year	C1	14%	37%	35%	28%	78%	0.05	0.016	0.74
		C2	15%	48%	44%	36%	62%	0.07	0.026	0.66
		C3	13%	50%	46%	41%	60%	0.06	0.023	0.67
		C4	19%	49%	44%	36%	55%	0.08	0.021	0.63

mapping outputs from the low-resolution HEC-RAS and cGAN-Flood, which indicates that the DL model significantly improved flood mapping.

The cGAN-Flood could improve the HR, CSI, and CSI0.01 by 44%, 31%, and 48%, respectively. The improvement in CSI0.3 (deeper depths) was less significant, about 5%. The reason is that deeper water is more frequently present along the channel, which was better captured in the low-resolution HEC-RAS model, demonstrated by better CSI0.3 metrics compared to CSI0.05 and CSI0.01. Furthermore, cGAN-Flood, and other DL models, tend to show lower performance when analyzing CSI0.3m. For FAR, which measures the proportion of false positives in the total predicted positives, low-resolution HEC-RAS consistently has a lower average FAR (with an average of 18%) across all

locations compared to cGAN-Flood (an average of 20%). The reason is that HEC-RAS consistently underestimated shallower depths across these sub-catchments, reducing false negatives.
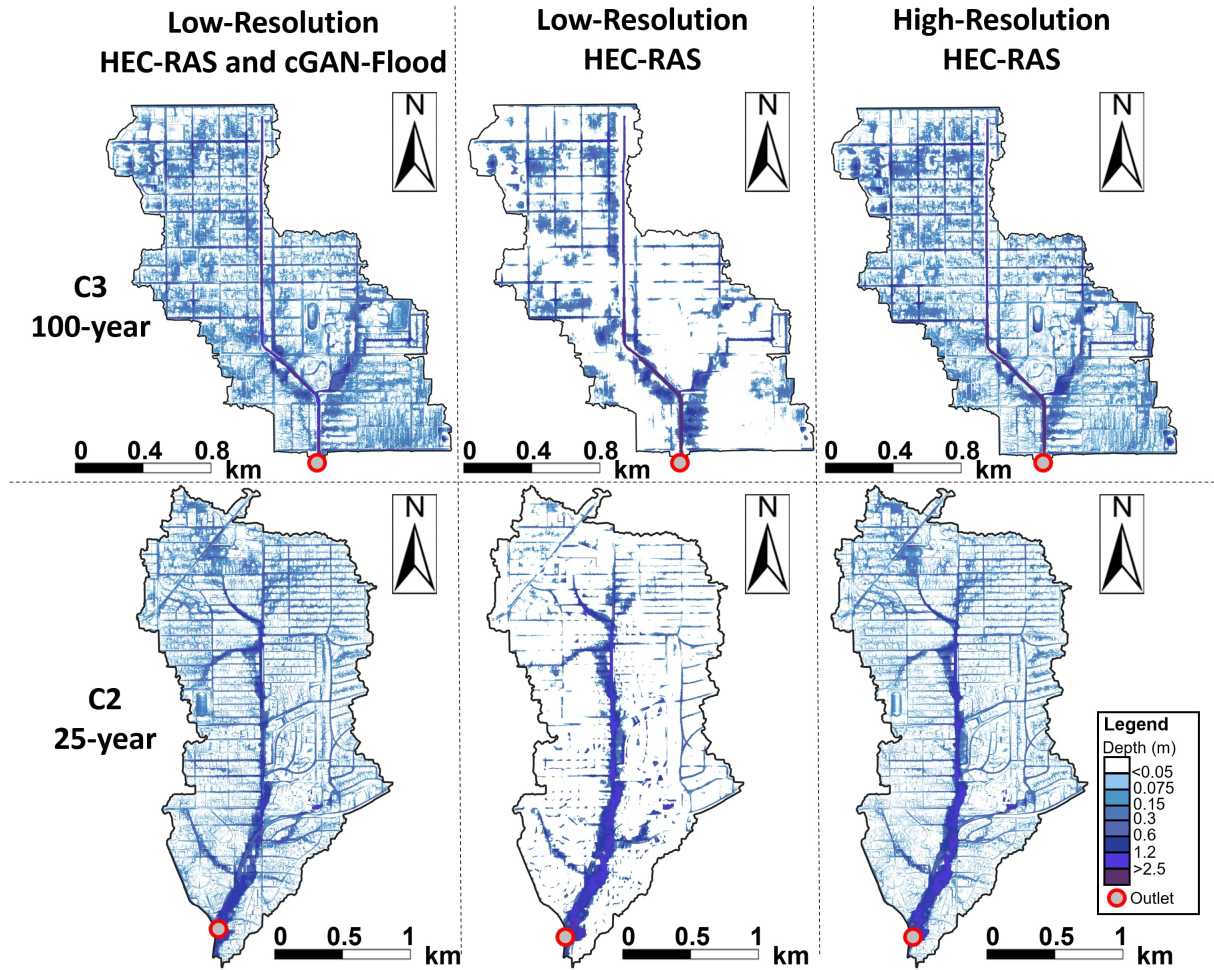
Figure 7 – Comparisson between flood maps generated from low-resolution HEC-RAS model and cGAN-Flood with high-resolution HEC-RAS outputs

In addition to improving the flooded areas, cGAN-Flood also improved the flood depths across the domains, as demonstrated with MAE and NSE metrics. The DL model decreased the MAE from an average of 0.15 m to 0.13m and improved the NSE from 0.66 to 0.75. Fig. 8 illustrates the difference between the cGAN-Flood and low-resolution HEC-RAS to the high-resolution one. It can be observed that, in general, the errors are closer to zero with cGAN-Flood when compared to low-resolution HEC-RAS. However, Fig. 8 also shows that cGAN-Flood presented some localized areas with more expressive errors (e.g., near the outlet of area C4). When comparing low- and high-resolution HEC-RAS outputs, the flood depths are expected not to deviate significantly, as we are comparing outputs generated with the same set of hydrodynamic equations and solver strategy.

Consequently, the RSME increased by an average of 0.008m after applying cGAN-Flood, as the more significant errors are magnified with the root operation of this metric.
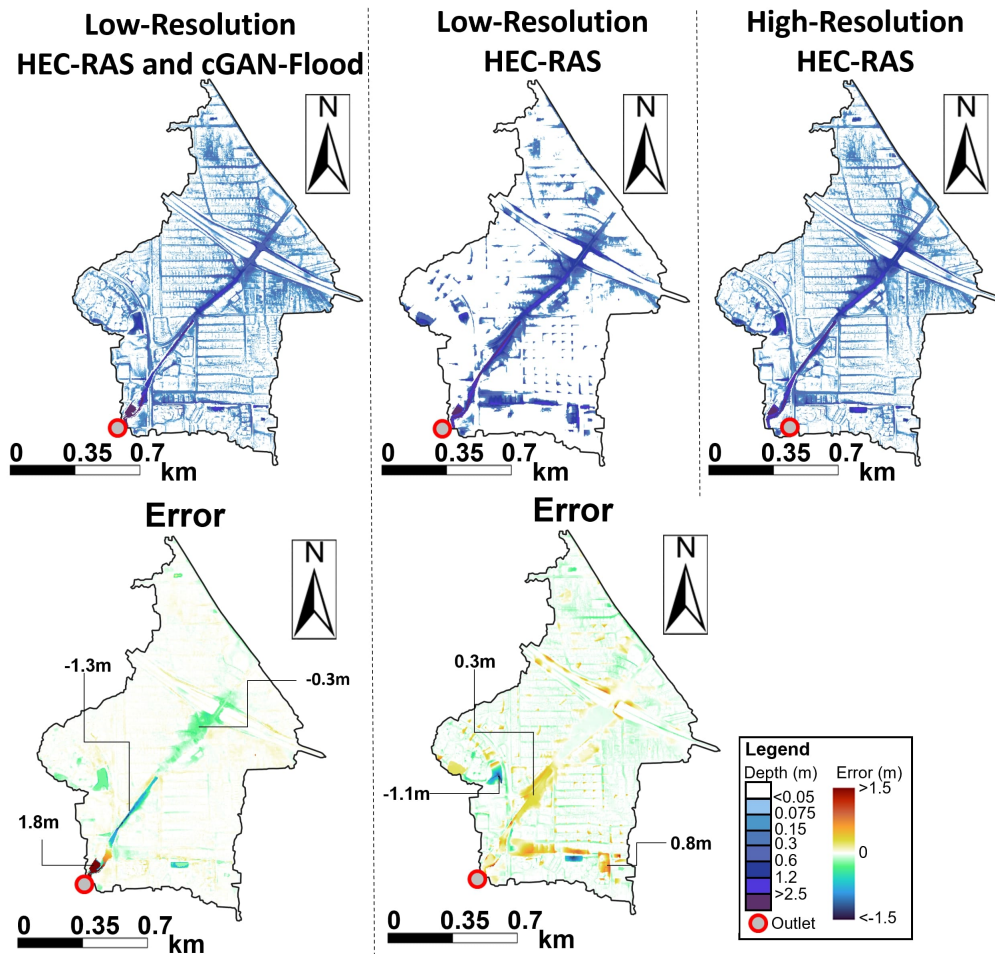
Figure 8 – Error depths of cGAN-Floos and low-resolution HEC-RAS maps.

2.3.1.1 High-Resolution Prediction of UPSA Watershed

The comprehensive flood maps produced by the low-resolution HEC-RAS model, enhanced by the cGAN-Flood volume redistribution, are displayed in Fig. 8. Integrating a low-resolution hydrodynamic model and cGAN-Flood led to significant enhancements in flood map predictions throughout the UPSA watershed, particularly in depicting shallower depths. Such details regarding shallow cells can provide valuable insights to local authorities during emergencies. For instance, vehicular aquaplaning can occur at speeds of 70km/h or 62km/h when water depths reach 0.01m and 0.02m, respectively (OH *et al.*, 2008). More precise flood maps can enhance the effectiveness of responses, such as evacuation strategies, and contribute to safeguarding local residents.

From a time efficiency perspective, the low-resolution HEC-RAS model (570k cells) required 31 minutes, while the cGAN-Flood volume redistribution across the entire UPSA took an additional 37 minutes. Therefore, the total computation time to generate

high-resolution flood maps for about 38 million cells was 68 minutes. In comparison, the prediction of a 25-year flood map in area C1 (approximately 150k cells) alone consumed 37 minutes. Notably, the simulation time per cell reduces with a low-resolution model, as coarser model decrease the Courant Number and allows for larger timesteps. If we presume that the computation time scales with the number of cells, a rough estimate suggests that a full HEC-RAS simulation with a 3m resolution for the UPSA would take approximately 160 hours (or nearly one week), assuming the simulation time per cell is equivalent to that of area C1. These results underscore the potential of DL models for enhancing efficiency in predictions of large areas. However, it is worth noting that the fluvial flooding in segments draining over 500ha was calculated with 15m cells in the low-resolution model HEC-RAS model. Applying finer cell sizes or a combination with a 1D HEC-RAS can improve the flood predictions at these locations, which can affect the total prediction time. HEC-RAS 1D models have been traditionally used for fluvial flood predictions and may be a preferred option for rapid flood modeling as it is less computationally demanding.
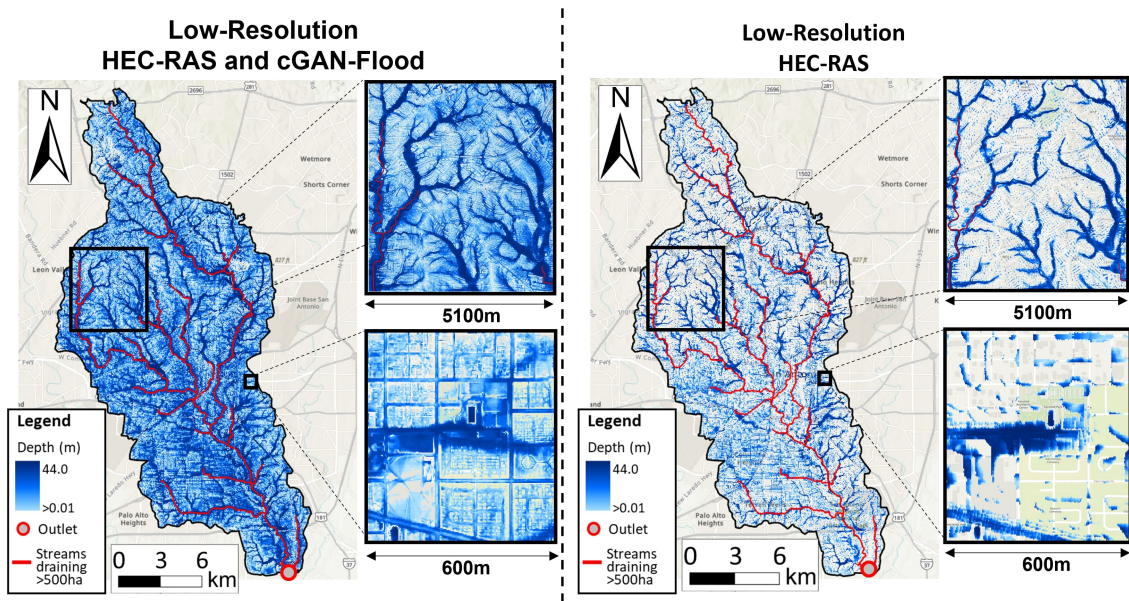
Figure 9 – Flood maps of entire UPSA watershed with a low-resolution HEC-RAS model and after coupling it with cGAN-Flood. Depths are visualized with equalized histogram for better illustration.

2.4 Conclusions and Future Model Improvements

This study addressed an important gap in the field of flood predictions in a large domain, demonstrating a pioneering application of Deep Learning (DL) models to enhance flood mapping resolution originating from coarse hydrodynamic models. This presents a significant leap toward refining flood modeling while maintaining computational feasibility. Our work showcased the use of cGAN-Flood with a coarse mesh-based hydrodynamic

model. Therefore, the methods presented in this chapter underscored the potential to ameliorate the resolution of flood mapping in pre-existing 2D hydrodynamic models.

However, some limitations of cGAN-Flood needs can be highlighted. First, the model was not trained to account for underground drainage systems. The incorporation of such systems in the model could improve its predictions, especially in urban settings where these systems are prominent and significantly influence flood dynamics. Future work should focus on expanding the model's capacity to include underground drainage systems. Also, cGAN-Flood was not evaluated with previous hydrological conditions. It is suggested to train the model with different initial soil moisture to make it sensitive to different previous climate conditions. cGAN-Flood is also strictly confined to a 3m raster resolution. The inability to adapt to finer or coarser cells restricts its application in situations where data resolution varies or in scenarios requiring more detailed flood predictions. Further adaptations should be made to enable the model to work with different resolutions, thereby broadening its application scope. Finally, cGAN-Flood was trained with models that were not calibrated and its results reproduce the outputs from generic HEC-RAS models. It is recommended to evaluate how using calibrated models to train cGAN-Flood can improve its predictions capabilities.

In conclusion, while this study presented a novel and promising approach to large flood modeling, it has also revealed pathways for future research that could further enhance the performance and applicability of DL models in flood predictions. It has not only demonstrated this technology's potential but also outlined a clear pathway for future research. Literature reveals substantial progress in utilizing DL for flood prediction in recent years, offering encouraging results for practical, real-world application scenarios in the near future.

3 EVALUATING CGAN-FLOOD TRANSFERABILITY TO CATCHMENTS WITH DISTINCT TOPOLOGICAL CHARACTERISTICS

ABSTRACT

Deep learning (DL) models for flood predictions have gained popularity. However, these models still struggle to accurately predict floods to different topologies and boundary conditions. Recently, a DL model based on a conditional generative adversarial network (cGAN-Flood) was developed with a focus on generalization to different catchments and rainfall events, trained and tested within San Antonio, Texas. Despite its satisfactory efficiency in predicting floods to unseen catchments, the tested areas are closed to training ones, with similar topological characteristics. This chapter aims to discuss cGAN-Flood methods and evaluate their accuracy for catchments in Sao Paulo. HEC-RAS models were developed for three catchments in Sao Paulo, whose results were compared to cGAN-Flood's outputs. Furthermore, we demonstrate how cGAN-Flood can be coupled with a raster-based model for enhancing resolution at the Aricanduva watershed ($150km^2$). Results showed a drop in the performance of cGAN-Flood from testing areas in San Antonio compared to the ones in Sao Paulo. The reason is the significant differences in the input data and higher slopes in Sao Paulo. Despite the drop in accuracy, cGAN-Flood was still able to predict flooding with relative efficiency, improving the overall accuracy of low-resolution Hydropol2D model.

3.1 Introduction

A key tool for designing and planning flood mitigation strategies in urban areas is flood modeling. Today, the most accurate models for predicting urban floods are two-dimensional (2D) hydrodynamic (CEA; COSTABILE, 2022). However, their applicability in large watersheds or when several runs are necessary is hampered by their high computing cost (e.g., for Monte Carlo simulation and optimization problems). Furthermore, rain-on-grid modeling, which consists in simulating flood distribution directly from rainfall inputs upon the domain, takes even longer simulation times. The reason is that with the application of rainfall, every cell in the domain contains water in which the shallow water equations (SWE) are applied to compute the flood dynamics.

In an effort to expedite flood predictions, Rapid Flood Models (RFMs) have been developed. Deep learning models (DL), including artificial neural networks (ANN), offer a potential solution for improving rapid flood predictions. ANNs, known for their learning capabilities and efficiency, have been successfully employed in numerous flood-related studies (DTISSIBE *et al.*, 2020; ZHAO *et al.*, 2020; SONG *et al.*, 2020; LE *et al.*, 2019; FANG *et al.*, 2021; PETERS; SCHMITZ; CULLMANN, 2006; SHRESTHA; THEOBALD;

NESTMANN, 2005; BOMERS *et al.*, 2019; PANAHI *et al.*, 2021; **??**; BERKHAHN; FUCHS; NEUWEILER, 2019). DL models showed promising results in reproducing hydrodynamic models, which are often data-demanding and expensive to be created.This opens the opportunity to train DL models in areas where reliable hydrodynamic models exists to be replicated in areas with low investments for such purpose. However, it is necessary to investigate the transferability of DL models between areas with distinct topological features and wether the performance can be maintained. However, generalizing flood predictions is still a challenge (BENTIVOGLIO *et al.*, 2022).

Do Lago et. al (2022) developed cGAN-Flood, which uses a conditional adversarial network (cGAN) to solve a rain-on-grid problem. This approach distributes a pre-determined flood volume over a catchment, which can be previously calculated with horological simulations. cGAN-Flood was trained and validated in different catchments in San Antonio, Texas. The generalization capabilities of cGAN-Flood were evaluated in a variety of unseen catchments, within the same city, under different rainfall magnitudes. Although the results were satisfactory, showing that the model can generalize to both boundary and topological conditions, cGAN-Flood was tested in catchments that are geographically close and with similar topological characteristics.

3.1.1   Background on cGAN-Flood Training and Validation

According to Lago *et al.* (2023), ten, two, and five testing catchments were used for the training (TR), validation (VA), and testing (TE) datasets, respectively. All these catchments are located in San Antonio, Texas, within Upper San Antonio and Leon Creek watersheds (Fig. 4a) . Most of the training sub-catchments are gathered around Leon Creek's eastern limits. The testing areas TE1, TE2, and TE3 are located closer to the training cluster than the TE4, TE5, and the validations areas. In order to evaluate cGAN-Flood under various spatial conditions, areas were chosen for testing and validation that comprise catchments with various sizes, average cell slopes, and percentages of impervious surface.

These areas presented different characteristics so that cGAN-Flood could be trained and validated under various catchment scenarios for predictions. Their size varied from 54.4 to 463.8 ha. In terms of cell-to-cell average slope, TR1 presented the highest value of 17.5°. As for the percent impervious area, the most urbanized catchment within the studied areas is 63.8 % impervious.

HEC-RAS (BRUNNER, 2016) was the hydrodynamic model used as ground-truth to train the generators. HEC-RAS 2D models with 3m grid resolution were created in for each catchment. The DEM and imperviousness map used for HEC-RAS modeling had the same resolutions. For impermeable cells, Manning's roughness coefficient of 0.03 $m^{1/3}s^{-1}$ was chosen, as suggested for concrete regions (BRUNNER, 2016), as these models were not

Table 3 – Characteristics of the testing, validation, and training areas

Location	Area (ha)	Number of Cells (x10³)	Average cell slope (°)	Impervious Area (%)
TR1	226.9	252.1	17.5	44.7
TR2	84.8	94.2	14.7	43.1
TR3	99.8	110.9	14.7	46.9
TR4	187.6	208.5	10.9	46.8
TR5	463.8	515.3	13.3	58.9
TR6	371.5	412.8	14.5	36.1
TR7	309.6	344	12.7	48.4
TR8	383.6	426.3	14.7	46
TR9	307.3	341.4	15.4	38.4
TR10	378.1	420.1	17.1	57.2
VA1	134.6	149.5	13.1	29.9
VA2	341.9	379.8	13.7	48.9
TE1	258.9	287.7	14.7	33.4
TE2	54.4	60.4	13.8	63.8
TE3	406.5	451.6	12.5	43.2
TE4	251	277.8	8.2	45.5
TE5	146.9	163.2	12.2	54.1

calibrated. For previous areas, n equal to 0.1 $m^{1/3}s^{-1}$ was selected to represent different pervious covers (e.g. bare field, grass, row crops, sparsely vegetated surfaces, and others) (ENGMAN, 1986). The HEC-RAS depth output maps were used to train generator 2 and to create the rank maps, used for training generator 1. Because the catchment areas are relatively small (under 500 ha), it is expected that spatially homogeneous precipitation will predominate. Therefore, only spatially uniform precipitation was used for training, validating, and testing cGAN-Flood. Using cGAN-Flood for larger watersheds means dividing the area into smaller sections. The deep learning model would then independently manage the volume distribution in each section. Though the rainfall might is more uniformly distributed in these smaller portions, its characteristics can vary significantly across different parts of the domain.

The rainfall used for training presented an increasing intensity Fig 9b. Therefore, the ranking map used to train generator 1 was created according to when the cells started to be flooded. In addition, depth maps were collected at different times of this event to represent different flood magnitudes when training generator 2.

Furthermore, terrain modifications were applied to each training area to make the generators sensitive to different elevations. These terrain modifications multiplied the DEM with different factors varying from 0.8 to 1.2. Therefore, the training of the generators also included catchments that were 20 % smoother and enhanced regarding the elevations. Smoothing the terrain reduces the difference in elevations between cells. It makes the catchment more prone to flooding, as the channels will be shallower and likely experience lower velocities due to lower slopes. On the other hand, enhancing the

elevation increases the overall velocity and reduces the chances of overflows in channels as the difference between the channel bottom and riverbanks increases.

The cGAN training processes were carried out using 200 epochs and a batch size of 128. A learning rate of 0.005 was utilized with the Adam optimizer (KIEFER, 1953). The parameters of both generators were saved for each epoch so they could be utilized for validation. We used 25- and 100-year (Fig. 10c and d) design storm simulations to determine the maximum depths in areas VA1 and VA2 in order to validate both generators. The distribution of rainfall for the design storms was then determined using the alternating blocks method.
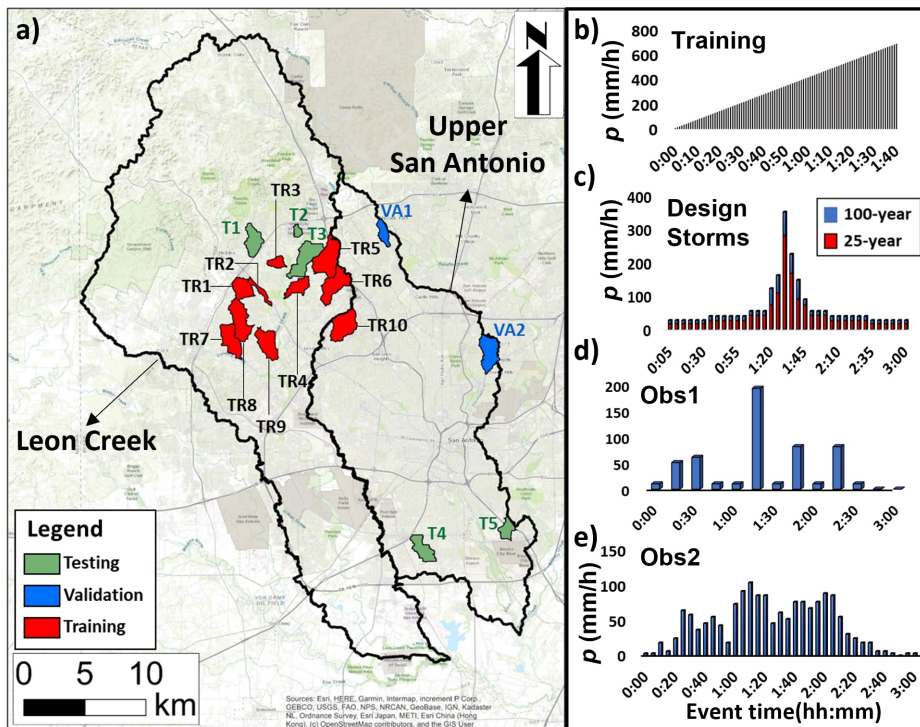
Figure 10 – Training, validation, and testing areas of cGAN-Flood. Source: (LAGO, 2022)

3.1.2 cGAN-Flood Testing and Performance

The testing areas in San Antonio were tested with both 25 and 100-year storms Fig. 10c and d (LAGO *et al.*, 2023). In addition, two observed events were also used for testing Fig 10e and f to evaluate different rainfall distributions in cGAN-Flood's performance. The performance metrics of in all testing areas, for the four rainfall events, are shown in Table 4. The model presented a satisfactory overall performance for all catchments and events, despite the differences in area, slopes, imperiousness, and total flood volume distributed. Therefore, cGAN-Flood was capable of generalizing to different topology and boundary conditions.

The maximum root squared mean error (RSME) was 0.18m, with a minimum of 0.69 of R^2. The hit rate (HR), false alarm rate (FAR), and critical success index (CSI) used

to evaluate the performance of the model to identify dry and wet cells, were calculated for all flood cells above 0.01m. This shallow depth was chosen to better evaluate the performance of generator 1, which accounted for every cell with a depth higher than zero. These metrics showed that, overall, cGAN-Flood can satisfactorily predict flood for shallow depths. The minimum CSI, which considers false alarms and missings, was 69%. In addition, $CSI_{0.05}$ and $CSI_{0.3}$, computed for every cell flooded with depths above 0.05 and 0.3m, were used to evaluate generator 2 capacity in predicting deeper water depths. Despite the decrease in performance moving towards deeper depth limits, due to the decrease in the analyzed flooded area, cGAN-Flood also presented a satisfactory performance.

Table 4 – Performance metrics of cGAN-Flood for all testing areas

Storm	Testing Area	v_t (1000m³)	RSME (m)	R^2	HR (%)	FAR (%)	CSI (%)	$CSI_{0.05}$ (%)	$CSI_{0.3}$ (%)
	TE1	285	0.09	0.90	94.4	14.8	81.1	72.7	69.0
	TE2	37	0.08	0.85	88.2	11.7	78.9	71.1	68.3
25-year	TE3	486	0.13	0.89	93.2	15.3	79.8	72.3	68.0
	TE4	223	0.09	0.88	94.1	10.9	84.4	74.2	67.1
	TE5	119	0.17	0.84	83.9	11.9	75.3	72.1	67.9
	TE1	339	0.10	0.90	94.6	13.3	82.6	74.6	70.9
	TE2	46	0.09	0.86	86.8	8.5	80.4	72.9	67.8
100-year	TE3	595	0.14	0.87	93.5	13.4	81.7	74.4	67.5
	TE4	270	0.10	0.86	94.2	9.4	85.8	76.3	65.7
	TE5	143	0.16	0.78	84.3	10.3	76.9	73.7	69.3
	TE1	242	0.09	0.88	94.5	17.5	78.8	70.7	65.4
	TE2	34	0.08	0.84	89.0	14.8	77.1	69.3	67.1
Obs1	TE3	443	0.13	0.84	93.8	18.3	77.5	69.7	67.4
	TE4	201	0.09	0.84	94.0	12.4	83.0	73.3	66.9
	TE5	104	0.18	0.77	91.5	15.2	78.6	69.7	64.7
	TE1	196	0.10	0.82	92.7	23.1	72.5	63.9	60.0
	TE2	28	0.09	0.78	89.9	21.9	71.8	64.5	60.9
Obs2	TE3	412	0.17	0.72	94.8	28.3	69.0	58.8	61.0
	TE4	179	0.11	0.74	95.3	19.9	77.0	65.5	67.2
	TE5	82	0.18	0.69	92.4	24.4	71.2	61.1	58.7

3.1.3 Objective

Given the necessity in evaluating the performance of cGAN-Flood in different domains the objective of this chapter is **to evaluate how cGAN-Flood performs in catchments with a distinct topological configuration from where it was trained**.

To evaluate its transferability, cGAN-Flood was applied to different catchments in Sao Paulo to evaluate the DL model's performance. In addition, cGAN-Flood was to predict high-resolution floods in Aricanduva Watershed with a low-resolution Hydropol2D was used for calculating the flood volume, a raster-based model, which requires a different methodology when using a mesh-based one (used in the previous chapter).

3.2 cGAN-Flood Testing in Sao Paulo Catchments

Despite cGAN-Floods capability in predicting floods for San Antonio watersheds, the catchment's regional characteristics are similar, and the data source used in all areas is the same. Therefore, there is a need to evaluate the models' generalization capacity in catchments located outside San Antonio's region. In this chapter, cGAN-Flood was tested for in Sao Paulo city.

3.2.1 Study Areas

The Aricanduva watershed is located in the city of Sao Paulo, Brazil, and has approximately 150 km² (Fig. 11). The watershed was modeled using HydroPol2D, a raster-based model. HydroPol2D is a diffusive-like cellular automata model that couples hydrologic, hydrodynamic, and water quality transport of pollutants. Please refer to (JR *et al.*, 2023) for a detailed model description. It also contains terrain analysis algorithms to treat DEM issues and allow proper hydrologic continuity, allowing terrain smoothening (SCHWANGHART; SCHERLER, 2017) and burning (PAIVA *et al.*, 2013).
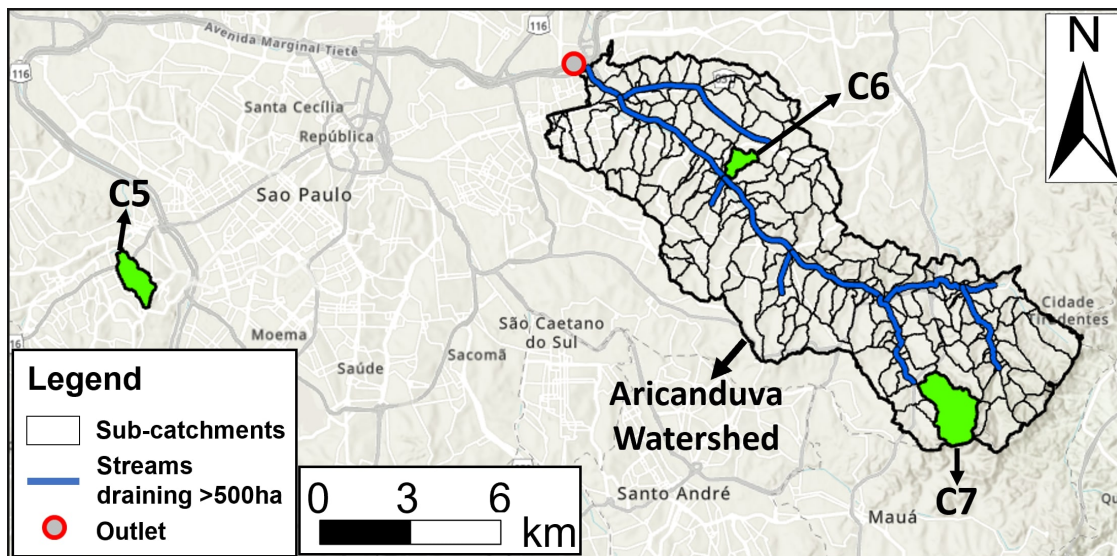
Figure 11 – Aricanduva Watershed and Testing Areas in Sao Paulo

We have used a 15m resolution for the HydroPol2D simulations. The DEM was resampled from a 1m resolution map, with bridges and culverts manually burned using HEC-RAS terrain modification. The channel modifications were calculated by measuring the channel's width close to the bridge or culvert. The permeable and impervious areas map was resampled from a 10m map (REPORT, 2019). The terrain and impervious map resampling operations were performed using the bilinear and nearest neighbor methods.

The flood volume v_t used for redistributing with cGAN-Flood was calculated directly from the maximum water depths maps. Unlikely HEC-RAS, which interpolates

Location	Area (ha)	Number of Cells (x10³)	Average cell slope (°)	Impervious Area (%)
C5	128	142.0	33	76.3
C6	63	70.4	28	91.5
C7	303	336.8	50	31.0

WSE between cell faces, the water depths calculated with Hydropol2D result directly from the water balance between cells. The flood volume at each cell can be calculated by multiplying the cells' area by the water depth. Therefore, v_t is the sum of flood volume in each cell inside a given area. The method of calculating v_t for raster-based models makes it more accessible than mesh-based ones, which can be performed directly from low-resolution flood maps and does not require one of the model's source files, such as HEC-RAS hdf plan file.

3.2.1.1 Performance Analysis in Sao Paulo Catchments

The performance of cGAN-Flood coupled with Hydropol2D was also done in smaller catchments instead of the whole Aricanduva Watershed. Hyrodpol2D models with a 15m resolution were created for catchments C5, C6 and C7, located across Sao Paulo city (Fig. 11). The low-resolution Hydropol2D models were used to calculate v_t to be redistributed. Therefore, this chapter demonstrate how to couple cGAN-Flood with a raster based model, whose methodology differ from the one presented in the previous chapter. These catchments were selected to represent different catchment sizes, imperviousness percentages, and average slopes, as presented in Table 3.2.1.1. HEC-RAS models with cell sizes of 3m were created as ground truth for comparing modeling results, as it is a hydrodynamic model with a better representation of flood dynamiics.

Considering these catchments are situated outside San Antonio, the location cGAN-Flood training catchments, we've also assessed the transferability of cGAN-Flood to these different regions. Consequently, we have compared the outputs from cGAN-Flood with the total flood volume (v_t) computed directly from the high-resolution HEC-RAS models. By doing this, we were able to eliminate the errors associated with Hydropol2D in calculating v_t from this analysis. As a result, we can gain a more precise understanding of the errors that are exclusively associated with the cGAN-Flood model.

Similarly to the investigations conducted in the previous chapter, the HEC-RAS simulations were conducted on the i7 10700 CPU operating at 2.9GHz CPU and cGAN-Flood on the 8 GB NVIDIA GeForce RTX 2060 SUPER GPU (1650 MHz). At the moment these analysis, Hydropol2D did not have GPU compatibility and its simulations were conducted on the CPU.

Table 5 – Performance Metrics for Catchments in Sao Paulo

Storm	Catchment	HR05	FAR05	CSI05	CSI	CSI3	RSME (m)	MAE (m)	NSE
	C5	76%	21%	63%	69%	50%	0.17	0.09	0.65
10-year	C6	83%	23%	67%	73%	49%	0.09	0.05	0.70
	C7	78%	28%	60%	61%	53%	0.19	0.11	0.70
	C5	77%	19%	66%	72%	54%	0.17	0.10	0.68
100-year	C6	84%	21%	69%	75%	54%	0.09	0.06	0.72
	C7	77%	25%	61%	62%	58%	0.21	0.12	0.71

3.3 Results

The effectiveness of cGAN-Flood in Sao Paulo Catchments was evaluated by comparing its outputs with HEC-RAS map. To exclude uncertainties related to predicting the flood volume, the flood volume distributed with cGAN-Flood matches exactly the volume in HEC-RAS maps for this analysis. As the catchment characteristics of the C5, C6, and C7 catchments are significantly different from the training ones, cGAN-Flood showed worse performance than testing catchments in San Antonio. For instance, the average RSME and MAE were 0.15m and 0.09m for C5, C6, and C7, while the maximum values for the catchments at UPSA were 0.09 and 0.019m. The maximum NSE in Sao Paulo was 0.72, below the average of 0.75 for UPSA catchments.

HR, FAR, and CSI also show larger errors regarding flooded cell locations in Sao Paulo than in San Antonio, as Table 5 show. cGAN-Flood showed better accuracy when considering shallow depths, similar to UPSA catchments, with higher CSI01 values than CSI05 and CSI03. CSI03 presented the lowest values, with an average of 53%. Higher CSI values considering shallower depths were also observed in Lowe. For instance, Their CSI0.05 ranged from 44.7 to 58.3% (average of 48.7%), and their CSI0.3 ranged from 23.5 to 59.2% (average of 37.4%).

The different spatial inputs between San Antonio and Sao Paulo catchments explain the drop in performance. First, Sao Paulo city is more hilly, with the average cell slope of the terrain in the selected areas varying from 28 to 50°. As a comparison, the catchments with the highest average cell slope used during the training phase was 21°, including the 20% increase with the terrain modification (LAGO *et al.*, 2023). Furthermore, Sao Paulo tends to have fewer green spaces when compared to San Antonio. For instance, C5 and C6 present an imperviousness percentage higher than all testing, validating, and training catchments in San Antonio, which ranged from 29.9 to 63.8% (LAGO *et al.*, 2023). C7 is located in a suburban area with only 31% impervious area. In addition, the spatial patterns of the input data in Sao Paulo also differ from what cGAN-Flood has seen during training. Fig 12 illustrates the spatial inputs in San Antonio and Sao Paulo catchments,

represented by C1 and C5, respectively. The first major difference is the impervious data. In San Antonio, the high resolution allows for delineating roads and buildings. In Sao Paulo, however, an impervious map with only a 10m resolution is available, with the impervious areas represented as continuous blocks. It can also be seen that the terrain model in San Antonio is smoother than the one in Sao Paulo, which presents more abrupt changes in elevation due to terrain excavations to accommodate housing. These differences in terrain also affect the slope matrices with patterns that were unseen during training. Moreover, our analysis did not take into account the differences in infrastructure (e.g. bridges, culverts, and underground pipes) between San Antonio and Sao Paulo. These differences in infrastructure between the two cities could potentially further decrease the model's accuracy. Recognizing and incorporating such intricate infrastructural elements is necessary to improve model generalization, especially when ANNs are trained considering hydraulic infrastructure elements.
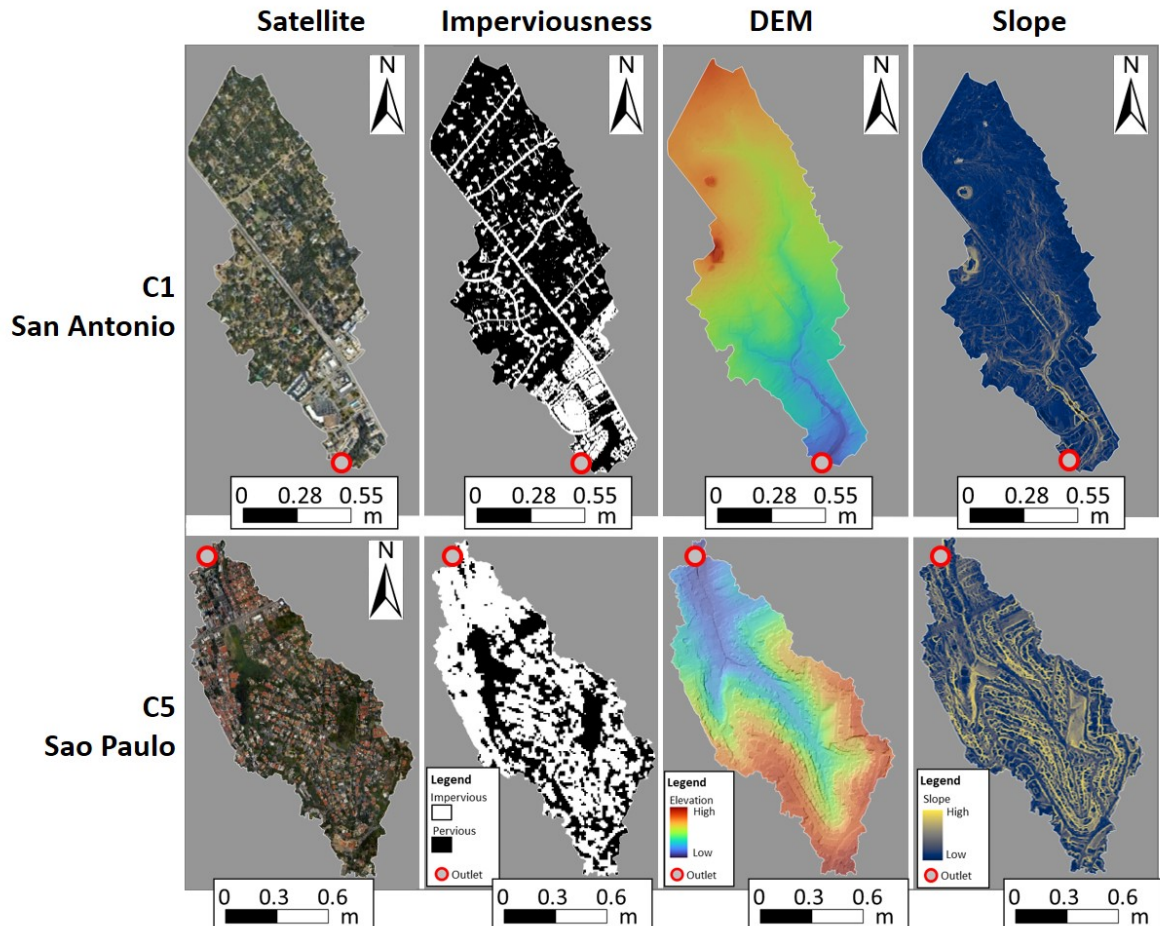
Figure 12 – Illustration of the difference in spatial characteristics between San Antonio and Sao Paulo

Despite the drop in performance, cGAN-Flood could still generate flood maps for Sao Paulo Catchments that are similar to the ones generated with high-resolution HEC-

RAS. Fig. 13 exemplifies food predictions for C6 and C7 catchments for depths larger than 0.01m and 0.3m. In catchments C6, the cGAN-Flood map was similar to the HEC-RAS output, with sparse miss and false alarm cells across the catchments. cGAN-Flood tends to overestimate the number of cells equal to or larger than 0.3m, especially along the main channel. The reason might be the higher slope of the catchment when compared to the training ones, and cGAN-Flood underestimated the channel's flow capacity. Nonetheless, cGAN-Flood could still identify the main flood locations in C7.
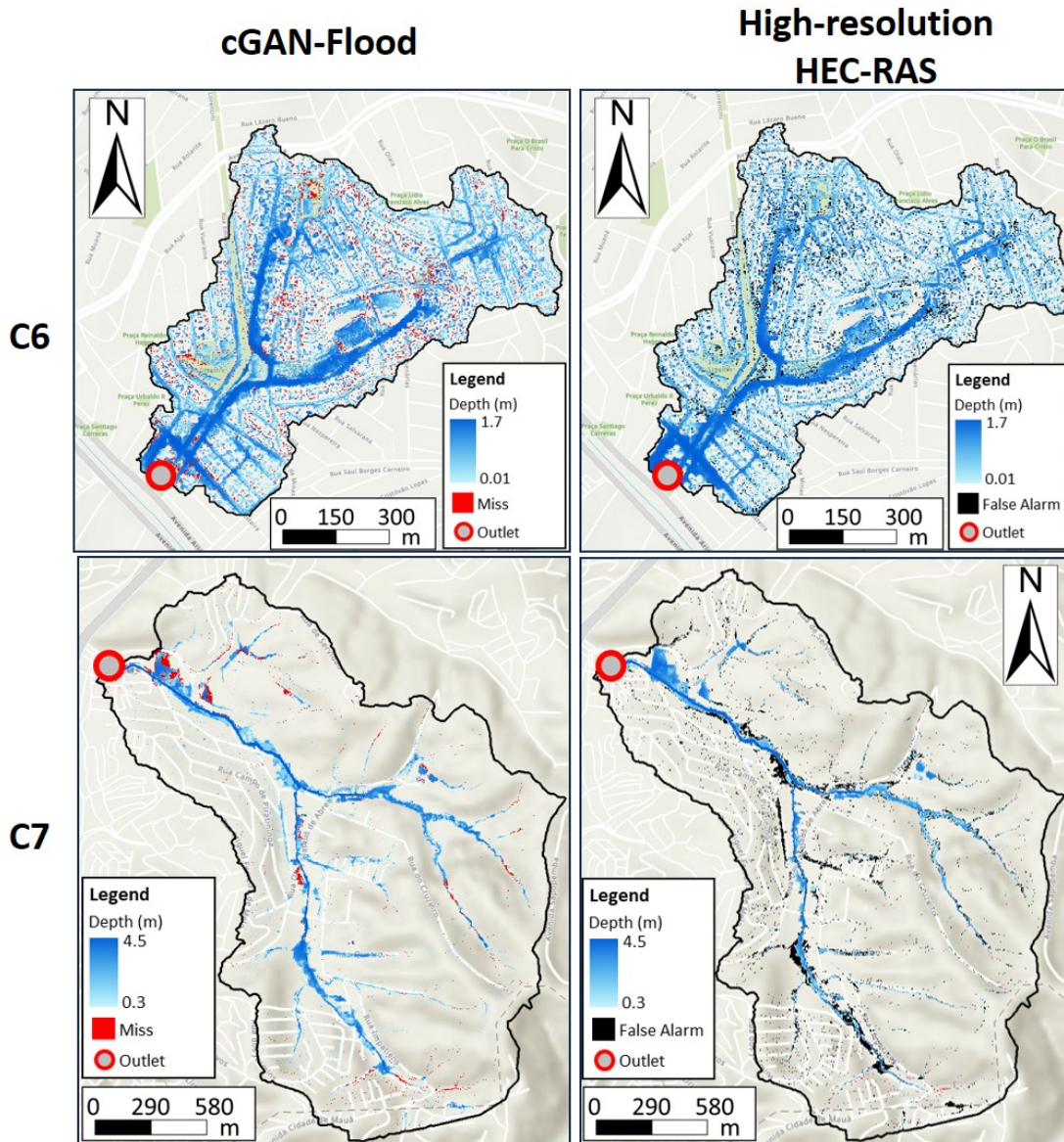
Figure 13 – Flood maps comparing high-resolution HEC-RAS and cGAN-Flood in Sao Paulo catchments.

When coupling HYdropol2D with cGAN-Flood, the errors in flood volume prediction are presented in Table 6. The error in v_t calculated with the low-resolution Hydropol2D varied from -9.8% to 21.6%. Catchments C5 and C6 presented errors comparable to those related to the ones calculated with low-resolution HEC-RAS, ranging from -6.2 to -9.8%.

Table 6 – Comparison of total flood volume calculated from low-resolution Hydropol2D and high-resolution HEC-RAS models

Storm	Catchment	Volume high-resolution HEC-RAS (1000m3)	Volume low-resolution Hydropol2D (1000m3)	Error
10-year	C5	102.1	94.6	-7.3%
	C6	33.0	29.9	-9.3%
	C7	196.4	224	14.1%
100-year	C5	124.6	116.9	-6.2%
	C6	40.4	36.4	-9.8%
	C7	246.2	299.4	21.6%

Volumes calculated for C7 were significantly higher, possibly due to high catchment slopes. As a rapid flood model, Hydropol2D does not consider inertia, which is relevant for accurate predictions in areas with high velocities (JAMALI *et al.*, 2018).

The performance of cGAN-Flood, when integrated with Hydropol2D, is detailed in Table 7. Generally, a decrease in the performance of cGAN-Flood is observed when it is coupled with Hydropol2D, primarily due to errors in the calculation of v_t. For example, the FAR05 in Catchment C7 was observed to be 31 and 30%, attributed to an overestimation in flood volume as opposed to 28 and 25% when the volumes are well-matched (refer to Table 5). However, when we average the metrics for the three catchments across both the 10 and 100-year storm events, the degradation in performance is not substantial. Specifically, the averages for CSI05 and NSE declined slightly from 64 to 63% and 0.69 to 0.68, respectively, while the average RMSE increased marginally from 0.15 to 0.16. This analysis indicates that errors tied to the performance of the DL model in redistributing the flood volume are more significant than uncertainties in the calculation of flood volume. This underscores the necessity to expand the training of the cGAN-Flood model to enable it to recognize a wider array of spatial patterns, thereby enhancing its generalization capabilities. A sensitivity analysis is recommended to evaluate how adding extra catchment variability during training improves the metrics when cGAN-Flood is applied to testing areas.

In spite of the errors linked to cGAN-Flood and flood volume prediction, the integration of the DL model with the low-resolution Hydropol2D model substantially enhanced the precision of flood predictions when compared to Hydropol2D alone. For example, Hydropol2D significantly underestimates flooded cells with a depth greater than 0.05m, with HR05 values ranging between 28 and 49%. However, upon coupling with cGAN-Flood, HR05 values increased to fall within the range of 73 to 82%. The incorporation of cGAN-Flood resulted in an average decrease in FAR05 and RMSE by 10.5% and 0.015m, respectively, and an average increase in CSI01 and NSE by 27% and 0.25, respectively. The MAE presented an average increase of 0.02m. The advancement in

Table 7 – Performance metrics of low-resolution Hydropol2D and cGAN-Flood

	Storm	Catchment	FAR05	HR05	CSI05	CSI	CSI3	RSME (m)	MAE (m)	NSE
Low Resolution Hydropol2D and cGAN-Flood	10-year	C5	19%	73%	63%	69%	52%	0.09	0.17	0.66
		C6	20%	80%	67%	73%	48%	0.05	0.09	0.70
		C7	31%	80%	59%	61%	50%	0.12	0.19	0.67
	100-year	C5	17%	76%	65%	71%	55%	0.10	0.18	0.68
		C6	18%	82%	69%	75%	54%	0.06	0.10	0.72
		C7	30%	80%	60%	61%	52%	0.14	0.23	0.66
Low Resolution Hydropol2D	10-year	C5	36%	28%	24%	41%	32%	0.13	0.16	0.36
		C6	30%	39%	33%	43%	41%	0.07	0.06	0.51
		C7	36%	44%	35%	35%	38%	0.13	0.17	0.40
	100-year	C5	34%	33%	28%	45%	36%	0.13	0.17	0.40
		C6	29%	42%	36%	47%	46%	0.07	0.07	0.54
		C7	33%	49%	40%	35%	47%	0.12	0.19	0.45

flood mapping resolution is depicted in Fig. 14. Despite a significant error of 21% in volume prediction for Catchment C7, the flood maps generated with the help of cGAN-Flood are noticeably more accurate compared to those produced by the low-resolution Hydropol2D. Notably, the low-resolution simulation from Hydropol2D failed to capture essential flood features such as roads, a shortcoming attributable to the resampling of the terrain. These findings also suggest that the flooded area (with depths greater than 0.01m) is generally greatly overestimated. This pattern may explain why MAE is lower with the low-resolution Hydropol2D. Shallow depths overestimated by Hydropol2D are registered as zero with HEC-RAS outputs. At these locations, the discrepancy between cell depths is relatively minimal, resulting in a reduction of the MAE.

3.3.0.1 High-Resolution Prediction of Aricanduva Watershed

The improvements in flood mapping resolution of Hydropol2D maps with cGAN-Flood for Aricanduva Watershed are exemplified in 15. Unlikely the flood maps generated with the low-resolution mesh-based model, which failed to generate pluvial flooding (15), the low-resolution Hydropol2D could somewhat represent flood patterns with the coarse pixel size. However, as discussed in the previous section, resampling the terrain may misrepresent important urban features, such as roads, leading to overestimating shallow depths. Redistributing the flooded volume with cGAN-Flood to a higher resolution results in a more realistic prediction of flooded depth and area.

Regarding time efficiency, the low-resolution Hydropol2D model, comprising 460k pixels with 15m resolution, demanded 75 minutes, while the cGAN-Flood volume redistribution across the entire Aricandura watershed took an additional 18 minutes. Consequently, the total computation time to create high-resolution flood maps encompassing roughly 11.5 million cells was 83 minutes. Considering the same assumption of computational efficiency discussed in Section 2.3.2, a high-resolution HEC-RAS model with a 3m cell size
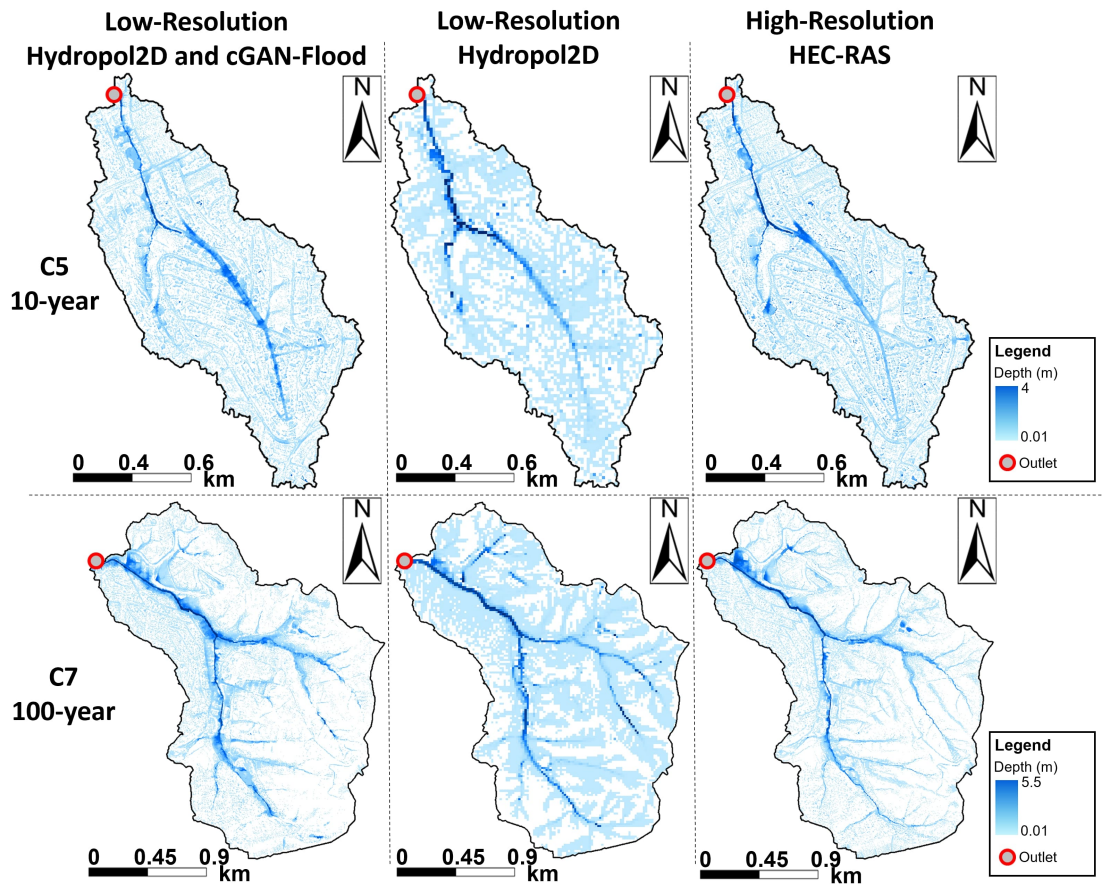
Figure 14 – Flood maps generated with cGAN-FLood and low-resolution Hydropol2D compared with high-resolution HEC-RAS in C5 and C7 catchments

would take approximately 2 days of simulation for the Aricanduva watershed. This analysis highlights the potential of increasing the resolution of coarse flood maps derived from a raster-based model. It is worth noting the drop in efficiency when coupling cGAN-Flood with Hydropol2D when compared to low resolution HEC-RAS, which presented a similar computational time for a larger area.

3.4 Conclusions and Recommendations

cGAN-Flood model was originally trained and tested for catchments in San Antonio, Texas. In this chapter, its generalization capacity to adverse topology was tested for catchments in Sao Paulo, which presented different data characteristics, especially with higher slopes. This chapter also presents a methodology on how to coupled a raster-based model with cGAN-Flood for increasing pixel resolution of flood maps.

The analysis showed a drop in cGAN-Flood's performance for Sao Paulo catchments compared to the testing ones in San Antonio. However, cGAN-Flood could still predict the flooded areas with results comparable to HEC-RAS, showing that major catchment characteristics in San Antonio could somewhat be captured and reproduced in Sao Paulo.
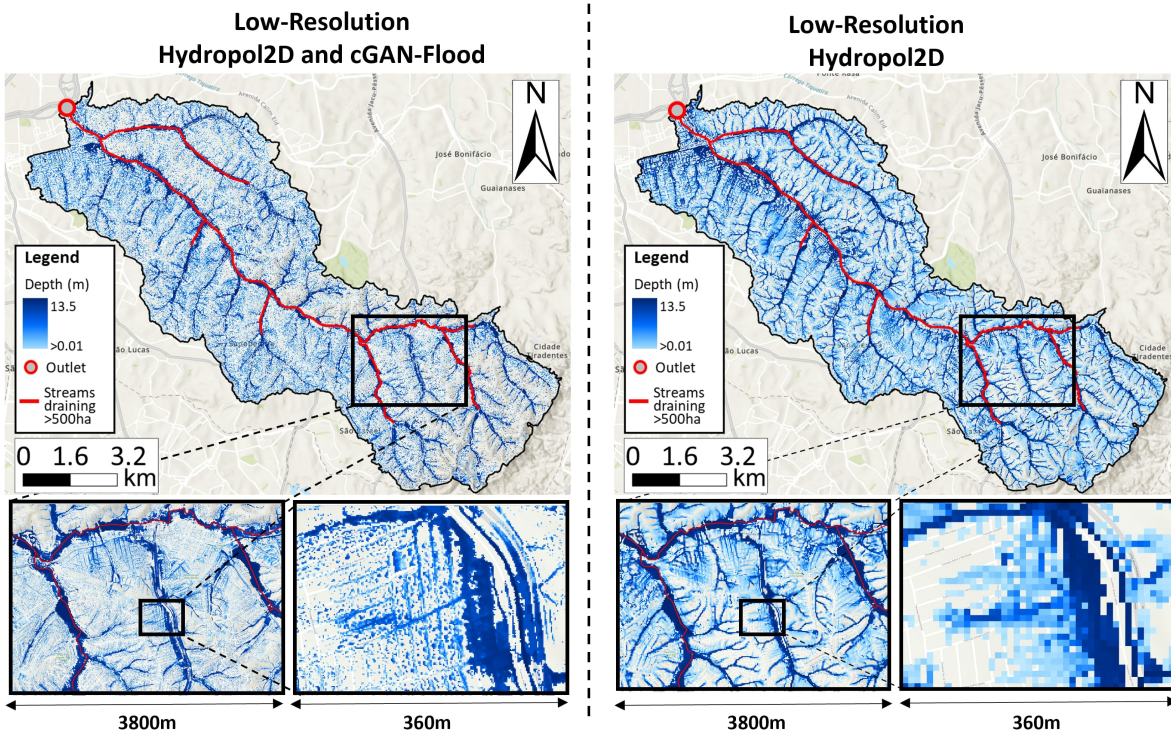
Figure 15 – Flood maps of the entire Aricanduva watershed with a low-resolution Hydropol2D model and after coupling it with cGAN-Flood.

This is an advantage that allows training a DL model where data and reliable hydrodynamic models exist to be later applied in areas where they lack. To achieve that goal, it is recommended to train cGAN-Flood with a higher diversity of topological patterns so that the model can maintain its accuracy when applied to different catchments.

This study shows that DL models can contribute significantly to rapid flood predictions study. In addition to large-scale modeling, DL models can support real-time predictions and optimization problems. However, DL models still need to be improved to increase generalization capacity so they can be applied to different locations without re-training, which is a time-consuming and data demanding process. Giving that the training in San Antonio catchments could somewhat generate satisfactorily predictions in Sao Paulo, we can infer that cGAN-Flood has a high generalization capacity with the potential for great performance in a wide range of topological patterns if catchment variability is inceased during training.

4 RIVERINE FLOOD MAPPING USING AN ARTIFICIAL NEURAL NETWORK RAPID FLOOD MODELING

ABSTRACT

Riverine flood mapping is often conducted using complex and data-intense hydrodynamic models, which hamper their application in many locations where data or funding is lacking. The literature shows that Artificial Neural Networks (ANN) have been applied for flood prediction and can be an alternative to the hydrodynamic models. However, the predictive ability of ANNs to simulate floodplains in different areas outside the training dataset needs to be better understood. This study developed a novel modeling approach using ANN to predict floodplains. ANN modeling capacity is highly dependent of the size of the training dataset. To improve model performance, we apply data augmentation by dividing the spatial domain in smaller spatial windows, called target domains. The methodology uses localized physical characteristics to increase the number of training samples and the generalization capabilities of the model. HEC-RAS-1D models were used to generate datasets taken as ground truth for training purposes. HEC-RAS models were built for sixteen different locations in San Antonio, Texas: Ten locations were used for training, three for validating, and three for testing the model. Flood predictions presented satisfactory results compared to HEC-RAS models for the validation and testing areas, suggesting that this approach can create ANN models capable of generating predictions in different areas outside of the training and validation datasets. The ANN approach outperformed more simplistic methods, such as using normal depths for all locations. In addition, simulation for UPSA was performed with ANN and compared to FEMA. The floodplains agree reasonably, but the is inclusion of hydraulic structures during the ANN training is recommended to improve the predictions. A major advantage of the ANN model is speed and it requires simpler model inputs. The ANN rapid flood model was 20 times faster than HEC-RAS models, and can be run simply with the DEM and inflows. This approach can be used as Rapid Flood Models to improve the real-time prediction of floods and speed up optimization problems.

4.1 Introduction

Estimates indicate that flood events caused over $1 trillion in economic damages and victimized more than 220,000 people from 1980 to 2013 (WINSEMIUS *et al.*, 2016). Furthermore, climate change projections show that the frequency and intensity of extreme storm events tend to increase in the future (AICH *et al.*, 2016; CLAVET-GAUMONT *et al.*, 2017; GAO *et al.*, 2020; SHRESTHA; LOHPAISANKRIT, 2017; YIN *et al.*, 2018), which can magnify the impacts of flooding. The development of flood mitigation planning is a essential for protecting comminities and local economies. The effectiveness of such

plans depends on accurate and reliable floodplain mapping, typically done with the aid of hydrodynamic simulation models. Building reliable hydrodynamic models can be time-consuming and costly (FEMA, 2013; NRC, 2007), because it requires high-resolution data for building and validating the models (NEAL *et al.*, 2009; ZHANG; PAN, 2014).

It is estimated that the average cost per mile of reach mapped ranges from $5,000 to $10,000 (WOZNICKI *et al.*, 2019). High cost is likely a major contributor for low-coverage floodplain mapping worldwide. In the U.S., for instance, 40% of the reaches have not yet been modeled and mapped (WOZNICKI *et al.*, 2019). Moreover, many floodplain maps are outdated and don't reflect the current and future flood risks associated with land use and climate change.

Recent studies have applied Artificial Neural Networks (ANN), which are computing systems inspired by biological neural networks, for flood estimation. ANN can learn and apply complex rules to simulate very complex phenomena, including hydraulics of flood events. ANN is also computationally efficient algorithms and can make complex predictions for very large domains in a fraction of the computational budget required by hydrodynamic models. For instance, PETERS; SCHMITZ; CULLMANN (2006) used HEC-RAS 1D model to train a simple one-hidden layer ANN, for flood routing in Germany. Their model replicated the hydrodynamic model's results in less than 1s for a 1-year time series, which takes around 12 hours using the original hydrodynamic model. SHRESTHA; THEOBALD; NESTMANN (2005) applied ANN for flow routing, and their results show that the ANN could extrapolate the predictions for flood events with different flow magnitudes from the one used for the training model. (PANAHI *et al.*, 2021) implemented Convolutional Neural Networks (CNN) and Recurrent Neural Networks (RNN) to generate flash flood probability maps in Iran and observed significant accuracy in predictions that could be beneficial for planning flood mitigation strategies (PANAHI *et al.*, 2021). On the other hand, (BOMERS *et al.*, 2019) combined a 1D/2D hydrodynamic model with an Artificial Neural Network (ANN) to recreate historical flood events in the Netherlands. This approach remarkably improved the accuracy of reproducing local flood characteristics, and it reduced the uncertainties tied to these historical events.

As a data-driven modeling approach, one of the drawbacks of ANN is the requirements of large datasets for training and validation (TAYLOR; NITSCHKE, 2018; CARVALHO; FILHO; PORTO, 2021; ANTHONY; BARTLETT; BARTLETT, 1999; LEE; DERRIBLE, 2020; IYER; RHINEHART, 1999). Although flooding is the most common and fatal natural disaster worldwide (DOOCY *et al.*, 2013; JONKMAN, 2005), few locations contain high-resolution spatial and temporal datasets of real flood events. This lack of observations impairs the ability of ANN to make accurate predictions because of weak model training and validation. An alternative to the lack of datasets is to generate synthetic datasets using physically based models, such as hydrodynamic simulators and

data augmentation methods.

4.1.1 Chapter Goals and Contributions

The main goal of this chapter is to develop an ANN model for rapid floodplain mapping in data-scarce and large watersheds. The literature presents several studies that apply ANN for flood estimation with satisfactory performance (BERKHAHN; FUCHS; NEUWEILER, 2019; BOMERS *et al.*, 2019; DTISSIBE *et al.*, 2020; FANG *et al.*, 2021; **??**; LE *et al.*, 2019; PANAHI *et al.*, 2021; PETERS; SCHMITZ; CULLMANN, 2006; SHRESTHA; THEOBALD; NESTMANN, 2005; SONG *et al.*, 2020; ZHAO *et al.*, 2020). All previous investigations, however, have assessed model performance for the same location for which the ANN was trained. Here we address the question of whether ANN models could be trained using data from some locations and predict flooding in other areas or river branches in the same watershed. To achieve the main goal, this chapter contains the following contributions:

- Two innovative ANN structures, integrating both dense and convolutional layers, are introduced for predicting riverine flooding. This addresses the domain of pluvial flooding, an area not covered by cGAN-Flood.

- A method for generating synthetic high-resolution floodplain datasets is described. The method is based on 1D hydrodynamic model simulations to perform data augmentation by altering the floodplain digital elevation model (DEM), slopes, and cross-sections.

- The chapter tested the predictive ability of the ANN models to generate accurate flood maps in areas outside of the training regions.

- The ANN models were evaluated for the entire Upper San Antonio Watershed.

The chapter is organized into six main sections. In Section 4.2, we describe the ANN model, its data inputs and pre-processing, the methods for data augmentation, the two architectures, the training and hyperparameters, and the algorithm used to create flood maps. Next, Section 4.3 depicts the case-study used for testing the proposed modeling approach. This section also describes how the new method was used to generate floodplains for a large domain and how they were compared to the existing floodplain map generated by the Federal Emergency Management Agency (FEMA). Section 4.5 presents the ANN training and mapping performance metrics. Finally, we summarized the paper and discussed the main findings and limitations, offering recommendations for future research directions regarding fluvial flood predictions with DL models in Section 4.6. The mathematical notation is: italicized lowercase characters represent variables or parameters (e.g. k is kernel size, $d(t)$ is water depth function of time). Italicized, boldface

upper and lower case characters represent matrices and column vectors, respectively (a is a vector and A is a matrix). The proposed ANN approach is described in five subsections: Data Inputs and Pre-Processing, Data Augmentation, ANN Architectures, ANN Training, and Hyperparameters, and Algorithm for Flood Predictions.

4.2 ANN Model Applied for Water Depth Predictions

4.2.1 Data Inputs and Pre-Processing

This section explains the data inputs and pre-processing treatment of the data for the ANN flood mapping model. Given a large domain of a river channel, the goal of the ANN model is to predict a vector output of water depths (d) in target locations (red dot on Fig. 16) based on five inputs: a matrix containing elevation (E) obtained from a Digital Elevation Model (DEM), slope profile vector (s), cross-section vector (x), inflow hydrograph vector (q), and downstream water depths over time (d_t). The maximum depths are then selected from vector output to generate fluvial flood mapping. Previous model versions included a raster map with pervious and impervious areas; however, these inputs did not improve performance and were removed from the model to simplify operations. Infiltration is previously accounted with a hydrological model, reflecting on the hydrograph input of the model.
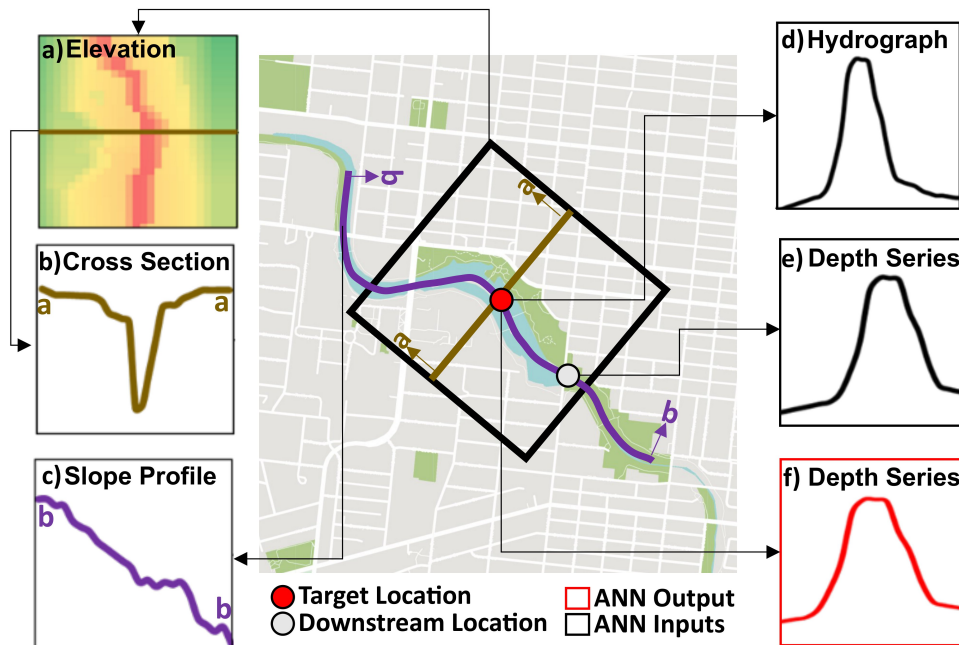
Figure 16 – Input data of the ANN: (a) elevation, (b) cross-section, (c) slope profile, (d) hydrograph, and (e) downstream water depths. The output of the ANN is depth time series (f) at the target location.

The input E is a 2D matrix with the target location in the center (Fig. 35a). The algorithm rotates the DEM so that the river follows a north-south direction. The rotation

angle is determined according to the angle of the drainage line at the target location. Cross-sections x and slope profile s can be extracted automatically from the E, or included externally (e.g. from topographic survey). The pre-processing algorithm extracts the cross section with the target location point at the center of the E in a vector (Fig. 35b). The elevations along the drainage line are also collected as a vector to represent the slope profile as s (Fig. 35c). Given a squared matrix $A_{n \times n}$ with elevation values (a) collected from the DEM raster, E was normalized with Eq (4.1).

[h]

$$e^{i,j} = \frac{a^{i,j} - a^{\frac{n}{2},\frac{n}{2}}}{\Delta a}, \forall i,j = [1,\ldots,n], (a^{i,j})_{n \times n} = A \tag{4.1a}$$

$$E = \begin{bmatrix} [h]e^{1,1} & e^{1,2} & \ldots & e^{1,n} \\ e^{2,1} & e^{2,2} & \ldots & e^{2,n} \\ \vdots & \vdots & \ddots & \vdots \\ e^{n,1} & e^{n,2} & \ldots & e^{n,n} \end{bmatrix} \tag{4.1b}$$

where $e^{i,j}$ is the normalized elevation value. The whole matrix is subtracted by the central elevation $a^{\frac{n}{2},\frac{n}{2}}$ so that the target location elevation is equal to zero. Δa is a pre-determined difference in elevation taken from E so all e values are below one. The treated x is the middle row of matrix E (Fig. 35-a to Fig. 35-b) described by Eq (4.2):

[h]

$$x = E_{\frac{n}{2}*} = [e^{\frac{n}{2},1}, e^{\frac{n}{2},2}, \ldots, e^{\frac{n}{2},n}]^T \tag{4.2}$$

Depth vector at the target location was normalized according to Eq (4.3):

[h]

$$d^t = \frac{wse^t - a^{\frac{n}{2},\frac{n}{2}}}{\Delta a}, \forall t = [1,\ldots,m] \tag{4.3a}$$

$$d = [d^1, d^2, \ldots d^m]^T \tag{4.3b}$$

where d^t is the treated depth value and wse^t is the water surface elevation at time t on the target location for a time series with duration m. The data treatment of vector d_d follows the same principle as vector d , but with wse collected downstream. Finally, the slope profile s was treated with Eq. (4.4):

[h]

$$s^i = \frac{a^i - a^q}{d_i^q}100, \forall i = [1,\ldots,q], (a^i)_q = a \tag{4.4a}$$

$$s = [s^1, s^2, \ldots s^q]^T \tag{4.4b}$$

where s^i and a^i are slope and elevation values for element i in the s vector, q represents the last entry in in the s vector , a is a vector with elevation along the drainage line, and d_i^q represents the euclidean distance between cell i and cell q. For training the ANN, the water depth series and the q inputs were collected from hydrodynamic modeling results (details in Section 4.3).

4.2.2 Data Augmentation

Data augmentation consists in modifying the data to increase the number of training and validation samples. Previous studies have shown that data augmentation can improve the accuracy of the ANN and enhance the generalization capability of the model (ZHANG *et al.*, 2021; ROY *et al.*, 2019). In our approach, two techniques were used. First, for each sample in the dataset, the x and E inputs were mirrored laterally for the same q, d, d_d and s. This technique doubled the number of training and validation samples. Second, we performed terrain modifications, by multiplying the original DEM raster by 0.8 to 1.2, with 0.05 increments between each alteration. Examples of how terrain modification affects the slope profile and cross-section are shown in Fig. 17-a and b, respectively. These modifications added eight hypothetical flood locations to be simulated with the hydrodynamic model. The 0.8 E represents a more prone flood area, with a mild slope profile, a shallower channel depth, and a plainer area at the overbanks. At the current version of the DL model, surface roughness is not considered. Modifying the HEC-RAS models with different Manning's n is a future recommendation if such input is included in the DL model. It is also a common practice to rotate the input images for data augmentation when training an ANN, such as what was done with cGAN-Flood (LAGO *et al.*, 2023). However, for this study, the E images were treated so that the upstream portion of the domain is maintained north. Fixating an origin helps the training process and facilitates the ANN to recognize patterns. In face recognition, for instance, the nose tends to be centralized in the center of the image GondhiFace2017.

4.2.3 ANN Architectures

Previous literature suggests that ensemble models can lead to better generalization potential than single an ANN (BROWN *et al.*, 2005; ALOBAIDI; CHEBANA; MEGUID, 2018; MORINI; PINELLI, 2021). Two ANN architectures that combine dense and convolutional layers are proposed to estimate water depths (Fig. 18). Both architectures apply 2D convolutional layers (Conv2D) in E and 1D convolutional layers (Conv1D) in the vectors s and x, followed by dense layers that process the remaining inputs vectors. Max pooling was applied between Conv2D layers to downsample their outputs. The difference between Architecture 1 and 2, is that the latter, uses a causal convolution layer with a dilation rate (DR) of 3 to process the vectors q and d_d before the concatenation. In
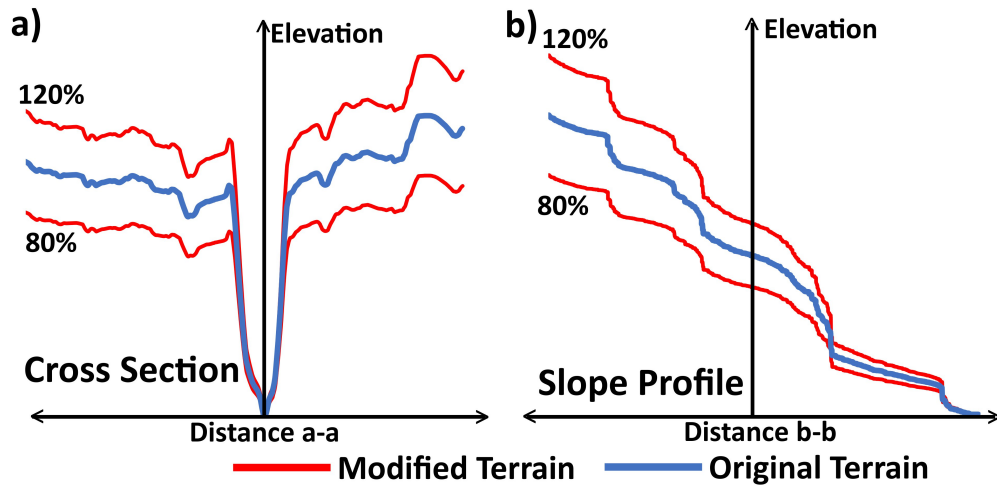
Figure 17 – Example of data augmentation for cross-section(a) and slope profile (b).

addition, Architecture 1 includes one additional Conv1D layer for s and x inputs, and one extra dense layer between the concatenation of q and d_d and the output d. These two architectures presented performance when evaluating the loss function during training.

Four different configurations were used in both architectures, with a different number of filters (f) and kernel sizes (k) on the convolutional layers and nodes (D) on dense layers, resulting in eight different topologies to generate the ensemble predictions. The final water depth values were computed as the average output of each of the eight ANN outputs. The selection of nodes (D) in the surrounding dense layers was set to ensure that the nodes in middle dense layers ($D*$) are less than twice the size of the input layer (XU; CHEN, 2008) and as being 2/3 of the sum of input and output layers (SHEELA; DEEPA, 2013). The Rectified Linear Unit (ReLU) activation function was used, which has been successfully applied to ANNs using convolutional layers (GODIN *et al.*, 2018; SHANG *et al.*, 2016). BERKHAHN; FUCHS; NEUWEILER (2019) evaluated the ANN ensemble approach to improve the accuracy of urban flood predictions. The authors applied ANNs as a single topology but trained with different initial weights. Even using ANN with the same topology, ensemble predictions decreased the error of predicted floodplains and showed to be beneficial. Tensorflow v2.1.0 (ABADI *et al.*, 2015) was used to create the ANN.
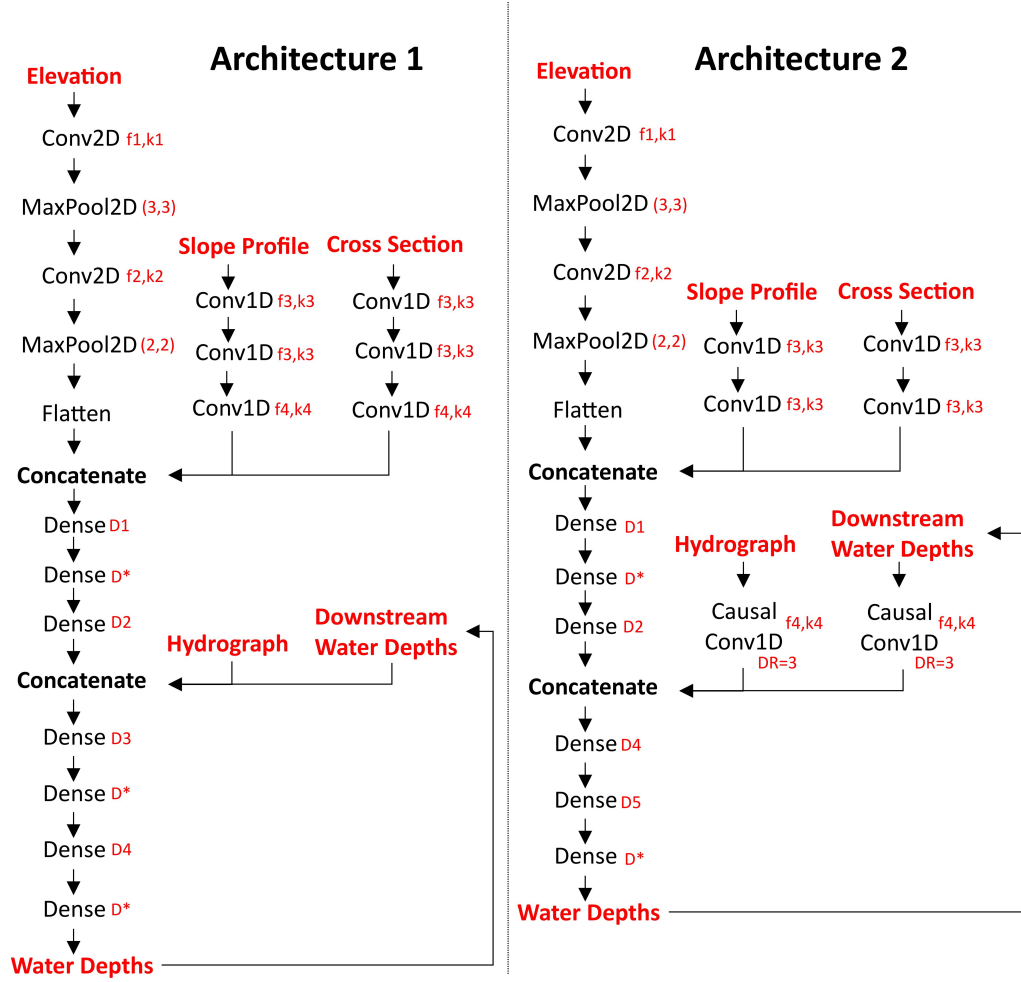
Figure 18 – ANN architecture 1 and 2 used for the ensemble predictions.

4.2.4 ANN Training and Hyperparameters

A custom loss function was used to train the model (Eq. (4.5)), which is a weighted average between the mean absolute error (MAE) between depth series and peak depths error:

$$Loss = \frac{1}{w_1 + w_2} \left[w_1 \left(\frac{|d_H - d|}{m} \right) + w_2 |max(d_H) - max(d)| \right], \tag{4.5}$$

where d_H is the vector with true depths simulated with the hydrodynamic model, d are the predicted depths with the ANN, and m is the number of time steps of the depth vector. w_1 and w_2 are the weights relative to MAE and peak depth error. We used $w_1 = 1$ and $w_2 = 2$ to force a higher accuracy at peak depths, which is more relevant for floodplain mapping.

Different batch sizes (1024 to 8192), learning rates (0.00001 to 0.001), and dropout rates (0 to 0.1) were tested to identify the best hyperparameters configuration. Batch sizes lower than 1024 showed significantly lower performance, while batch sizes larger than 8192 caused memory allocation issues. Very small learning rates quickly stagnated the validation loss at high values, while the learning process presented more unstable loss

values for larger learning rates. Random initial weights were set at the beginning of the ANN training. A batch size of 4046 and a learning rate of 0.0005 were used, as the previous analysis showed that these values generated the lowest minimum validation loss. Although dropout is also applied in increasing generalization, (DAI; LE, 2015) it did not contribute to reducing the minimum validation loss and was not applied in this study. The Nesterov Accelerated Adaptive Moment Estimation (Nadam) (DOZAT, 2016) was used for training, because it presented the best training performance when compared to the other optimizers available in Tensorflow.

The sizes of the E, x, and s inputs and the most suitable topologies were determined through trial and error, which is a common practice (JAAFRA *et al.*, 2019) in ANN studies. The best configuration was selected for the minimum validation loss during the training process. Furthermore, we evaluated which of the inputs better helped to decrease the validation loss function. Nonetheless, additional research is needed to determine if these architectures remain optimal when applied to different catchments. For the local information (E, s, and x), the validation loss was evaluated by training the ANN without these components. Then, the minimum validation loss was compared to the complete ANN. The downstream depth was modified from 5% to 200% of its original values at the outlet of each validation and testing area. Then, the error at each point upstream was calculated by the difference between the ANN prediction with the original downstream condition.

4.2.5 Algorithm for WSE Predictions

The eight trained ANN architectures were coupled to an algorithm for predicting flood maps for the entire domain. The pseudo-code of the algorithm is presented as follows.

First, a drainage pathway raster map is generated, in which each cell in the drainage line has a unique identification number that increases from the upstream to downstream areas. This map guides the algorithm to move throughout the domain. In addition, this map is used to indicate where an inflow is introduced in the model. If the raster map already exists, this pre-processing step is skipped. In step 1, the first depth series is predicted at the outlet with Manning's equation assuming normal depth. The energy slope at the outlet should be pre-defined. Then, in step 2, the ANNs and their optimized weights are loaded for predicting water depths. A new target location is then identified, where the ANN will predict the water depth series (step 3). In this step, all required input data is automatically acquired and treated and a new depth series is generated using the ANN. Step 3 repeats until the water depth series is determined for the whole spatial domain. Then, new cross-sections are drawn perpendicular to the flow direction, where WSE is calculated and interpolated linearly.

Euclidean distances of each cell to the drainage line are computed to create the

cross-sections, which followed the greatest gradient of the distance map. These cross-sections differ from the ones used as inputs to the ANN (Fig. 35), which are simply collected from the E matrix to speed up the simulation. As the input cross-sections to the ANN are straight lines, they can overlap while creating the WSE. Finally, the interpolated WSE map is subtracted by the DEM to generate the flood depths.

Algorithm 1: Algorithm for generating floodplain using the ANN architectures.

Target location starts at the outlet. Downstream boundary condition is calculated assuming normal depths
All trained ANN are initialized
for *All Target Locations* **do**
    if *Current Location is downstream to the inlet of current reach* **then**
        Target location moves 300m upstream
        else if *all water depths have been predicted for all reaches* **then**
            Break
            else
                Target location moves to the next reach at the junction
            end
        end
    end
    Local characteristics are collected: E, x, s, q and d_d (d from previous predictions).
    Input data is treat and normalized.
    Ensemble ANN models predict local water depths d
end
Draw cross-sections following drainage flow direction
Assign WSE to each cross-section and perform linear interpolation
Subtract interpolated WSE from DEM to generate flood depths map

4.3 Study-case

A total of seventeen urban reach segments are located in the Upper San Antonio and Leon Creek watersheds, located in San Antonio, TX Fig. 19. Eleven reaches were selected to generate synthetic datasets for the training of the ANN (red TR areas), three reaches were used in the validation (yellow VA areas), and three for testing (green TR areas).

4.3.1 Hydrodynamic Modeling

The HEC-RAS 1D was used for hydrodynamic modeling. The models used in this work are simplified and did not include any lateral and inline structures or bridges; only ineffective flow areas were set to the cross-sections where needed. Ineffective areas represent the locations in the cross-sections where flow is not conveyed due to obstacles downstream. A 3m DEM raster was acquired with San Antonio River Authority (SARA) (personal communication, September 18, 2018) and was used to draw the cross sections.
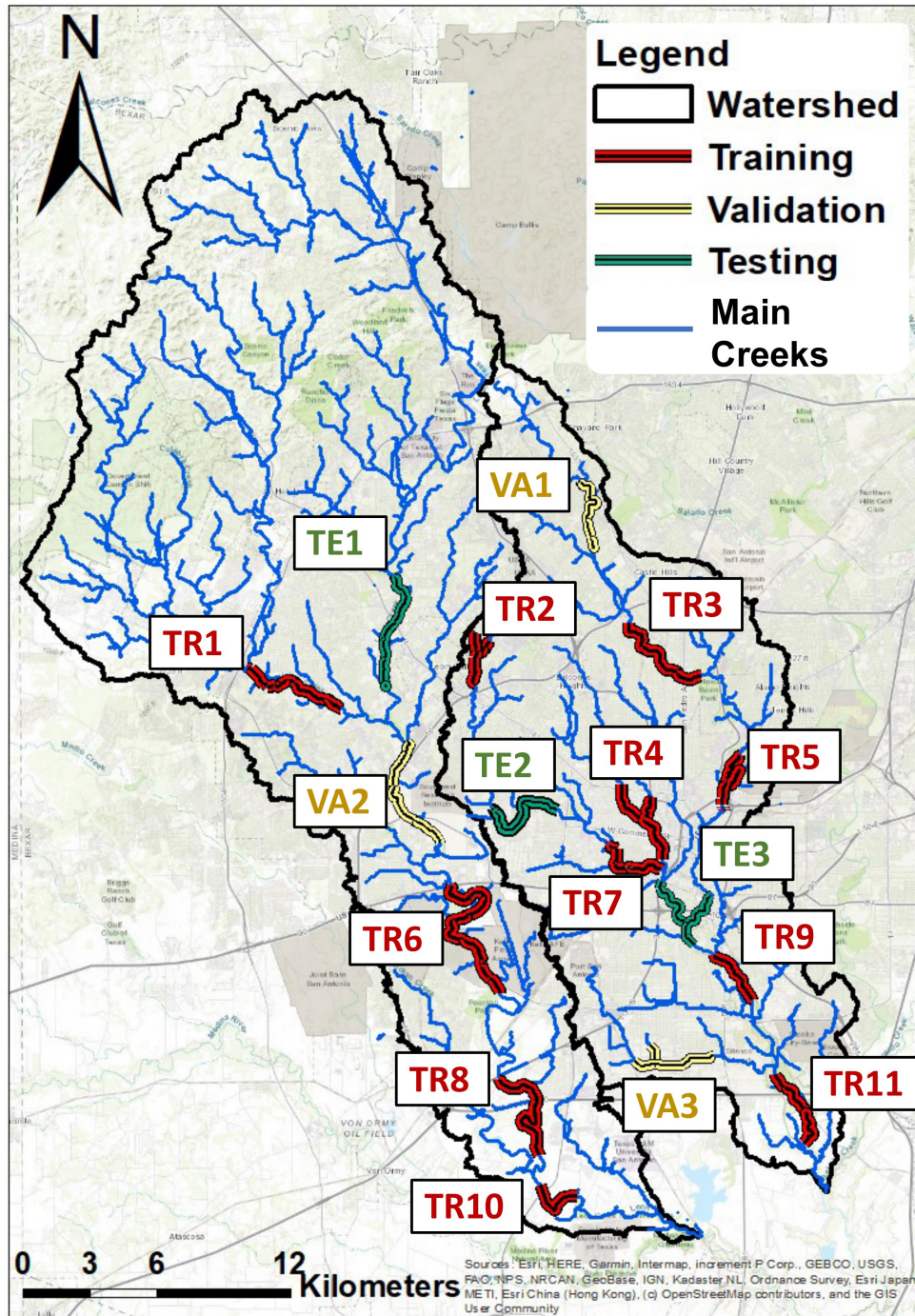
Figure 19 – Location of HEC-RAS models used for training (red) and validating (yellow), and testing (green) the ANN model.

Table 8 – Reference peak flows (500-year storm and 24 hours duration) for the training, validating and testing areas.

Area	Reference Peak flow (m³/s)	
	Inflow 1	Inflow 2
TR1	906	-
TR2	227	142
TR3	481	-
TR4	368	283
TR5	311	227
TR6	3,115	-
TR7	1,133	-
TR8	3,313	-
TR9	2,690	-
TR10	3,398	-
TR11	3,058	-
VA1	510	-
VA2	2,832	-
VA3	341	173
TE1	1,840	-
TE2	594	-
TE3	1,902	911

TE3 area is a simplified HEC-RAS model developed to access climate change impacts in San Antonio (LAGO *et al.*, 2021a). This 1D/2D model initially included 21 bridges, three culverts, and eight gates. The manning values of this model were calibrated for the main channel, impervious and pervious areas (0.035, 0.03, and 0.3, respectively). These values were applied to all HEC-RAS 1D models in this study. We used the peak flow of a 500-year storm (24-hours duration) as a reference for simulating HEC-RAS 1D models, shown in Table. 8. These areas drain different flow magnitudes, with reference peaks varying from 142 to 3,398 m³/s. The peak flows were determined with a calibrated Hydrologic Modeling System (HEC-HMS) (USACE, 2010) models for Leon Creek (GIACOMONI; OLIVERA; LAGO, 2019) and Upper San Antonio Watersheds (LAGO *et al.*, 2021a). Five out of the 17 HEC-RAS 1D models have one tributary and require two inflow hydrographs. The validation and testing areas include different peak flow magnitudes (ranging from 173 to 2832 m³/s), two areas with one junction, and different reach lengths (3.1 to 6.9 km). Therefore, these areas incorporate different characteristics to be representative of the entire training dataset.

A total of 16 different hydrograph shapes were used in HEC-RAS simulations (Fig. 20). These hydrographs were normalized by the peak flow and ranged from 0 to 1. The inflow boundary condition of the HEC-RAS models was computed by multiplying the normalized hydrographs by a pre-defined peak flow. Nine different peak flows were used to build the hydrographs, which were 60, 70, 80, 85, 90, 95 105, and 110% of the reference peak flows. The 100-year peak was approximately 60% of the 500-year peak at TE3 area

(LAGO *et al.*, 2021a). Hydrographs 1 to 8 (Fig. 20) were selected from different locations at the Upper San Antonio and Leon Creek HEC-HMS models, generated with the 500-year storm with the SCS type-III distribution. Despite the difference in flow magnitude, the hydrographs at most locations in both watersheds can be represented by one of these selected shapes. Hydrographs 9 to 16 are synthetic, a result of a combination of two or more observed hydrographs. These additional hydrographs were created to increase the number of HEC-RAS simulations and training/validation samples.
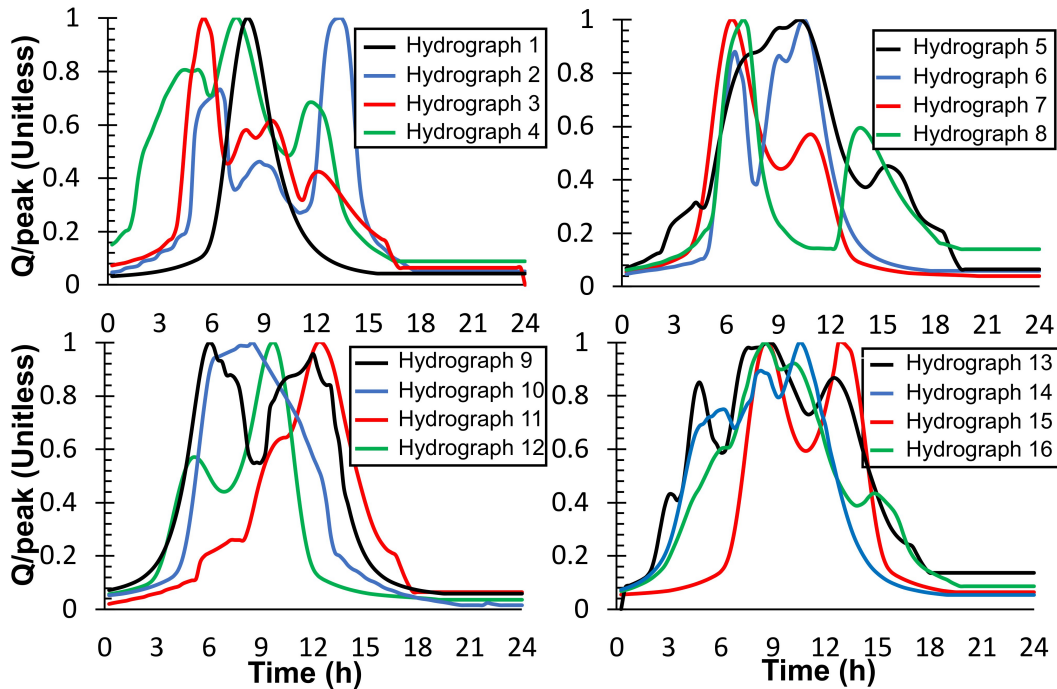
Figure 20 – Hydrographs used in HEC-RAS 1D simulations

In addition to the variety of hydrographs, simulations with all the terrain modifications were performed for each TR and VA reach segment. Terrain modifications at areas TR1 and TR3 were done between 0.6 to 1, instead of 0.8 to 1.2, due to numerical instability problems during 1D simulations for terrain modification larger than 1. Terrain modification was not applied to TE areas, as only the original area was used to evaluate the model's performance. A total of 1269 simulations (16 hydrographs, nine peak flows, and nine elevations) were performed for each of the 14 HEC-RAS 1D models in the TR and VA areas. Python codes were created to automate the modifications on the unsteady flow and geometry files used by HEC-RAS, run the models, and read discharge and WSE results for each cross-section. Due to a large number of simulations, the HEC-RAS report file was read after each simulation to identify whether it was unstable and to fix the model's geometry if necessary. Therefore, it guarantees that all simulations had stable results and did not compromise the ANN training process.

4.3.2 Data acquisition

The hydrographs and water depths used for training the ANN were acquired from HEC-RAS results. These time series data have a duration of one day with a 15-minute time step. Therefore, they are vectors with dimensions 96x1 to be inserted in the ANN. d_d 300m downstream to the target location has also 96x1 shape, representing a boundary condition that affects flow upstream (see Fig. 35.

For the E, x, and s inputs for the ANN, SARA's DEM resolution were resampled from 3 to 21m. Using lower-resolution data, which is more accessible, allows the application of the ANN regions where detailed data is scarce. BERKHAHN; FUCHS; NEUWEILER (2019) reduced the DEM resolution for predicting urban flooding with ANN. The authors argue that spatial resolution is less relevant for data-driven models (such as ANN) when compared to physically-based ones. The E is a 2D matrix of the shape of 31x31 (651x651m) and the x is a vector of shape 31x1 (651m). The s input is a 1D vector with a shape of 50x1 (1050 m) that represents the river bed elevation for 525m upstream and downstream of the target location. The 500m represents a distance from where downstream conditions have a neglectable effect (CORATO; MORAMARCO; TUCCIARELLI, 2011). This distance may vary for different study areas but is still suitable for this study as the ANN is not physically-based. However, the sizes of E, x, and s might require adjustments based on the catchment, making it challenging to achieve a global generalization of the these architectures across diverse catchments.

All required data for training and validating the ANN was collected at all the intersections between each cross-section of the HEC-RAS models and the drainage line. The number of samples in each location is twice the number of cross-sections times the number of simulation, due to mirroring. Therefore, in this study, the training and validation datasets had about 2.5 and 0.8 million samples.

4.4 Performance Evaluation and Floodplain Prediction for Large Scale Domain

Flood maps generated for validation and testing areas with this new ANN approach were compared to HEC-RAS model. As the validation dataset can be biased (WU *et al.*, 2013), these areas were also included in the analysis to be compared to the testing dataset. If the validation dataset is biased, the performance of the ANN training process might be compromised with unrealistic validation loss values (SHIN *et al.*, 2016). As a consequence, the final optimized parameters of the ANN may not be suitable for other areas with the worst performance in the testing locations. In addition, the downstream depth inputs used in the validation dataset during training differ from the ones used for floodplain generation. The reason is that the downstream depths used for training were directly acquired from

HEC-RAS models, while ANN prediction results are used to feed the ANN during the simulation (Algorithm 1, step 16). Therefore, the validation areas can also be used to evaluate the method as a whole (e.g. how error propagates upstream).

Our approach was also compared to floodplains generated with normal depth at each target location in validation and testing areas. This is similar to the GIS Flood model developed by USGS (VERDIN *et al.*, 2016). This rapid flood model consists in drawing cross-sections where normal depth is calculated. Then, the floodplain is determined by Height Above Nearest Drainage (HAND) (NOBRE *et al.*, 2011b). We used interpolation between cross-sections to generate the floodplains for comparison purposes, as HAND is more indicated to large-scale studies where minor details can be neglected(HOCH *et al.*, 2018). In contrast to the previous chapter that focused on predicting pluvial flooding, fluvial floodplains exhibit a more consistent variation in WSE. For instance, HEC-RAS 1D models interpolate WSE between cross sections to produce flood maps (BRUNNER, 2016). This uniformity enabled the conversion of water levels at discrete points.

This new approach was also tested for the whole Upper San Antonio Watershed. The DEM, drainage lines, and inflows were the data required for the simulation (Fig. 21). This watershed includes a flow diversion from an underground tunnel and two storage units. The flow diversion effect on the WSE is modeled with the correspondent peak flow in the given area, previously simulated with the hydrological model. The WSE for the storage units was determined via storage-discharge and storage-elevation curves for Elmendorf Lake and Olmos Dam. These curves and the official 100-year peak flows were acquired at the San Antonio River Authority (SARA) website (SARA, 2020). The 100-year peak flows were used to create the inflows to the model with the proper hydrographs selected for each location, shown in Fig. 20. The final flood map was then compared to 100-year Flood Insurance Rate Map (FIRM) FEMA maps. The comparison with the FEMA map excluded locations where data was generated for training and validation to avoid the influence of the training process.

The performance of the ANN model was accessed with Root Squared Mean Error (RSME), Mean Absolute Error (MAE), Hit Rate (HR), False Alarm Ratio (FAR), and Critical Success Index (CSI). HR, FAR and CSI metrics are given by Eqs. (4.6)-(4.8):

$$HR = \frac{Hits}{Hits + Misses} \tag{4.6}$$

$$FAR = \frac{False\ Alarms}{False\ Alarms + Hits} \tag{4.7}$$

$$CSI = \frac{Hits}{Misses + False\ Alarms + Hits} \tag{4.8}$$
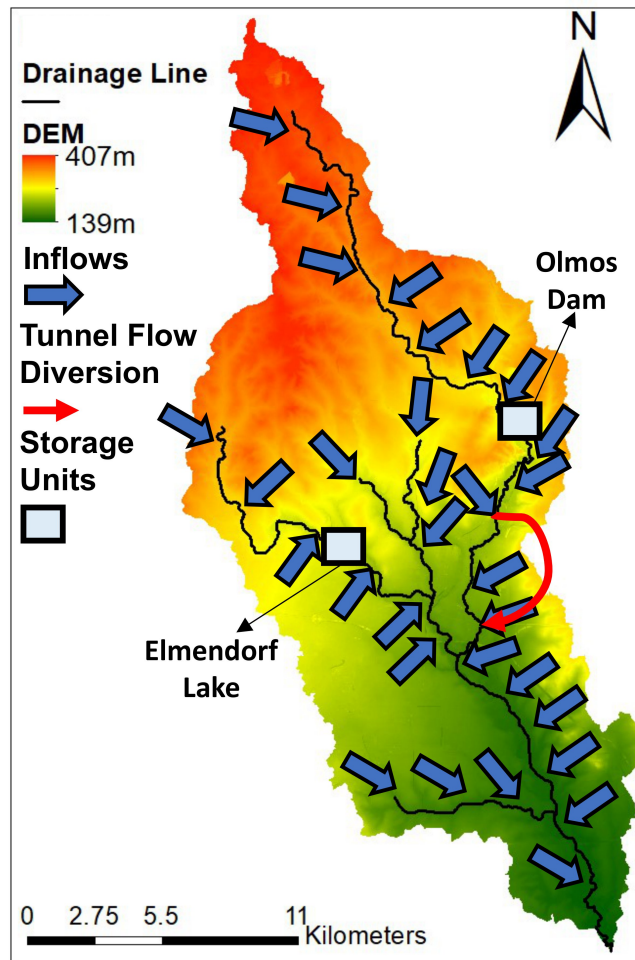
Figure 21 – Data used for the prediction of WSE with ANN

4.4.1 Hardware Specifications

All ANN and HEC-RAS simulations were performed on an i7 10700 CPU operating at 2.9GHz. No significant computational gains were obtained when predicting flood maps with the ANN method using NVIDIA GeForce RTX 2060 SUPER GPU (operating at 1650 MHz), possibly due to interaction between ANN outputs in the algorithm to generate the floodplains.

4.5 Results and Discussion

4.5.1 ANN Training

The final configurations found for each topology are presented in Table 9. The validation loss is similar to all topologies, ranging from 0.274 to 0.296m. It is worth noting that despite the loss unit being meters, it has no physical meaning. Fig. 22-a shows an example of the training and validation losses for each epoch for topology. The validation

Figure 22 – Example of training and validation loss (a) and effect of input data on validation (b) for topology 1

loss drops approximately to the 100th epoch and then increases, suggesting an overfitting of the ANN beyond that. The optimized ANN was saved at the epoch of minimum validation loss.

Table 9 – Topologies and minimum validation losses.

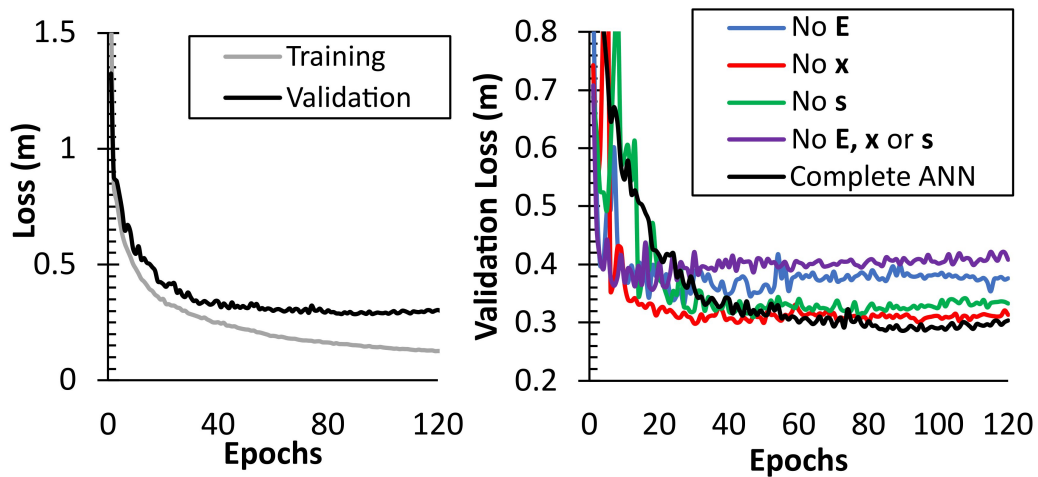|		Validation Loss (m)	f1	f2	f3	f4	k1	k2	k3	k4	D1	D2	D3	D4
Architecture 1	Topo. 1	0.285	64	32	32	16	3	2	3	2	1024	512	512	256
	Topo.2	0.274	32	32	16	16	3	2	2	2	512	256	512	256
	Topo.3	0.297	32	32	64	32	3	2	3	2	512	512	512	256
	Topo.4	0.277	64	32	64	32	3	2	3	2	512	256	512	256
Architecture 2	Topo.5	0.284	128	64	64	32	3	2	3	2	256	128	256	128
	Topo.6	0.278	64	32	32	16	3	2	3	2	512	128	1024	512
	Topo.7	0.277	64	32	32	32	3	2	3	2	256	128	512	256
	Topo.8	0.296	64	32	64	32	3	3	3	2	256	128	256	128

The contribution of each input was also evaluated and is shown in Fig. 22-b. The x and s were the inputs with the lower contribution to the ANN, with minimum validation losses 5 and 8% higher than the complete ANN, respectively. This lower contribution was expected, as x and ss can be acquired, somewhat, from E input. The E input contributed to reducing the validation loss by 16%. The no x validation curve drops faster, with minimum validation loss between the 20th and 40th epochs. The no E and no s curves had an unstable learning process for the first epochs and reached the minimum validation loss between 40th and 60th epochs. The models started overfitting at the first epochs for ANN without local information and showed no learning progress.

4.5.2 ANN Performance

The performance of the ANN approach to predict WSE was compared to the HEC-RAS 1D results for the validation and testing areas for 100 and 500-year storms

(Table 10). Despite the fact that validation areas can be biased, the performance of the ANN method for the testing areas is similar to the validation ones. Therefore, the ANN training process was suitable to allow generalization. The RSME varied from 0.25 to 0.89m and can be considered significant compared to other rapid floods, such as the WCAD2D (GHIMIRE *et al.*, 2013), with RMSE ranging from 0.10 to 0.36m. However, in their study, the floodplain were generated for a rain-on-grid problem and the RSME was calculated for every flooded cell above 0.1m. Therefore, the number of shallower flood cells for the whole domain is larger. The flood plains included the testing and validation areas that can reach high water depths (e.g. 10m in TE3, (see Appendix C) and increase RSME. As a comparison, the calibration of water depth for area TE3 (LAGO *et al.*, 2021a) was performed with two gauges. With five observed events, the maximum error in peak depth simulated with the HEC-RAS model was 0.64m. In approximately 28km of reach simulated for validation and testing areas, the maximum peak depth error was 1.15m for the 500-year storm at VA2. Overall, the outputs of ANN methos is comparable to the ones generated with HEC-RAS models. The flood depths for each validation and testing area can be seen in Appendix C.

The RSME was larger where the floodplain is more constrained, which makes water level variation more significantly with discharge. This phenomenon contributed to reducing the error on the floodplain and on the HR, FAR, and CSI metrics. TE2, for instance, had the lowest RSME value for the 100-year and worse HR, FAR, and CSI values than VA2 (with the highest RSME). The WSE profile of VA2 and TE2 can be compared in Fig. 23-a. It can be seen that the WSE predicted by ANN and HEC-RAS agree for most locations at VA2 (Fig. 23-b). Up to point 1, ANN slightly overestimates the WSE. A constraint in terrain in this location reduces the flow and increases water depths, followed by a sudden drop in riverbed elevation. Therefore, the WSE is slightly overestimated as the ANN could not predict it. This error does not propagate to location 1, where HEC-RAS and the ANN water depth series match. However, the ANN significantly overestimates the WSE in point 2. The reason is a lateral diversion where the water is stored. This diversion contributes to decreasing water depths downstream, but the ANN does not predict it. This characteristic is not included in any of the training locations and could not be learned by the ANN. This lack of accuracy highlights the importance of a broad training dataset covering different locations. The error upstream to this point reduces, as shown by the WSE from points 2 to 3. The maximum error at VA2 is 1.1m, which can be seen in the area where the water is stored. However, this overestimation by the ANN was not enough to overflow in this location and contributed to a good performance of HR, FAR, and CSI. In area TE2, on the other hand, the ANN approach overestimated the WSE until approximately 4000m distance from downstream location. Despite the error being significantly smaller than in VA2, it increases the flood extent along the reach (Fig. 23-c) which increased the FAR (14.1%). The reason is the low-relief terrain at the over-banks in this region. After the

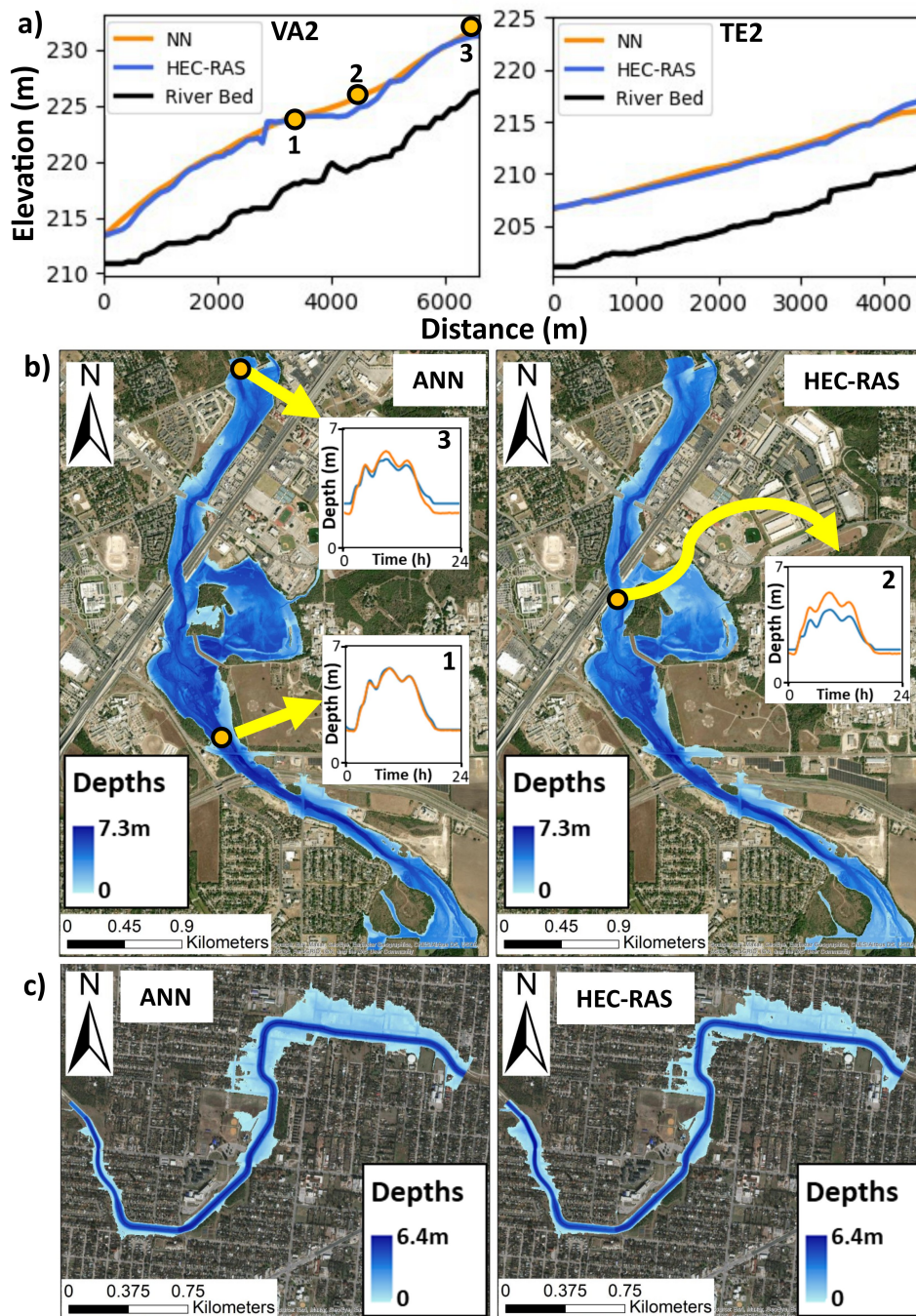4000m, the ANN underestimated the flood extent when compared to HEC-RAS.

Figure 23 – WSE predictions with HEC-RAS and ANN models for 100 and 500-year storms on validation and testing areas

Table 10 – Evaluation of Flood Plains Computed with Normal Depths

Area	Storm	ANN					Normal Depth				
		RSME	MAE	HR	FAR	CSI	RSME	MAE	HR	FAR	CSI
VA1		0.5	0.4	98.8%	1.2%	87.6%	0.65	0.48	98.1%	1.9%	90.8%
VA2		0.89	0.67	92.5%	7.5%	91.6%	1.28	1.05	86.2%	13.8%	82.2%
VA3	100-year	0.34	0.3	93.1%	6.9%	82.5%	0.64	0.42	79.7%	20.3%	74.0%
TE1		0.58	0.45	90.3%	9.7%	81.9%	1.04	0.83	71.8%	28.2%	50.1%
TE2		0.31	0.26	85.9%	14.1%	82.3%	1.05	0.94	49.5%	50.5%	49.5%
TE3		0.48	0.35	97.4%	2.6%	95.8%	0.56	0.44	93.4%	6.6%	90.1%
VA1		0.45	0.37	98.0%	2.0%	92.1%	0.56	0.4	94.8%	5.2%	91.7%
VA2		0.89	0.65	84.9%	15.1%	84.1%	1.45	1.18	77.8%	22.2%	76.5%
VA3	500-year	0.25	0.19	96.2%	3.8%	91.3%	0.73	0.54	70.6%	29.4%	68.7%
TE1		0.57	0.48	93.4%	6.6%	88.0%	0.88	0.71	67.1%	32.9%	57.2%
TE2		0.35	0.29	87.2%	12.8%	84.8%	1.45	1.31	40.4%	59.6%	40.4%
TE3		0.67	0.59	97.9%	2.1%	85.2%	0.78	0.65	85.4%	14.6%	85.2%

The errors of the floodplains determined with the ANN are significantly lower than computing it with a single or normal depth or calculating the normal depth at each target location (Table 10). Simulation with the ANN presented better values for all metrics in all locations, showing that normal depths presented a higher percentage of misses and false alarms. These results highlight the weakness of using normal depth for flood prediction, especially in natural reaches. Normal depths require some specific conditions to occur. First, the flow must be uniform with constant hydraulic parameters over several cross-sections (e.g., bottom slope, wetted area, and water level) so that there is a dynamic equilibrium between accelerating and resistance forces. Therefore, the water velocity is kept constant within the segment. Even though normal depths are widely used for channel sizing, such conditions are unlikely to happen in real case reaches (PORTO, 2006). Consequently, assuming normal depth and uniform flow for flood predictions increases the uncertainty. In addition, Manning's equation was formulated assuming steady flow, as flood wave propagation in the channel breaks the equilibrium of forces and variable flow prevails. However, in this study, all simulations were performed with the unsteady flow, which can also compromise estimating floodplains and can be relevant in real-time predictions.

The increase in WSE error (reflected by the RSME and MAE) significantly affected the areas with a low relief terrain outside the riverbanks, such as VA3, TE1, and TE2. In areas VA1, VA2, and TE3, where the floodplain is more confined, the errors on WSE assuming normal depth had a lower impact on the HR, FAR, and CSI metrics. These results agree with VERDIN *et al.* (2016)'s finding when comparing the GFT, which uses normal depth for flood prediction, with hydrodynamic models. The authors stated that GFT model should be avoided in areas with a low relief terrain.

The comparison between TE1 (low relief terrain) and VA1(well-defined relief) is illustrated in Fig. 24 a and b. At the southern portion of the TE1 domain, up to 3000m from downstream, the normal depth was below what was predicted with HEC-RAS,

underestimating the flood extent and WSE. Between 3000m and 4000m, it can be seen that the river bed becomes flattered, and the bottom slope decreases. In addition, there is a decrease in the river width and, consequentially, in the wetter area. The combination of these two conditions increased the WSE and generated a large floodplain to the west. One possible explanation is the lack of momentum conservation by this approach. Simplifications that ignore the inertia and conservation of momentum can cause higher water levels than expected for flatter areas. This issue has also been reported in simplified 2D models where Manning's equation determines flow between cells (GUIDOLIN *et al.*, 2016). This phenomenon, however, could be captured by the ANN and did not compromise its results, as the predicted WSE line is close to the HEC-RAS one. The error in area VA2 is smaller, as the terrain and river characteristics are more uniform than in TE1, and the water level simulated with HEC-RAS is closer to the normal depth. The maximum error using normal depth in area VA1 occurs at approximately 2500m from downstream, where there is a sudden drop in the river's elevation and the calculated normal depth is low. As the area's flow has a well-defined relief, the difference in the flood extent was reduced.
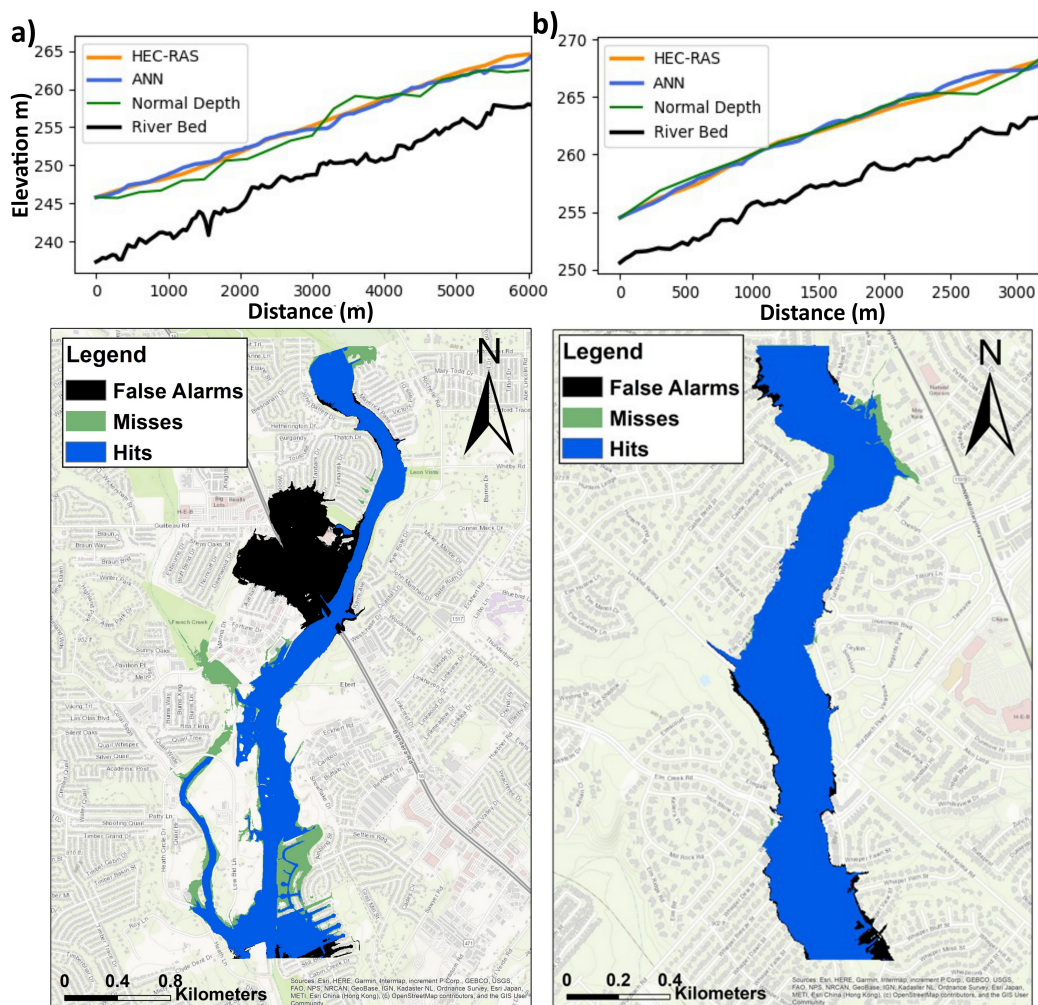

Figure 24 – Comparison Between Flood Maps Generated with HEC-RAS 1D and Normal Depths for TA1 (a) and VA1 (b)
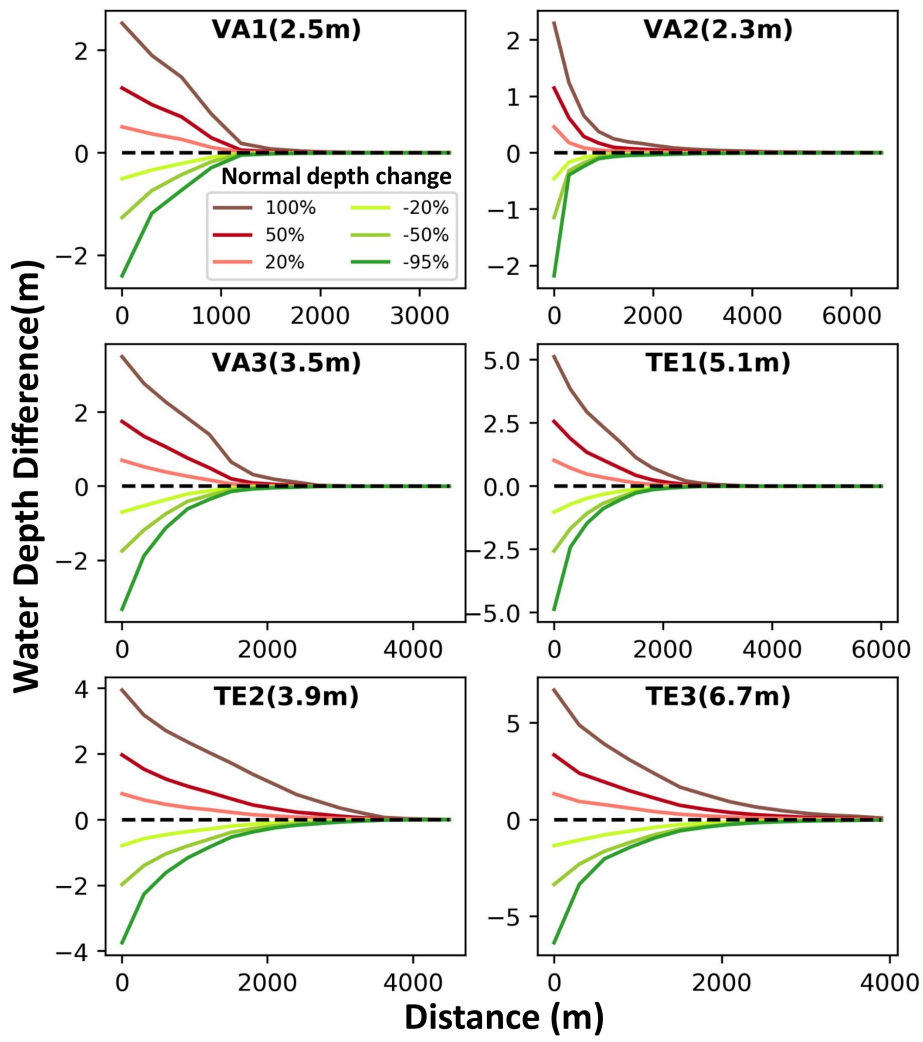
Figure 25 – The effects of downstream water depths
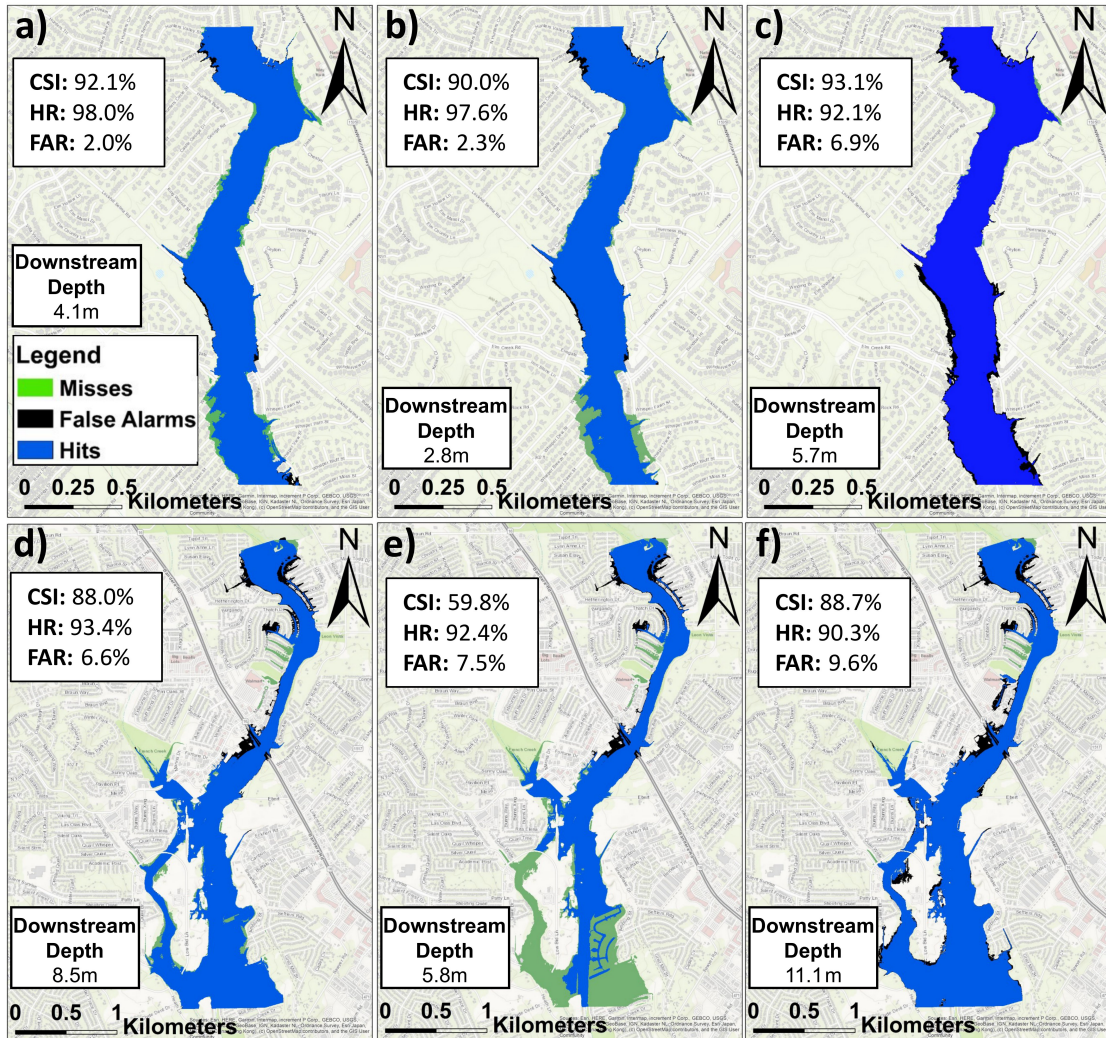
Figure 26 – The impact of downstream boundary conditions on ANN's capability to produce flood maps is illustrated. The first column displays the floodplain, utilizing the original slope to determine the normal depth as the boundary condition. In contrast, the second and third columns demonstrate the changes in floodplain predictions when employing a slope five times larger and five times smaller than the original downstream slope, respectively.

A sensitivity analysis on the downstream condition was evaluated (Fig. 25) . It can be seen that the difference in water depths, relative to no change in downstream conditions, reduces as the predictions move upstream. Eventually, the ANN predictions tend to normalize, and the downstream conditions do not affect the results. In general, the water depths tend to normalize quicker for lower downstream conditions. The larger the depth downstream, the longer it takes for the results to normalize. At areas TE1 and TE3, for instance, the depth difference becomes irrelevant at approximately 3000m. In area VA1 (with a downstream depth of 2.5m), on the other hand, the difference in predictions tends to zero at approximately 1500m. These results show that the ANN was able to understand unrealistic water depths for a given hydrograph. This capacity of the ANN

to reduce error as the simulation moves upstream is essential for the robustness of the model, especially for simulations of long streams. If the domain has an area where the ANN does not perform well (e.g., in VA2 as previously discussed). In that case, the error in this location will not propagate indefinitely upstream and compromise the final result. On the other hand, the influence of the downstream boundary condition may represent legitim flow conditions, such as the backwater effect (higher depths) or flow divergence downstream (lower depths).

To evaluate the effect of downstream conditions on the floodplain, the normal depths on the HEC-RAS and ANN models were artificially modified by multiplying and dividing the downstream slope boundary condition by five. A higher slope increases the flow capacity and reduces the downstream normal depth. This analysis was done with areas VA1 and TE1 (high and low influence of the downstream boundary condition) for the 500-year storm and to compare the flood maps generated with normal depth. The flood maps with the original downstream depths for areas VA1 and TE1 and shown in Figs. 26-a and d, which are more accurate than floodplains predicted with normal depths (Fig. 24). Results show that the ANN method was not able to reproduce floodplains for low water depths downstream (Figs. 26-b and e). The reason is that the depths in the HEC-RAS model increased almost instantaneously, and the floodplains were almost unaltered. As the ANN depths take longer to increase until they reach the original condition, the floodplain is significantly underestimated in locations closer downstream. For example, in area TE1, where there is an adjacent river in the west, the water level was not high enough to flood it as HEC-RAS model results indicate. The performance of the ANN in such drainage conditions can be improved with further training with steeper flow conditions. Between all training, validation, and testing areas, the highest slope used at the downstream condition was 0.84% in TR2 (with a terrain modification of 1.2). The maximum modified slopes for this analysis in VA1 and TE1 were 3 and 1.3%, respectively. However, as 1D modeling is less detailed than 2D hydrodynamic models, they can be more unstable, especially in areas with steep profiles with high velocities (LOGAH *et al.*, 2017). Therefore, increasing datasets with locations with a steeper profile or applying terrain modification larger than 1.2 may be challenging. In this study, in particular, the major instability issues were detected for terrain modifications of 1.2. Despite the longer simulation times required for the 2D modeling, it might be indicated for generating datasets with steeper conditions.

The ANN predictions with increased downstream depth were accurate (Figs. 26-c and f). For this condition, ANN slightly overestimated the flood plains near the downstream, increasing FAR and decreasing HR. However, the model's overall performance (CSI) improved compared to the original downstream due to a larger extent of the floodplain for both locations and lower missed areas.
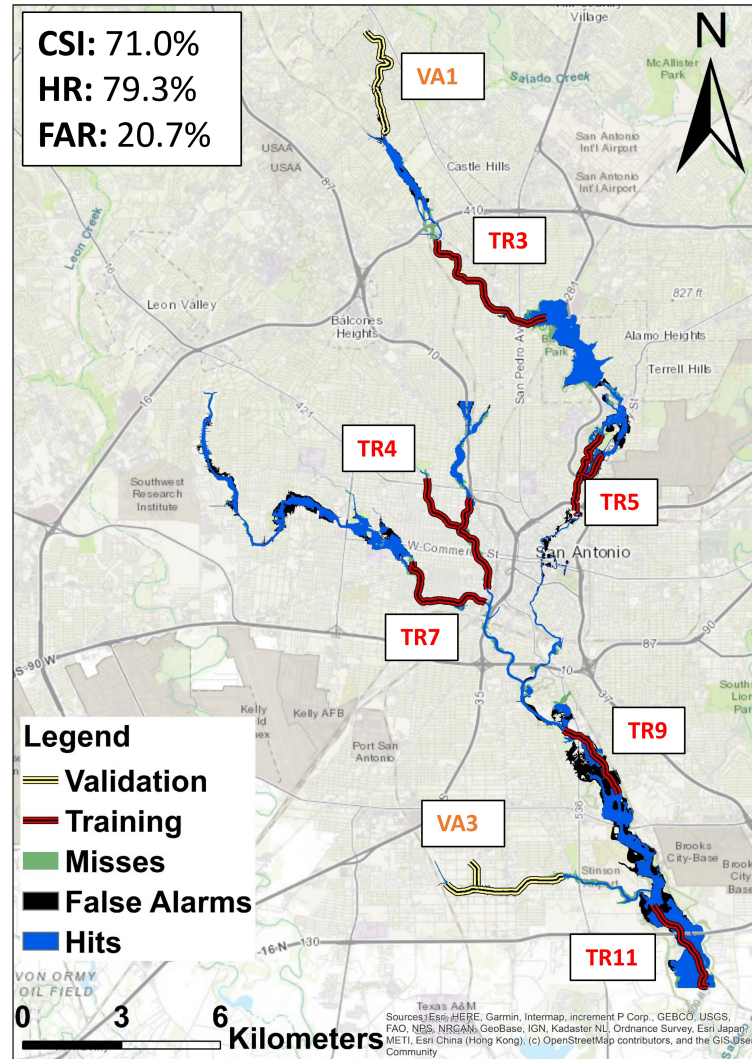
Figure 27 – Hits, misses, and false alarms of the ANN floodplain compared to FEMA map for Upper San Antonio Watershed

4.5.3 Large Scale Flood Plain Simulation

The 100-year floodplain generated for the major reaches in Upper San Antonio Watershed was compared to FEMA maps with hits, false alarms, and misses (Fig. 27). JAMALI *et al.* (2019), for intance, developed a cellular automata model(CA) for rapid flood prediction, with CSI values ranging from 69.3 to 82.8%, 85.5 to 94.8%, and 8.96 to 26.5%, respectively. The HR of CA developed by GHIMIRE *et al.* ranged from 70 to 91% and the FAR from 8 to 34%. The CSI metric for the rapid flood models tested by (BERNINI; FRANCHINI, 2013) ranged from 64.8 to 86.9%. KABIR *et al.* evaluated CNN and support vector regression (SVR) for flood predictions against hydrodynamic modeling. The HR varied from 89 to 99% with CNN and from 74 to 97% with SVR.WOZNICKI *et al.* (2019) used random forest (RF), another type of machine learning, to generate floodplains with 30m resolution for the entire continental U.S. Their HR was 79% compared to FEMA 100-year maps. Although these models were applied to different studied areas around the

world, these metrics values are comparable to the ones found in San Antonio using the DL approach.

However, the FEMA maps were generated with highly detailed HEC-RAS models for Upper San Antonio, including all infrastructures that affect flow dynamics (e.g. bridges and weirs). The simplification of the HEC-RAS models used to train the ANN compromise reduced its performance compared to FEMA maps. San Antonio downtown (downstream to TR4 and TR7), for instance, includes many bridges that increase energy loss and, consequently, water level. This phenomenon is modeled with HEC-RAS but was not captured by the ANN. Therefore, the ANN approach underestimated the floodplain in this region. TR9 is another location in which the ANN and the FEMA maps disagree, where ANN is overestimating. Other modeling characteristics, such as different Manning's n than the one used for training, can explain this difference. Despite the differences in the models used for training and creating the FEMA maps, the ANN maps agree reasonably with FEMA where flooding is likely to occur.

FEMA (2013) points out that creating an HEC-RAS model is very time-consuming and labor-intensive and should be considered while developing a floodplain study. These drawbacks can hamper estimating floodplains in an emergency for locations where no hydraulic model is available. In addition, reliable modeling tools require high-quality data (APEL *et al.*, 2009). Although the major cities in developed countries have reliable hydrodynamic models and high-resolution data, this might not be the reality in developing countries. This lack of data or models is a major concern, as cities in developing countries usually have worse drainage and warning systems, placing the population at a higher risk. Data scarcity hampers flood risk assessments in developing countries, as the lack of funding prevents acquiring reliable and detailed input data for flood models (WANNOUS; VELASQUEZ, 2017; GLAS *et al.*, 2019). Despite using a 3m resolution DEM to generate the floodplains with the hydrodynamic model, the approach proposed in this study uses a 21m resolution DEM, which is more accessible, with similar outputs compared to the hydrodynamic model. These results suggest ANN can be used to improve flood modeling in these countries and the safety of the population.

Another advantage of this approach is the total simulation time. The WSE prediction with the ANN for the whole Upper San Antonio Watershed took 84 seconds (0.9 s/km). As a comparison, the HEC-RAS simulation for TR1(100-year storm) was 138 seconds (23s/km). Thus, the ANN approach was more than 20 times faster than the HEC-RAS 1D simulation. However, this difference could be even more considerable if an HEC-RAS model was used to simulate the whole Upper San Antonio watershed. The more complex the HEC-RAS model is, the more iterations are necessary for the numerical solutions. Despite the 1D hydrodynamic being relatively fast, the difference in simulation time can be significant for optimization problems to minimize floodplains since hundreds

of thousands of simulations may be necessary. In addition, there is no guarantee that all simulations will generate stable results with the hydrodynamic modeling, which is also a disadvantage of hydrodynamic models pointed out by (FEMA, 2013).

4.6 Conclusion

In this paper, we developed a new model to predict flood maps using ANN, which simply requires the DEM and inflows as inputs. The proposed approach is also significantly faster than the 1D hydrodynamic simulations. This model was evaluated for three validation and three testing areas with satisfactory results. In addition, simulation on large domain was also performed and compared to FEMA maps. Despite the much simpler HEC-RAS models used for training the ANN, the floodplains generated with our model matched FEMA's floodplains reasonably.

This novel approach helps improve the state-of-art of ANN applied to flood studies, which could generalize flood modeling to different areas. However, there are still many research opportunities to increase the performance of this approach. We recommend increasing the number of training locations for the ANN to capture the nuances of different river reaches. Enhancing the variability of the dataset with river segments from several locations increases the model's capacity to recognize different flow characteristics. With more data and training, the predictions of the ANN are likely to get closer to the hydrodynamic model. With enough data variability, the same ANN can eventually be applied to most locations without the need of retraining it.

Further improvements are also suggested to the models used for training. In this paper, we assumed the same Manning's n for all models. However, varying Manning's n can make the ANN sensitive to its values. In addition, inline and lateral hydraulic structures can also be added to the hydrodynamic models used for training and as inputs to the ANN architectures. Including such structures can be a significant improvement to rapid flood models. For instance, to the best of our knowledge, no rapid flood model yet considers bridges to predict floodplains. Additionally, more training might be essential to sustain its efficiency in catchments with distinctly different features, like non-dendritic ones.

Despite the limitations of the proposed models, the results in this paper suggest that ANN, with the suggested improvements, can be used as a reliable surrogate model for floodplain mapping with many practical applications. For example, faster simulations can be an advantage in real-time flood predictions and optimization problems, where the simulation time can be significant. Another advantage is the simplicity of the input data and simulation approach. The ANN can be trained in areas where data is abundant and reliable hydrodynamic models are available to be later applied where it lacks. This strategy can increase the accuracy of flood predictions, especially in developing countries where funding is scarce, and improve the security of the local population.

5 GENERAL CONCLUSIONS

This dissertation has explored the potential of deep learning techniques, specifically artificial neural networks (ANNs), in flood prediction and floodplain mapping. It demonstrated the ability of ANNs and conditional generative adversarial networks (cGANs) to model and predict urban flood events, and assessed their performance in diverse geographic locations.

5.1 Summary

Chapter 2 revealed the capacity of cGAN-Flood to accurately reproduce hydrodynamic 2D models' results when used to improve flood mapping resolution. They significantly reduced computational time and demonstrated the capability to be applied at the watershed scale (Upper San Antonio Watershed). The application of DL models improving the resolution of coarse flood models is novel, which opens the possibility to improve flood maps of existing hydrodynamic models. This emphasized the versatility and computational efficiency of ANNs in modeling flood events in large-scale domains, demonstrating that the **research objective 1** was accomplished.

In Chapter 3, cGAN-Flood, was evaluated in a novel geographic context, to explore its generalization capabilities and reach **research objective 2**. Although the model's performance decreased when applied to catchments in Sao Paulo, different from its training ground in San Antonio, it managed to reasonably improve flood mapping resolution. This experiment demonstrated the ability of trained DL models to adapt to different catchments, given that they are trained with a diversity of topological patterns.

Chapter 4 introduced a new model for flood map prediction using ANNs, that only requires digital elevation models (DEMs) and inflows as inputs. It outperformed traditional hydrodynamic simulations in terms of speed, and its large-scale simulation comparable to FEMA's floodplains. The satisfactorily predictions of the model, combined with its computational performance, shows that **research objective 3** was met.

DL models have shown significant potential for use in flood prediction and floodplain mapping. They can simplify and speed up flood predictions, making them useful for real-time applications and optimizing mitigation strategies. Furthermore, with the appropriate training, DL models can be applied to diverse locations without the need for re-training. This thesis demonstrate that DL models are a viable tool to be applied to large scale-flood predictions, which was the **main objective** of the thesis. The DL models were capable of reproducing hydrodynamic outputs with a significant reduction in simulation times. However, there is a need to advance DL technologies to overcome its limitations as discussed

in the following section.

5.2 Recommendations for Future Studies

Despite the satisfactorily performance of DL models presented in this thesis, in terms of prediction and simulation times, there is still a need for model improvements to increase accuracy and reputability of their predictions, as listed below:

Inclusion of Underground Drainage Systems: The cGAN-Flood model does not currently account for underground drainage systems. Their inclusion could significantly improve flood prediction in urban areas where such systems significantly influence flood dynamics. Future studies should focus on incorporating these systems into the model.

Validation against calibrated models: The deep learning models were trained and tested using non-calibrated models. An assessment is required to determine the potential enhancement in predictions when utilizing calibrated models.

Rainfall Distribution: The cGAN-Flood model allocates the flood volume based on a uniform rainfall distribution. The implications of spatially varying rainfall on the outcomes warrant additional exploration.

Soil moisture conditions: HEC-RAS models used for training the cGAN-Flood model used a constant initial soil moisture. It would be beneficial to conduct a sensitivity analysis to discern the situations and locations where pre-event hydrological conditions impact the modeling outcomes.

Model Adaptability to Various Resolutions: The cGAN-Flood model is confined to a 3m raster resolution. This limitation hinders its application in scenarios where data resolution varies or where more detailed flood predictions are necessary. Therefore, adaptability of the model to work with varying resolutions should be a focal point for future research, broadening its application scope.

Parallelization: The cGAN-Flood model is employed on smaller catchments to distribute the flood volume independently when dealing with a large study domain. This approach allows for potential parallelization, further improving the model's computational efficiency. Additional investigation is suggested to assess computational requirements, including memory allocation, during parallelization.

Model Generalization and Training: The invtigations of this thesis shows a performance drop when the cGAN-Flood model was applied to different catchments, such as those in Sao Paulo compared to San Antonio. Future studies should prioritize training the model with a wider variety of topological patterns. This could enhance its generalization capacity and maintain accuracy when applied to diverse catchments. Capturing nuances from different locations can improve the model's capacity to recognize diverse flow characteristics, leading to more accurate predictions.

Hydraulic Structures: Inline and lateral hydraulic structures should be added to the hydrodynamic models used for training. Including structures in the models used for training could lead to significant improvements in rapid flood models. Furthermore, structures requires reliable data to be implemented in hydrodynamic models and are often a major source of model instability of hydrodynamic simulations, leading to additional costs and longer simulation times. Therefore, the application of DL to such cases can be highly beneficial.

Investigate the Application of Other Deep Learning Models: The development and testing of deep learning architectures can offer valuable insights and enhancements in flood prediction. Exploring these options could provide further understanding of the most promising DL strategy to be applied for flood predictions.

Developing Real-Time Prediction Systems with DL: Given the potential of these models to support real-time predictions, future research could explore DL with focus on developing robust real-time flood prediction systems. This can be crucial in flood management and mitigation, especially in areas prone to severe flooding.

Improving Flood Modeling in Developing Regions: This research suggested that the models could be trained in data-rich areas and then applied in areas where such data are lacking, due to the promising generalization potential of DL models. This opens a the oportunity for improving flood prediction accuracy in developing countries where resources are scarce.

Predicting Flash Floods and Landslides: Considering the severe impacts of flash floods and landslides, future research should focus on enhancing DL models to better predict these phenomena more rapidly. Real-time data sources, such as satellite imagery and ground sensors, combined with historical incident data can be used to train a DL model to support prediction and mitigation of flash floods and landslides.

Evaluating Climate Change Scenarios: The great uncertainty of climate model leads to many possible future projected scenarios. Evaluating this large number of possible climate projections can be time consuming, especially with hydrodynamic models. As DL can improve computational efficiency and reduce simulation times, it can be an efficient tool for evaluating multiple scenarios and improve mitigation plans.

Despite the challenges, DL models hold great promise in improving the accuracy and efficiency of flood predictions, which is especially valuable in regions where funding and data are limited. As climate change projections suggests that flood risks will be exacerbated. Therefore, the development and refinement of such tools will be essential in bolstering the resilience of communities worldwide.

REFERENCES

ABADI, M. *et al.* **TensorFlow: Large-Scale Machine Learning on Heterogeneous Systems**. 2015. Software available from tensorflow.org. Disponível em: https://www.tensorflow.org/.

AFSHARI, S. *et al.* Comparison of new generation low-complexity flood inundation mapping tools with a hydrodynamic model. **Journal of Hydrology**, Elsevier, v. 556, p. 539–556, 2018.

AGILAN, V.; UMAMAHESH, N. Is the covariate based non-stationary rainfall idf curve capable of encompassing future rainfall changes? **Journal of Hydrology**, Elsevier, v. 541, p. 1441–1455, 2016.

AICH, V. *et al.* Flood projections within the niger river basin under future land use and climate change. **Science of The Total Environment**, v. 562, p. 666–677, 2016. ISSN 0048-9697. Disponível em: http://www.sciencedirect.com/science/article/pii/S0048969716307021.

ALOBAIDI, M. H.; CHEBANA, F.; MEGUID, M. A. Robust ensemble learning framework for day-ahead forecasting of household based energy consumption. **Applied energy**, Elsevier, v. 212, p. 997–1012, 2018.

ANTHONY, M.; BARTLETT, P. L.; BARTLETT, P. L. **Neural network learning: Theoretical foundations**. [*S.l.: s.n.*]: cambridge university press Cambridge, 1999. v. 9.

APEL, H. *et al.* Flood risk analyses—how detailed do we need to be? **Natural hazards**, Springer, v. 49, n. 1, p. 79–98, 2009.

ARNBJERG-NIELSEN, K. *et al.* Impacts of climate change on rainfall extremes and urban drainage systems: a review. **Water science and technology**, IWA Publishing, v. 68, n. 1, p. 16–28, 2013.

BENTIVOGLIO, R. *et al.* Deep learning methods for flood mapping: a review of existing applications and future research directions. **Hydrology and Earth System Sciences**, Copernicus GmbH, v. 26, n. 16, p. 4345–4378, 2022.

BERKHAHN, S.; FUCHS, L.; NEUWEILER, I. An ensemble neural network model for real-time prediction of urban floods. **Journal of hydrology**, v. 575, p. 743–754, 2019. ISSN 0022-1694.

BERNE, A. *et al.* Temporal and spatial resolution of rainfall measurements required for urban hydrology. **Journal of Hydrology**, Elsevier, v. 299, n. 3-4, p. 166–179, 2004.

BERNINI, A.; FRANCHINI, M. A rapid model for delimiting flooded areas. **Water resources management**, Springer, v. 27, n. 10, p. 3825–3846, 2013.

BETSHOLTZ, A.; NORDLÖF, B. Potentials and limitations of 1d, 2d and coupled 1d-2d flood modelling in hec-ras. **TVVR17/5003**, 2017.

BOMERS, A. *et al.* Historic flood reconstruction with the use of an artificial neural network. **Water resources research**, v. 55, n. 11, p. 9673–9688, 2019. ISSN 0043-1397.

BROWN, G. *et al.* Managing diversity in regression ensembles. **Journal of machine learning research**, v. 6, n. 9, 2005.

BROWN, J. D.; SPENCER, T.; MOELLER, I. Modeling storm surge flooding of an urban area with particular reference to modeling uncertainties: A case study of canvey island, united kingdom. **Water Resources Research**, v. 43, n. 6, 2007. ISSN 0043-1397.

BRUNNER, G. Hec-ras river analysis system, 2d modeling user's manual, version 5.0. **Davis: US Army Corps of Engineers, hydrologic engineering center**, 2016.

BULTI, D. T.; ABEBE, B. G. A review of flood modeling methods for urban pluvial flood application. **Modeling earth systems and environment**, v. 6, n. 3, p. 1293–1302, 2020. ISSN 2363-6211.

CARVALHO, T. M. N.; FILHO, F. d. A. de S.; PORTO, V. C. Urban water demand modeling using machine learning techniques: Case study of fortaleza, brazil. **Journal of Water Resources Planning and Management**, American Society of Civil Engineers, v. 147, n. 1, p. 05020026, 2021.

CEA, L.; COSTABILE, P. Flood risk in urban areas: Modelling, management and adaptation to climate change. a review. **Hydrology**, MDPI, v. 9, n. 3, p. 50, 2022.

CHANDRA, R.; SAHA, U.; MUJUMDAR, P. Model and parameter uncertainty in idf relationships under climate change. **Advances in Water Resources**, Elsevier, v. 79, p. 127–139, 2015.

CHEN, A. S. *et al.* Multi-layered coarse grid modelling in 2d urban flood simulations. **Journal of Hydrology**, Elsevier, v. 470, p. 1–11, 2012.

CHEN, J. *et al.* Finding appropriate bias correction methods in downscaling precipitation for hydrologic impact studies over north america. **Water Resources Research**, v. 49, n. 7, p. 4187–4205, 2013. ISSN 0043-1397.

CLAVET-GAUMONT, J. *et al.* Probable maximum flood in a changing climate: An overview for canadian basins. **Journal of Hydrology: Regional Studies**, v. 13, p. 11–25, 2017. ISSN 2214-5818. Disponível em: http://www.sciencedirect.com/science/article/pii/S2214581817301696.

CORATO, G.; MORAMARCO, T.; TUCCIARELLI, T. Combining flow routing modelling and direct velocity measurement for optimal discharge estimation. **Hydrology & Earth System Sciences Discussions**, v. 8, n. 2, 2011. ISSN 1812-2108.

COUNCIL, N. R. Book. **Urban stormwater management in the United States**. [*S.l.: s.n.*]: National Academies Press, 2009. ISBN 0309125391.

DAI, A. M.; LE, Q. V. Semi-supervised sequence learning. **Advances in neural information processing systems**, v. 28, p. 3079–3087, 2015.

DEGAETANO, A. T.; CASTELLANO, C. M. Future projections of extreme precipitation intensity-duration-frequency curves for climate adaptation planning in new york state. **Climate Services**, Elsevier, v. 5, p. 23–35, 2017.

DHI. Mike 1d-2d modelling—user manual. **DHI Water Environment**, 2011.

DIBABA, W. T.; MIEGEL, K.; DEMISSIE, T. A. Evaluation of the cordex regional climate models performance in simulating climate conditions of two catchments in upper blue nile basin. **Dynamics of Atmospheres and Oceans**, v. 87, p. 101104, 2019. ISSN 0377-0265.

DOOCY, S. *et al.* The human impact of floods: a historical review of events 1980-2009 and systematic literature review. **PLoS currents**, Public Library of Science, v. 5, 2013.

DOZAT, T. Incorporating nesterov momentum into adam. 2016.

DTISSIBE, F. Y. *et al.* Flood forecasting based on an artificial neural network scheme. **Natural Hazards**, Springer, v. 104, n. 2, p. 1211–1237, 2020.

ENGMAN, E. T. Roughness coefficients for routing surface runoff. **Journal of Irrigation and Drainage Engineering**, American Society of Civil Engineers, v. 112, n. 1, p. 39–53, 1986.

FANG, Z. *et al.* Predicting flood susceptibility using lstm neural networks. **Journal of Hydrology**, Elsevier, v. 594, p. 125734, 2021.

FEMA. **Federal Guidelines for Inundation Mapping of Flood Risks Associated With Dam Incidents and Failures**. First. [*S.l.: s.n.*]: Federal Emergency Management Agency, 2013.

FEMA. **Guidance for Flood Risk Analysis and Mapping**. [*S.l.: s.n.*]: Federal Emergency Management Agency (FEMA), 2018.

FEWTRELL, T. *et al.* Evaluating the effect of scale in flood inundation modelling in urban environments. **Hydrological Processes: An International Journal**, Wiley Online Library, v. 22, n. 26, p. 5107–5118, 2008.

GANGULI, P.; COULIBALY, P. Does nonstationarity in rainfall require nonstationary intensity–duration–frequency curves? **Hydrology and Earth System Sciences**, Copernicus GmbH, v. 21, n. 12, p. 6461–6483, 2017.

GAO, C. *et al.* Effects of climate change on peak runoff and flood levels in qu river basin, east china. **Journal of Hydro-Environment Research**, v. 28, p. 34–47, 2020. ISSN 1570-6443.

GHIMIRE, B. *et al.* Formulation of a fast 2d urban pluvial flood model using a cellular automata approach. **Journal of Hydroinformatics**, v. 15, n. 3, p. 676–686, 2013. ISSN 1464-7141.

GIACOMONI, M.; OLIVERA, F.; LAGO, C. do. **Assessing the Impacts of Super Storm Flooding in the Transportation Infrastructure–Case Study: San Antonio, Texas**. [*S.l.: s.n.*]: Transportation Consortium of South-Central States - TRAN-SET, 2019.

GLAS, H. *et al.* Flood risk mapping worldwide: A flexible methodology and toolbox. **Water**, Multidisciplinary Digital Publishing Institute, v. 11, n. 11, p. 2371, 2019.

GODIN, F. *et al.* Dual rectified linear units (drelus): A replacement for tanh activation functions in quasi-recurrent neural networks. **Pattern Recognition Letters**, v. 116, p. 8–14, 2018. ISSN 0167-8655.

GONOG, L.; ZHOU, Y. A review: generative adversarial networks. *In*: IEEE. **2019 14th IEEE conference on industrial electronics and applications (ICIEA)**. [*S.l.: s.n.*], 2019. p. 505–510.

GOULDBY, B. *et al.* A methodology for regional-scale flood risk assessment. *In*: THOMAS TELFORD LTD. **Proceedings of the Institution of Civil Engineers-Water Management**. [*S.l.: s.n.*], 2008. v. 161, n. 3, p. 169–182.

GUIDOLIN, M. *et al.* A weighted cellular automata 2d inundation model for rapid flood analysis. **Environmental Modelling Software**, v. 84, p. 378–394, 2016. ISSN 1364-8152.

GUO, Z.; MOOSAVI, V.; LEITÃO, J. P. Data-driven rapid flood prediction mapping with catchment generalizability. **Journal of Hydrology**, Elsevier, v. 609, p. 127726, 2022.

HOCH, J. M. *et al.* Benchmarking flexible meshes and regular grids for large-scale fluvial inundation modelling. **Advances in Water Resources**, Elsevier, v. 121, p. 350–360, 2018.

HOFMANN, J.; SCHÜTTRUMPF, H. floodgan: Using deep adversarial learning to predict pluvial flooding in real time. **Water**, MDPI, v. 13, n. 16, p. 2255, 2021.

INNOVYZE. **InfoWorks ICM Help**. [*S.l.*], 2012.

ISOLA, P. *et al.* Image-to-image translation with conditional adversarial networks. *In*: **Proceedings of the IEEE conference on computer vision and pattern recognition**. [*S.l.: s.n.*], 2017. p. 1125–1134.

IYER, M. S.; RHINEHART, R. R. A method to determine the required number of neural-network training repetitions. **IEEE Transactions on Neural Networks**, IEEE, v. 10, n. 2, p. 427–432, 1999.

JAAFRA, Y. *et al.* Reinforcement learning for neural architecture search: A review. **Image and Vision Computing**, Elsevier, v. 89, p. 57–66, 2019.

JAMALI, B. *et al.* A cellular automata fast flood evaluation (ca-ffé) model. **Water Resources Research**, Wiley Online Library, v. 55, n. 6, p. 4936–4953, 2019.

JAMALI, B. *et al.* A rapid urban flood inundation and damage assessment model. **Journal of Hydrology**, Elsevier, v. 564, p. 1085–1098, 2018.

JATO-ESPINO, D. *et al.* A simulation-optimization methodology to model urban catchments under non-stationary extreme rainfall events. **Environmental Modelling & Software**, Elsevier, v. 122, p. 103960, 2019.

JONKMAN, S. N. Global perspectives on loss of human life caused by floods. **Natural hazards**, Springer, v. 34, n. 2, p. 151–175, 2005.

JR, M. N. G. *et al.* Hydropol2d–distributed hydrodynamic and water quality model: Challenges and opportunities in poorly-gauged catchments. **arXiv preprint arXiv:2304.11099**, 2023.

KABIR, S. *et al.* A deep convolutional neural network model for rapid prediction of fluvial flood inundation. **Journal of Hydrology**, v. 590, p. 125481, 2020. ISSN 0022-1694.

KARIM, F. *et al.* A review of hydrodynamic and machine learning approaches for flood inundation modeling. **Water**, MDPI, v. 15, n. 3, p. 566, 2023.

KIEFER, J. Sequential minimax search for a maximum. **Proceedings of the American mathematical society**, v. 4, n. 3, p. 502–506, 1953. ISSN 0002-9939.

KUNDZEWICZ, Z. W. *et al.* Uncertainty in climate change impacts on water resources. **Environmental Science & Policy**, Elsevier, v. 79, p. 1–8, 2018.

LAGO, C. A. do *et al.* Generalizing rapid flood predictions to unseen urban catchments with conditional generative adversarial networks. **Journal of Hydrology**, Elsevier, v. 618, p. 129276, 2023.

LAGO, C. A. F. do. **Battling Climate Change Induced Flooding: Rapid Flood Modeling, Optimization, Uncertainties and Metrics**. 2022. Tese (Doutorado) — The University of Texas at San Antonio, 2022.

LAGO, C. A. F. do *et al.* Assessing the impact of climate change on transportation infrastructure using the hydrologic-footprint-residence metric. **Journal of Hydrologic Engineering**, v. 26, n. 5, p. 04021014, 2021. ISSN 1084-0699.

LAGO, C. A. F. do *et al.* Assessing the impact of climate change on transportation infrastructure using the hydrologic-footprint-residence metric. **Journal of Hydrologic Engineering**, American Society of Civil Engineers, v. 26, n. 5, p. 04021014, 2021.

LAGO, C. Ambrogi Ferreira do *et al.* Simulation and optimization framework for evaluating the robustness of low-impact development placement solutions under climate change in a small urban catchment. **Hydrological Sciences Journal**, Taylor & Francis, p. 1–18, 2023.

LAWRENCE, J. *et al.* Exploring climate change uncertainties to support adaptive management of changing flood-risk. **Environmental Science Policy**, v. 33, p. 133–142, 2013. ISSN 1462-9011.

LE, X.-H. *et al.* Application of long short-term memory (lstm) neural network for flood forecasting. **Water**, Multidisciplinary Digital Publishing Institute, v. 11, n. 7, p. 1387, 2019.

LEE, D.; DERRIBLE, S. Predicting residential water demand with machine-based statistical learning. **Journal of Water Resources Planning and Management**, American Society of Civil Engineers, v. 146, n. 1, p. 04019067, 2020.

LIU, Z. *et al.* Association between floods and typhoid fever in yongzhou, china: effects and vulnerable groups. **Environmental research**, v. 167, p. 718–724, 2018. ISSN 0013-9351.

LOGAH, F. Y. *et al.* Floodplain hydrodynamic modelling of the lower volta river in ghana. **Journal of Hydrology: Regional Studies**, Elsevier, v. 14, p. 1–9, 2017.

LOWE, R. *et al.* U-flood–topographic deep learning for predicting urban pluvial flood water depth. **Journal of Hydrology**, v. 603, p. 126898, 2021. ISSN 0022-1694.

MARTINS, V. S. *et al.* Exploring multiscale object-based convolutional neural network (multi-ocnn) for remote sensing image classification at high spatial resolution. **ISPRS Journal of Photogrammetry and Remote Sensing**, Elsevier, v. 168, p. 56–73, 2020.

MORINI, M.; PINELLI, M. **Mathematical Modelling of Energy Systems and Fluid Machinery**. [*S.l.: s.n.*]: MDPI, 2021.

MORSY, M. M. *et al.* A cloud-based flood warning system for forecasting impacts to transportation infrastructure systems. **Environmental modelling & software**, Elsevier, v. 107, p. 231–244, 2018.

MOSS, R. H. *et al.* The next generation of scenarios for climate change research and assessment. **Nature**, Nature Publishing Group, v. 463, n. 7282, p. 747–756, 2010.

NATARAJAN, S.; RADHAKRISHNAN, N. Simulation of extreme event-based rainfall–runoff process of an urban catchment area using hec-hms. **Modeling Earth Systems and Environment**, v. 5, n. 4, p. 1867–1881, 2019. ISSN 2363-6211.

NEAL, J. C. *et al.* Distributed whole city water level measurements from the carlisle 2005 urban flood event and comparison with hydraulic model simulations. **Journal of Hydrology**, Elsevier, v. 368, n. 1-4, p. 42–55, 2009.

NEARING, G. S. *et al.* What role does hydrological science play in the age of machine learning? **Water Resources Research**, v. 57, n. 3, p. e2020WR028091, 2021. E2020WR028091 10.1029/2020WR028091. Disponível em: https://agupubs.onlinelibrary. wiley.com/doi/abs/10.1029/2020WR028091.

NOBRE, A. D. *et al.* Height above the nearest drainage–a hydrologically relevant new terrain model. **Journal of Hydrology**, Elsevier, v. 404, n. 1-2, p. 13–29, 2011.

NOBRE, A. D. *et al.* Height above the nearest drainage–a hydrologically relevant new terrain model. **Journal of Hydrology**, Elsevier, v. 404, n. 1-2, p. 13–29, 2011.

NRC. **Elevation data for floodplain mapping**. National Academies Press, 2007. 1-152 p. ISBN 0309104092. Disponível em: https://www.nap.edu/catalog/11829/ elevation-data-for-floodplain-mapping.

OH, C.-W. *et al.* Hydroplaning simulation for a straight-grooved tire by using fdm, fem and an asymptotic method. **Journal of Mechanical Science and Technology**, v. 22, n. 1, p. 34–40, 2008. ISSN 1976-3824.

PAIVA, R. C. D. D. *et al.* Large-scale hydrologic and hydrodynamic modeling of the amazon river basin. **Water Resources Research**, Wiley Online Library, v. 49, n. 3, p. 1226–1243, 2013.

PANAHI, M. *et al.* Deep learning neural networks for spatially explicit prediction of flash flood probability. **Geoscience Frontiers**, v. 12, n. 3, p. 101076, 2021. ISSN 1674-9871.

PETERS, R.; SCHMITZ, G.; CULLMANN, J. Flood routing modelling with artificial neural networks. **Advances in Geosciences**, v. 9, p. 131–136, 2006. ISSN 1680-7340.

PORTO, R. d. M. Hidráulica básica. 4ª edição. **São Carlos: EESC-USP, Projeto REENGE**, 2006.

RANGARI, V. *et al.* 1d-2d modeling of urban floods and risk map generation for the part of hyderabad city. **The International Archives of Photogrammetry, Remote Sensing and Spatial Information Sciences**, Copernicus GmbH, v. 42, p. 445–450, 2018.

REPORT, H. U. G. S. **Husqvarna Urban Green Space Index**. 2019. Accessed: 01-22-2023. Disponível em: \$https://www.hugsi.green/static/hugsi_space_index_2019_report_v2_1-e4638c0d067ef9e01f0911000f57fddd.pdf\$.

ROY, Y. *et al.* Deep learning-based electroencephalography analysis: a systematic review. **Journal of neural engineering**, IOP Publishing, v. 16, n. 5, p. 051001, 2019.

SARA. Digital data modeling repository. **San Antonio River Authority.**, Available at <https://d2mr.sara-tx.org/>, as of July 2nd 2020., 2020.

SCHWANGHART, W.; SCHERLER, D. Bumps in river profiles: uncertainty assessment and smoothing using quantile regression techniques. **Earth Surface Dynamics**, Copernicus Publications Göttingen, Germany, v. 5, n. 4, p. 821–839, 2017.

SHANG, W. *et al.* Understanding and improving convolutional neural networks via concatenated rectified linear units. *In*: PMLR. **international conference on machine learning**. [*S.l.: s.n.*], 2016. p. 2217–2225.

SHEELA, K. G.; DEEPA, S. N. Review on methods to fix number of hidden neurons in neural networks. **Mathematical Problems in Engineering**, v. 2013, 2013. ISSN 1024-123X.

SHEN, M. *et al.* Estimating uncertainty and its temporal variation related to global climate models in quantifying climate change impacts on hydrology. **Journal of Hydrology**, v. 556, p. 10–24, 2018. ISSN 0022-1694.

SHI, Z. *et al.* Development of integrated flooding early warning and rainfall runoff management platform for downtown area of shanghai. **Sustainability**, v. 13, n. 20, p. 11250, 2021.

SHIN, H.-C. *et al.* Deep convolutional neural networks for computer-aided detection: Cnn architectures, dataset characteristics and transfer learning. **IEEE transactions on medical imaging**, IEEE, v. 35, n. 5, p. 1285–1298, 2016.

SHRESTHA, R. R.; THEOBALD, S.; NESTMANN, F. Simulation of flood flow in a river system using artificial neural networks. **Hydrology and earth system sciences**, Copernicus GmbH, v. 9, n. 4, p. 313–321, 2005.

SHRESTHA, S.; LOHPAISANKRIT, W. Flood hazard assessment under climate change scenarios in the yang river basin, thailand. **International Journal of Sustainable Built Environment**, v. 6, n. 2, p. 285–298, 2017. ISSN 2212-6090. Disponível em: http://www.sciencedirect.com/science/article/pii/S221260901530025X.

SILLMANN, J. *et al.* Climate extremes indices in the cmip5 multimodel ensemble: Part 2. future climate projections. **Journal of Geophysical Research: Atmospheres**, v. 118, n. 6, p. 2473–2493, 2013. ISSN 2169-897X.

SIM, I. *et al.* Analysis of effect of temporal resolution in projected future rainfall data on estimating future rainfall intensity-duration-frequency curves. *In*: **EGU General Assembly Conference Abstracts**. [*S.l.: s.n.*], 2018. p. 2139.

SIT, M. *et al.* A comprehensive review of deep learning applications in hydrology and water resources. **Water Science and Technology**, IWA Publishing, v. 82, n. 12, p. 2635–2670, 2020.

SONG, T. *et al.* Flash flood forecasting based on long short-term memory networks. **Water**, Multidisciplinary Digital Publishing Institute, v. 12, n. 1, p. 109, 2020.

SZEWRAŃSKI, S. *et al.* Pluvial flood risk assessment tool (pfra) for rainwater management and adaptation to climate change in newly urbanised areas. **Water**, MDPI, v. 10, n. 4, p. 386, 2018.

TANG, J. *et al.* Statistical downscaling and dynamical downscaling of regional climate in china: Present climate evaluations and future climate projections. **Journal of Geophysical Research: Atmospheres**, Wiley Online Library, v. 121, n. 5, p. 2110–2129, 2016.

TAYLOR, L.; NITSCHKE, G. Improving deep learning with generic data augmentation. *In*: IEEE. **2018 IEEE Symposium Series on Computational Intelligence (SSCI)**. [*S.l.: s.n.*], 2018. p. 1542–1547.

TENG, J. *et al.* Flood inundation modelling: A review of methods, recent advances and uncertainty analysis. **Environmental Modelling Software**, v. 90, p. 201–216, 2017. ISSN 1364-8152.

THIEKEN, A. H. *et al.* Flood damage and influencing factors: New insights from the august 2002 flood in germany. **Water resources research**, v. 41, n. 12, 2005. ISSN 0043-1397.

USACE. **The Hydrologic Modeling System HEC-HMS Users Manual**. 3rd. ed. [*S.l.*], 2010.

USACE, U. A. C. of E. **1D vs 2D Hydraulic Modeling**. 2023. Accessed: 2023-07-20. Disponível em: https://www.hec.usace.army.mil/confluence/rasdocs/r2dum/latest/ steady-vs-unsteady-flow-and-1d-vs-2d-modeling/1d-vs-2d-hydraulic-modeling.

VELDHUIS, J. T. How the choice of flood damage metrics influences urban flood risk assessment. **Journal of Flood Risk Management**, v. 4, n. 4, p. 281–287, 2011. ISSN 1753-318X.

VERDIN, J. *et al.* **A software tool for rapid flood inundation mapping**. [*S.l.*], 2016.

WANG, K. *et al.* Generative adversarial networks: introduction and outlook. **IEEE/CAA Journal of Automatica Sinica**, IEEE, v. 4, n. 4, p. 588–598, 2017.

WANG, Q. *et al.* Individual and combined impacts of future land-use and climate conditions on extreme hydrological events in a representative basin of the yangtze river delta, china. **Atmospheric Research**, Elsevier, v. 236, p. 104805, 2020.

WANG, Z. *et al.* Climate change enhances the severity and variability of drought in the pearl river basin in south china in the 21st century. **Agricultural and Forest Meteorology**, Elsevier, v. 249, p. 149–162, 2018.

WANNOUS, C.; VELASQUEZ, G. United nations office for disaster risk reduction (unisdr)—unisdr's contribution to science and technology for disaster risk reduction and the role of the international consortium on landslides (icl). *In*: SPRINGER. **Workshop on World Landslide Forum**. [*S.l.: s.n.*], 2017. p. 109–115.

WASKO, C.; SHARMA, A. Continuous rainfall generation for a warmer climate using observed temperature sensitivities. **Journal of Hydrology**, Elsevier, v. 544, p. 575–590, 2017.

WBM, B. **Tuflow user manual-gis based 2d/1d hydrodynamic modelling**. [*S.l.*], 2008.

WIJERATHNE, K.; SENEVIRATHNA, E. Identify the risk for leptospirosis disease during flooding periods (special reference to medirigiriya divisional secretariat division in polonnaruwa district). **Procedia engineering**, v. 212, p. 101–108, 2018. ISSN 1877-7058.

WINSEMIUS, H. C. *et al.* Global drivers of future river flood risk. **Nature Climate Change**, v. 6, n. 4, p. 381–385, 2016. ISSN 1758-6798. Disponível em: https://doi.org/10.1038/nclimate2893.

WOLFRAM, S. Cellular automata as models of complexity. **Nature**, v. 311, n. 5985, p. 419–424, 1984. ISSN 1476-4687.

WOZNICKI, S. A. *et al.* Development of a spatially complete floodplain map of the conterminous united states using random forest. **Science of the total environment**, Elsevier, v. 647, p. 942–953, 2019.

WU, W. *et al.* A benchmarking approach for comparing data splitting methods for modeling water resources parameters using artificial neural networks. **Water Resources Research**, Wiley Online Library, v. 49, n. 11, p. 7598–7614, 2013.

XU, S.; CHEN, L. A novel approach for determining the optimal number of hidden layer neurons for fnn's and its application in data mining. *In*: **5th International Conference on Information Technology and Applications (ICITA 2008)**. [*S.l.: s.n.*], 2008. p. 683–686. ISBN 978-0-9803267-2-7.

YIN, J. *et al.* A copula-based analysis of projected climate changes to bivariate flood quantiles. **Journal of hydrology**, v. 566, p. 23–42, 2018. ISSN 0022-1694.

YIN, J. *et al.* Evaluating the impact and risk of pluvial flash flood on intra-urban road network: A case study in the city center of shanghai, china. **Journal of hydrology**, v. 537, p. 138–145, 2016. ISSN 0022-1694.

ZHANG, C. *et al.* Understanding deep learning (still) requires rethinking generalization. **Communications of the ACM**, ACM New York, NY, USA, v. 64, n. 3, p. 107–115, 2021.

ZHANG, S.; PAN, B. An urban storm-inundation simulation method based on gis. **Journal of Hydrology**, Elsevier, v. 517, p. 260–268, 2014.

ZHAO, G. *et al.* Urban flood susceptibility assessment based on convolutional neural networks. **Journal of Hydrology**, Elsevier, v. 590, p. 125235, 2020.

APPENDIX

APPENDIX A – COUPLING HEC-RAS WITH CGAN-FLOOD

The overall steps for predicting high-resolution flood maps with a coarse HEC-RAS model (mesh-based) are highlighted in Figure 1a. Breaklines are integrated to capture the specific stormwater channels and transportation infrastructure features. The incorporation of breaklines for the channels serves a dual purpose. Firstly, they reduce the cell size and align cell faces along the channel more accurately, thereby improving the representation of the channel's characteristics and flow dynamics. Breaklines for transportation infrastructure are inserted to depict the elevation of streets along the cell faces, generally indicating high landforms and water dividers. However, it's important to note that the coarse resolution of the cells can often lead to inaccurate representation of these elevated areas. Consequently, the model may not properly recognize these as barriers to water flow, leading to water being erroneously modeled as "leaking" through these cells. This misrepresentation reduces the flow path incorrectly, impacting the flow dynamics representation. Furthermore, it inaccurately decreases the total volume to be distributed (v_t), which may lead to underestimation of flood extents and depths. Although enforcing breaklines reduces the average cell size of the mesh and increases computational time, our previous investigations showed that they were essential for estimating v_t.
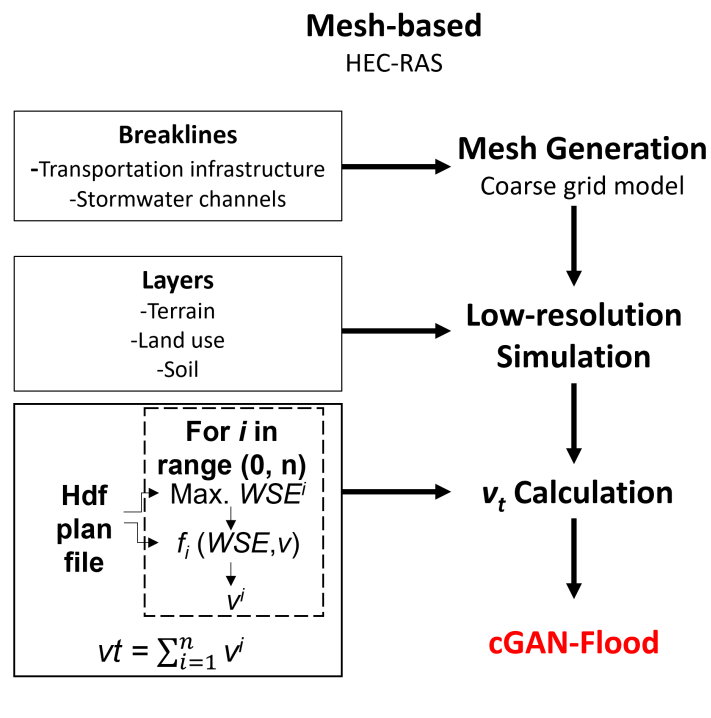

Figure 28 – Flowchart depicting how HEC-RAS model is set up and coupled with cGAN-Flood

Terrain, land use, and infiltration layers were also used in our HEC-RAS simulations.

The terrain layer is essential for computing elevation versus volume for each cell and generating hydraulic properties tables for their faces (BRUNNER, 2016). These hydraulic properties tie in the elevation of every cell face with corresponding variables such as area, wetted perimeter, and roughness. The land-use layer furnishes the model with critical information, including roughness values and the proportion of impervious area. This data is essential for accurately estimating the frictional resistance to flow and understanding the percentage of the area where water infiltration into the ground is minimal or non-existent. Conversely, the soil or infiltration layer imparts parameters related to the rate and extent of water infiltration into the ground. It is a critical element in modeling the portion of the rainfall that will contribute to the runoff and the portion that will infiltrate into the soil, significantly influencing the simulated flood's volume and timing.

cGAN-Flood is a tool capable of enhancing the resolution of coarse flood maps by redistributing a predetermined flood volume. This volume for being redistributed is calculated after the hydraulic simulation is concluded. However, deriving these flood volumes directly from the output depth maps of HEC-RAS presents a challenge. The HEC-RAS model operates on a mesh-based system with cells that vary in shape and size, with each cell potentially containing multiple raster pixels. The model calculates depths by interpolating each cell face's computed water surface elevation and subtracting it from the terrain elevation. While HEC-RAS does not include a feature for generating volume outputs for individual cells, a workaround is available through the plan HDF file, allowing maximum volumes to be computed. The model calculates and stores each cell's Water Surface Elevation (WSE) during each simulated timestep. This data, accessible via the plan HDF file, also includes an elevation-volume curve for each cell. Consequently, each cell's volume (v) can be approximated from the elevation-volume curve given a specific WSE. The sum of the maximum volume in each of the n cells of a given domain is the v_t to be redistributed with cGAN-Flood.

APPENDIX B − COUPLING HYDROPOL2D WITH CGAN-FLOOD

Unlikely mesh-based model, which computes flow dynamics across cells according to the hydraulic properties calculated with terrain, land use, and soil layers, raster-based models compute water balance and calculate mass exchange in each pixel of the input rasters. This study used Hydropol2D (JR *et al.*, 2023) as a raster-based model for calculating v_t.
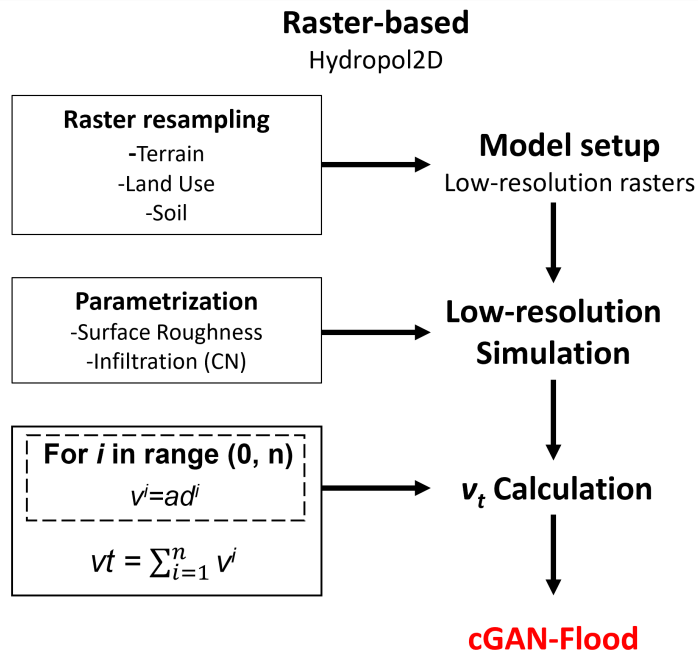
Raster-based
Hydropol2D

Raster resampling
-Terrain
-Land Use
-Soil

→ **Model setup**
Low-resolution rasters

Parametrization
-Surface Roughness
-Infiltration (CN)

→ **Low-resolution Simulation**

For *i* in range (0, n)
$v^i = ad^i$

$vt = \sum_{i=1}^{n} v^i$

→ **v_t Calculation**

cGAN-Flood

Figure 29 – Flowchart describing how Hydropol2D was used to compute v_t and coupled with cGAN-Flood

The input data for the Hydropol2D simulations comprise terrain, land use, and soil raster datasets. The parameters within Hydropol2D are configured independently to link surface roughness and infiltration properties with pixel values corresponding to various land uses and soil types. All input rasters must maintain the same cell size and identical quantities of rows and columns. These rasters were downsampled for the low-resolution simulations conducted with Hydropol2D, effectively reducing the number of cells and the number of computational calculus. This downsampling process has the additional benefit of decreasing the Courant number, thereby allowing for larger time steps and expedited simulations. However, the terrain's hydraulic properties, especially the channels, can be lost after reducing the terrain resolution. As such, the terrain was treated with smoothening (SCHWANGHART; SCHERLER, 2017) and burning (PAIVA *et al.*, 2013).

As raster-based models compute water balance between pixels directly, the volume in each cell can be calculated directly from the output depth map. The volume in each cell (v) is calculated by multiplying the water depth in that particular cell (d) by its area (pixel resolution squared). Therefore, the v_t to be redistributed with cGAN-Flood is the sum of the flood volume of all n cells within the area of interest.
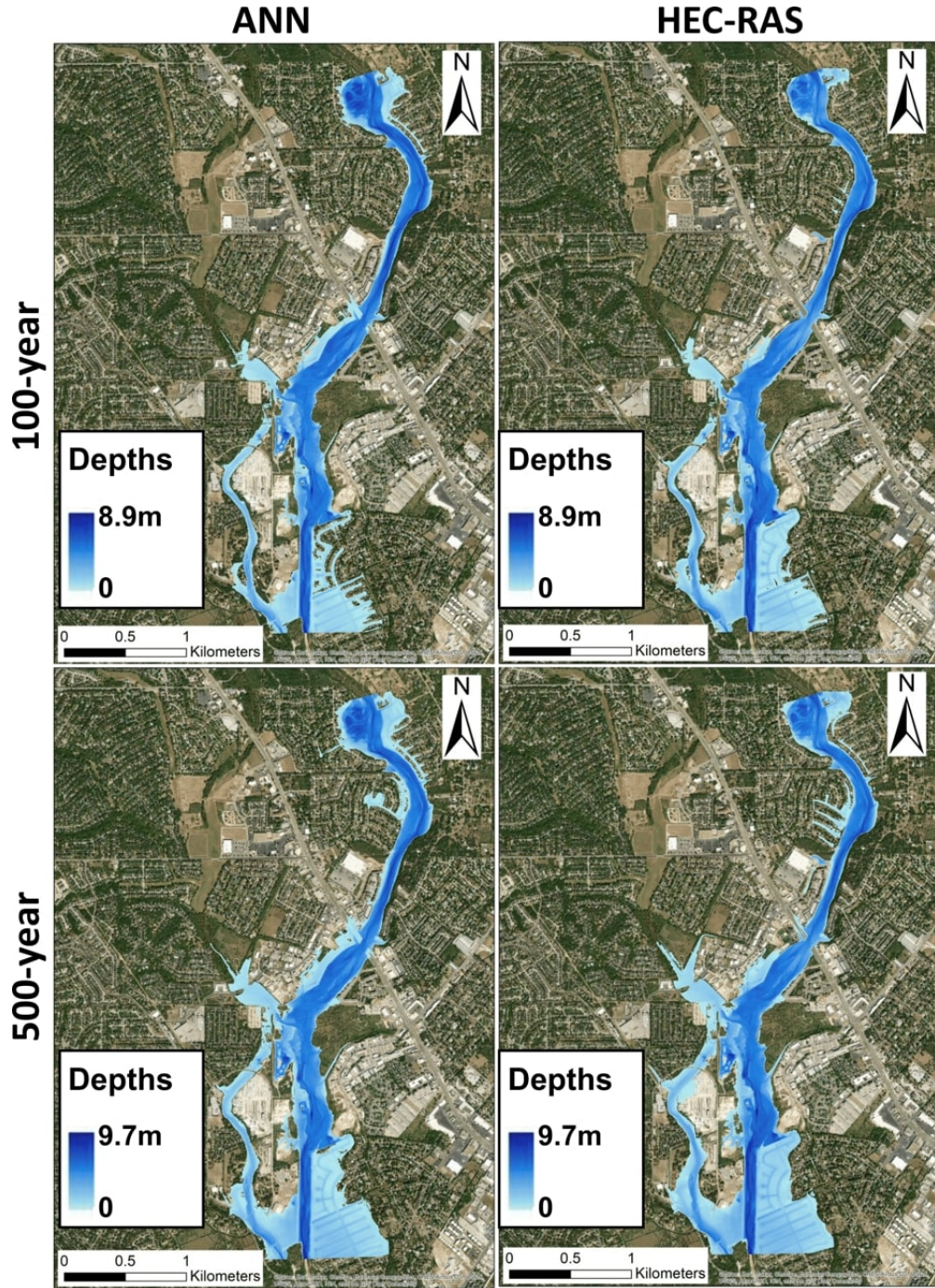
APPENDIX C – FLUVIAL FLOOD PREDICTIONS

Figure 30 – Performance of ANN model in predicting fluvial flood for area TE1
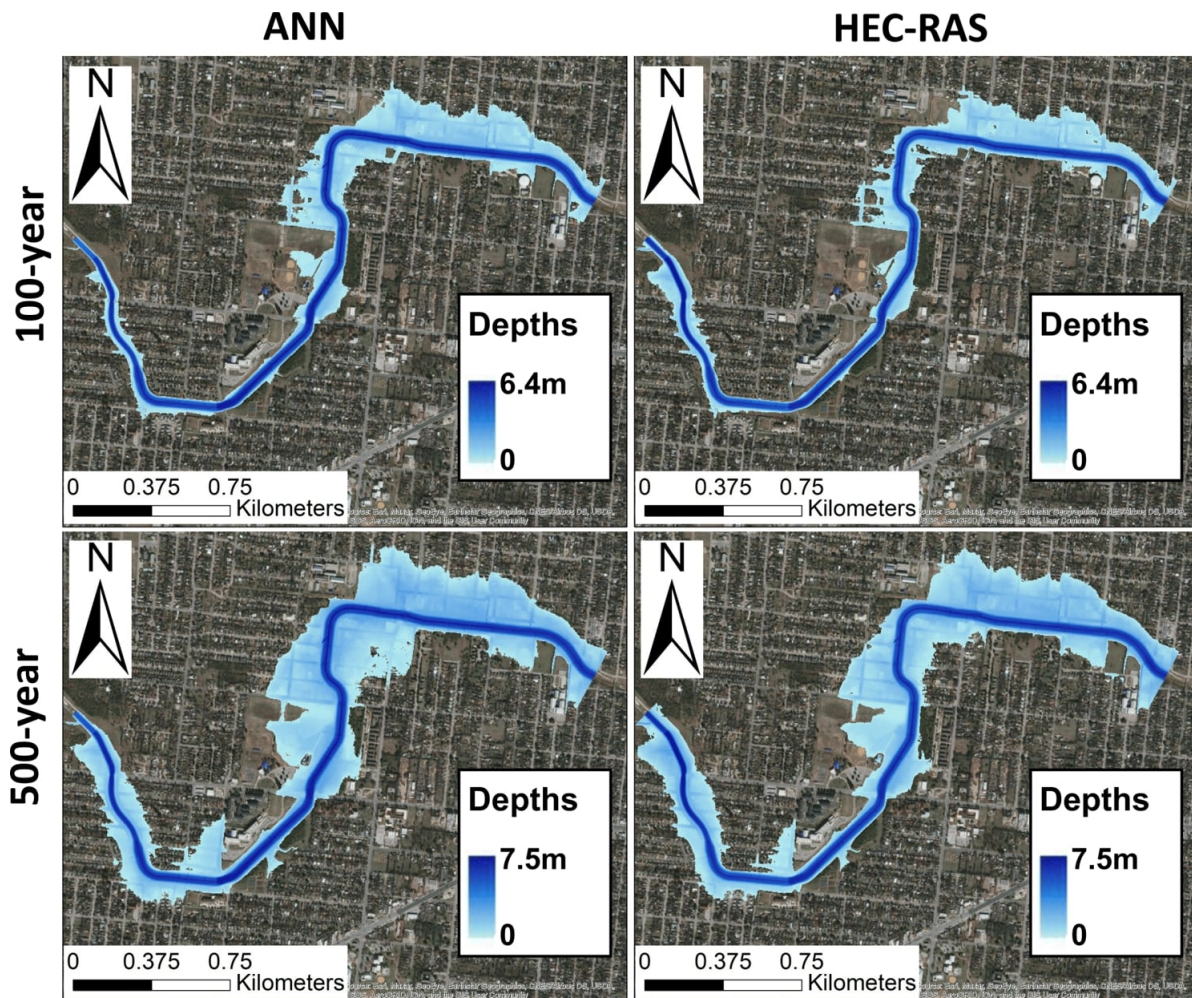
Figure 31 – Performance of ANN model in predicting fluvial flood for area TE2
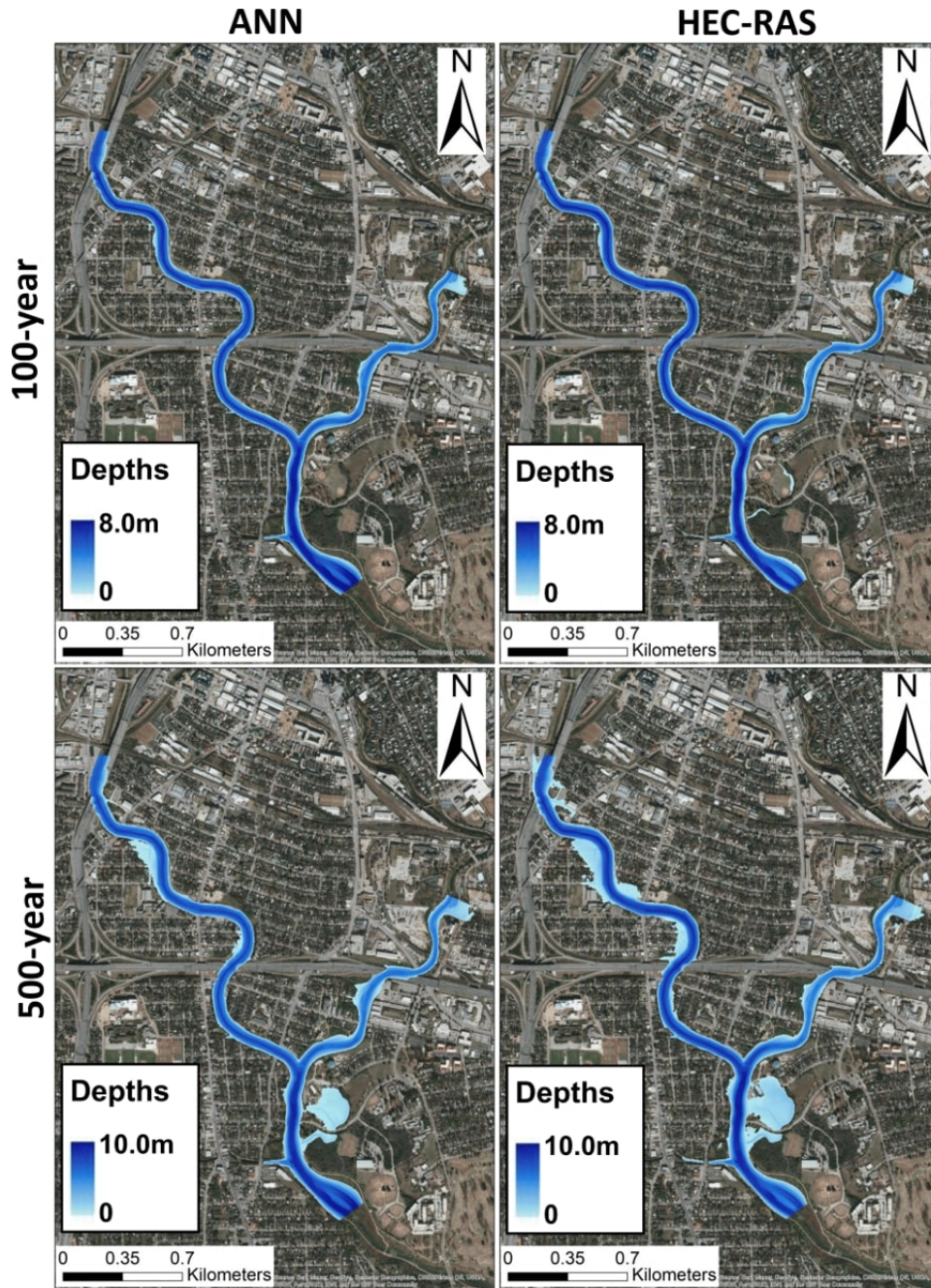
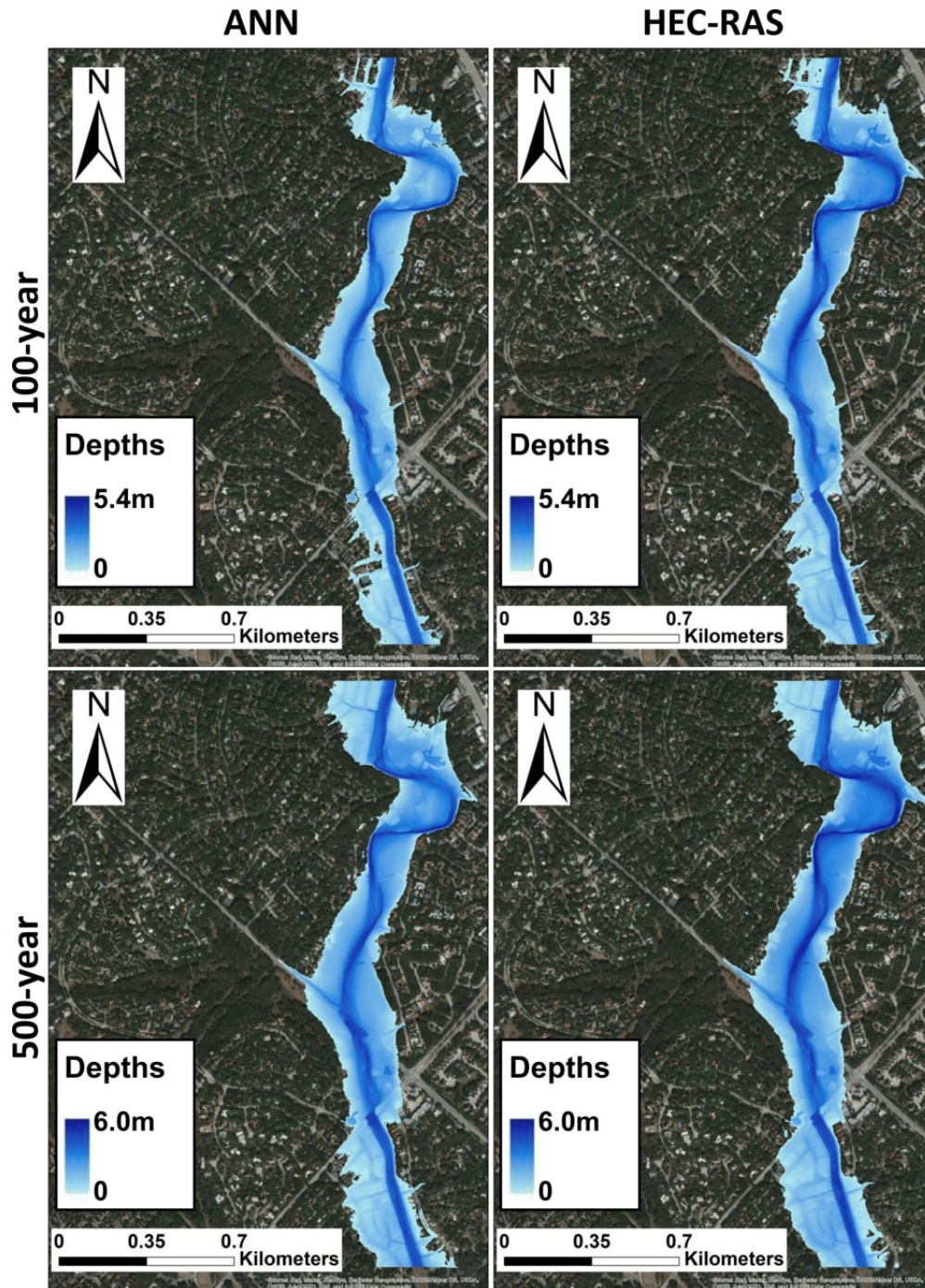Figure 32 – Performance of ANN model in predicting fluvial flood for area TE3

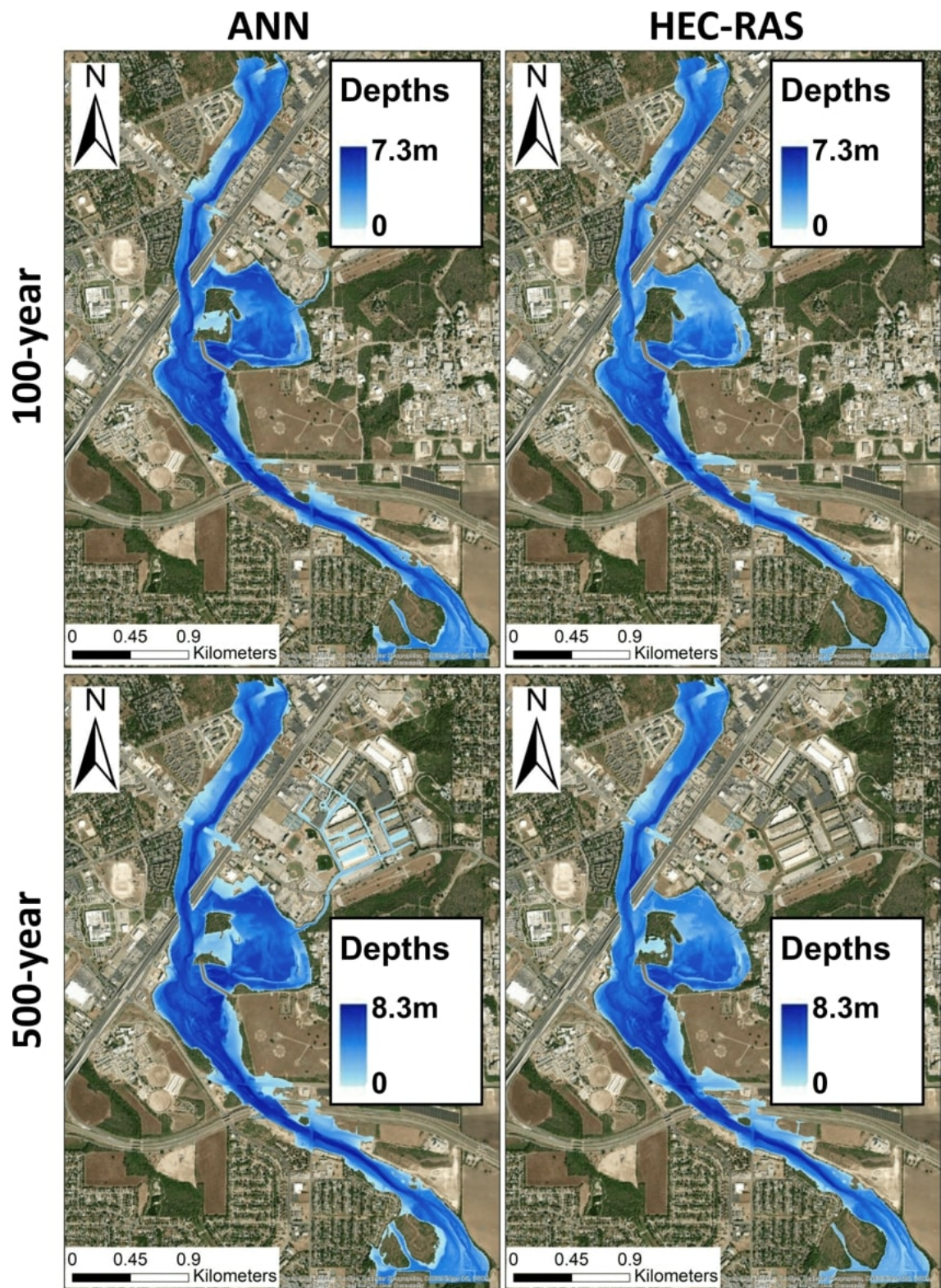Figure 33 – Performance of ANN model in predicting fluvial flood for area VA1

Figure 34 – Performance of ANN model in predicting fluvial flood for area VA2
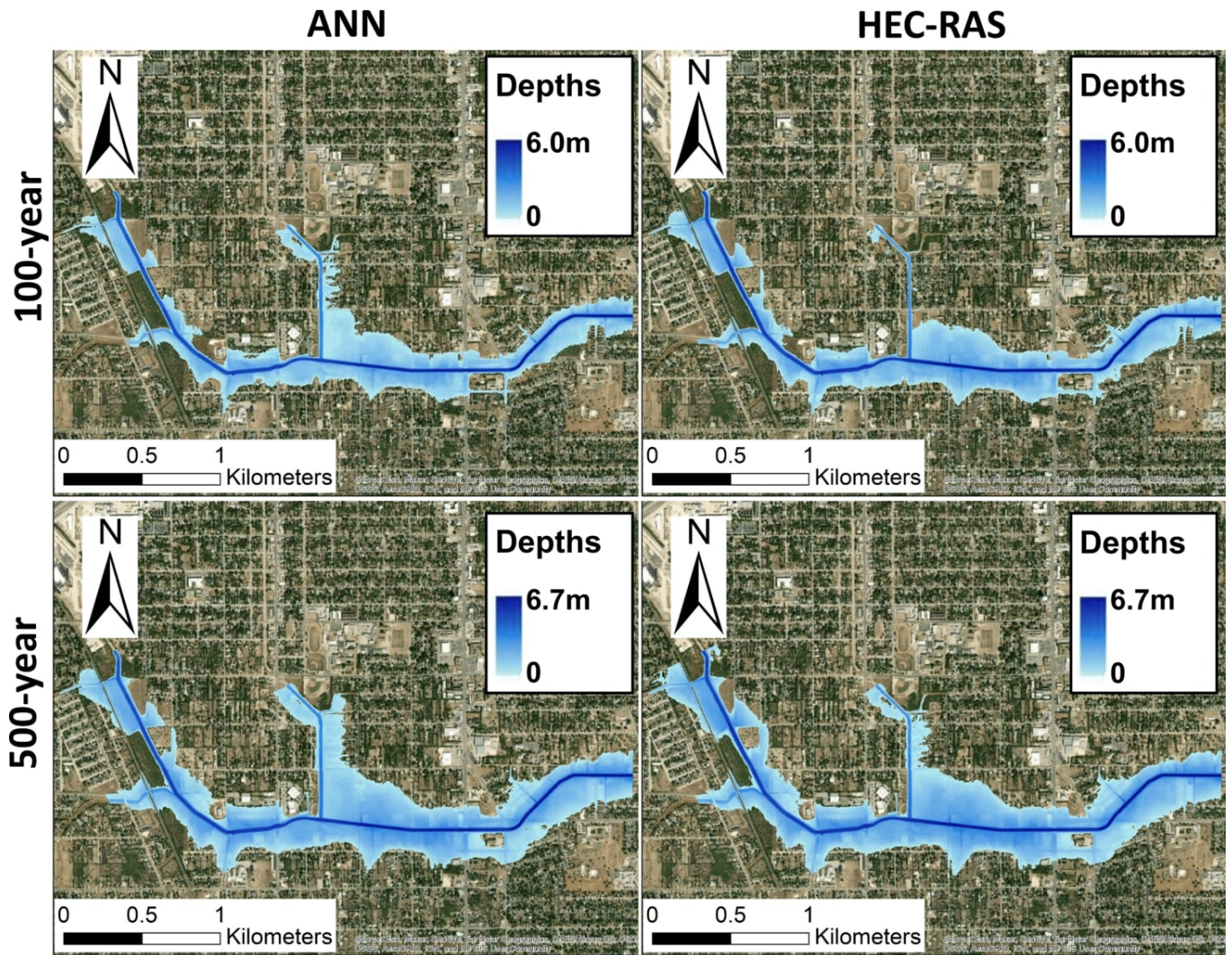
Figure 35 – Performance of ANN model in predicting fluvial flood for area VA3